Strojniški vestnik

Journal of Mechanical Engineering

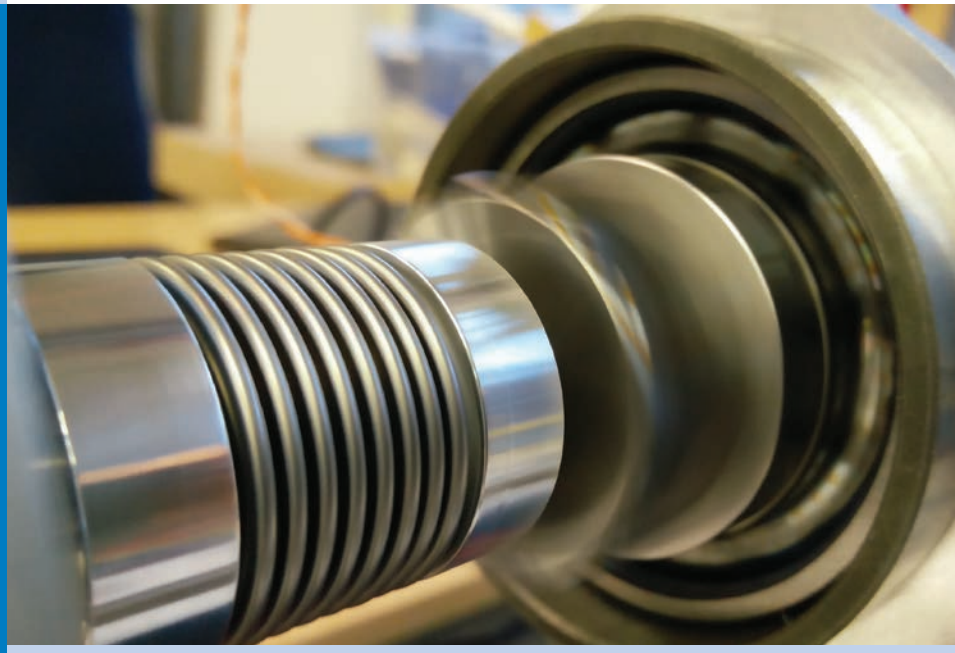

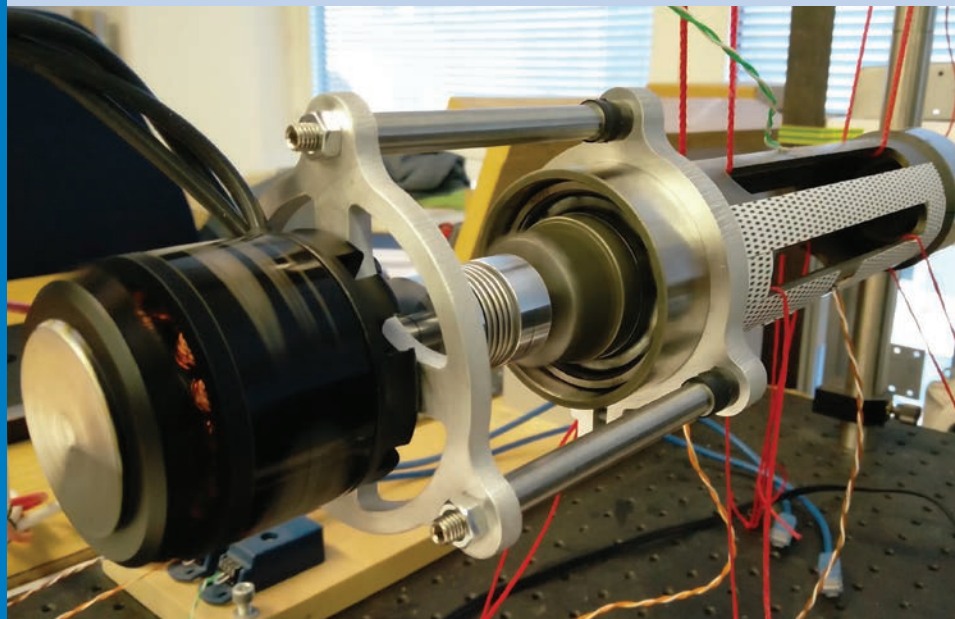

no. 7-8
year 2023
volume 69

Strojniški vestnik – Journal of Mechanical Engineering (SV-JME)

Aim and Scope
The international journal publishes selected original high quality articles in the areas of materials science, mechanics, thermodynamics, energy and environment, mechatronics and robotics, fluid mechanics, tribology, cybernetics, industrial engineering and structural analysis.
The journal follows selected areas in mechanical engineering and related sciences including electrical engineering, civil engineering and computer science, medicine and biology, agriculture, transportation systems, environmental technology and naval architecture.
The international advisory board helps with the selection of topics for special issues and with the choice of articles for publication.

Print: Demat d.o.o., printed in 240 copies

Founders and Publishers
University of Ljubljana, Faculty of Mechanical Engineering, Slovenia
University of Maribor, Faculty of Mechanical Engineering, Slovenia
Association of Mechanical Engineers and Technicians of Slovenia
Chamber of Commerce and Industry of Slovenia, Metal Processing Industry Association

Cover:
An experimental setup for testing the dynamics of rolling-element bearings is presented. The top image shows a close-up view of the system with a rotating shaft, while the bottom image shows the complete setup at free-free boundary conditions required to provide the bottom-up validation study.

Image Courtesy:
Matej Razpotnik, Slovenia

ISSN 0039-2480, ISSN 2536-2948 (online)

General information
Strojniški vestnik – Journal of Mechanical Engineering is published in 6 double issues per year.

Institutional prices include print & online access: institutional subscription price and foreign subscription €100,00 (the price of a single issue is €10,00); general public subscription and student subscription €50,00 (the price of a single issue is €5,00). Prices are exclusive of tax. Delivery is included in the price. The recipient is responsible for paying any import duties or taxes. Legal title passes to the customer on dispatch by our distributor. Single issues from current and recent volumes are available at the current single issue price. To order journals please contact the following website. Sample issues, subscription information and online publication are available at: *http://www.sv-jme.eu*.

You can advertise in the journal. The authors of the published papers are invited to submit additional information for publication of the commercial advertisements in the journal. Send your inquiries to: *info@sv-jme.eu*.

We would like to thank the reviewers who took part in the peer-review process.

SV-JME is indexed / abstracted in SCI-Expanded, Compendex, Inspec, ProQuest-CSA, SCOPUS, TEMA. The list of the remaining bases, in which V-JME is indexed, is available on the website.

The journal is financially supported by Slovenian Research and Innovation Agency.

Strojniški vestnik Journal of Mechanical Engineering is available on *https://www.sv-jme.eu*.

Contents

Strojniški vestnik - Journal of Mechanical Engineering
volume 69, (2023), number 7 8
Ljubljana, July August 2023
ISSN 0039-2480

Published everyt wo months

Papers

Strojniški vestnik - Journal of Mechanical Engineering 69(2023)7-8, 289-298
DOI:10.5545/sv-jme.2023.592
Original Scientific Paper
Received for review: 2023-03-30
Received revised form: 2023-05-03
Accepted for publication: 2023-05-31

The Dynamics of Tapered-roller Bearings – A Bottom-up Validation Study

Matej Razpotnik[1] - Thomas Bischof[2] - Miha Boltežar[1,*]
[1]University of Ljubljana, Faculty of Mechanical Engineering, Slovenia
[2]ZF Friedrichshafen AG, Germany

Rolling-element bearings are one of the most important elements when predicting the noise of rotating machinery. As a major connecting point between the rotating and non-rotating parts, their dynamic properties have to be accurately known. In this investigation we present a bottom-up approach to characterising the dynamics of the rolling-element bearing. A special test device was designed and built to assess the quality of the well-established analytical modelling approach of Lim and Singh. Two types of bearings were tested, i.e., the ball and tapered-roller types. The dynamic properties were observed by investigating the frequency-response functions. In addition, non-rotating as well as rotating test scenarios were checked. It was shown that the ball bearing model adequately predicts the system's response, whereas the tapered-roller bearing model requires modifications. These results were further confirmed with a quasi-static load-displacement numerical evaluation, where a full finite-element model serves as the reference.

Keywords: dynamic bearing model, tapered-roller bearing, bearing stiffness matrix, vibration transmission

Highlights

- *Test device for bottom-up investigation of bearing's dynamics is built.*
- *Ball and tapered-roller bearings are tested at different speeds and axial preloads.*
- *The system is evaluated numerically and experimentally.*
- *Ball bearing model is validated whereas tapered-roller one needs improvements.*

0 INTRODUCTION

Every rotating machinery contains bearings. They represent the connecting points between the rotating and non-rotating parts and so are very important elements in the chain of vibration transmission. The dynamic properties of rolling-element bearings have been studied for many decades; however, due to their complex contact-related phenomena the topic remains important in ongoing research.

A first general theory for elastically constrained ball and roller bearings was developed by Jones [**1**]. Later this theory was further extended by Harris [**2**]. The theory was very general and focused more on static and fatigue-life calculations than on the vibration transmission through the bearings. Simplified bearing models were introduced by other researchers, with the bearings being modelled as an ideal boundary condition for the shaft, as presented by Rao [**3**]. Meanwhile, the idea of interpreting the bearings with a simple one- or two-degrees-of-freedom (DOFs) model with linear springs was introduced by While [**4**] and Garigiulo [**5**]. Later, more accurate dynamic bearing models were derived. A major improvement in predicting the vibration transmission through rolling-element bearings was made by Lim and Singh [**6**] and [**7**] and in parallel by de Mul [**8**]. They derived a model that provides a comprehensive bearing-stiffness matrix. The model is capable of describing the nonlinear relation between the load and the deflection, taking into account all six DOFs and their interplay. These authors also presented system studies [**9**] and [**10**] for model-validation purposes. A good agreement between the measurements and the analytical model was shown for the ball and the cylindrical roller bearings as the two most distinct examples of different contact types. The six-DOFs model is the basis for the widely used industrial standard ISO/TS 16281 [**11**] as well as for many subsequent studies. Recently, a thorough review of mechanical model development of rolling-element bearing was presented by Cao et al. [**12**]. The authors classify modelling approaches into five different techniques and comprehensively discuss the current progress of development as well as identify future trends for research. Despite great computational power available these days, modelling of the bearings primary remains on the analytical level. Contact related phenomena and non-linearities lead to huge and often unstable finite-element method (FEM) models. However, connecting analytical models with numerical ones is crucial in predicting the proper behaviour of a modern system. Guo and Parker [**13**] presented a stiffness-matrix calculation

*Corr. Author's Address: University of Ljubljana, Faculty of Mechanical Engineering, Aškerčeva 6, 1000 Ljubljana, Slovenia, miha.boltezar@fs.uni-lj.si

using a finite-element/contact-mechanics model. On the other hand analytical approaches demand advanced methods to solve the system of nonlinear equations. Fang et al. [14] recently presented a comprehensive study of the speed-varying stiffness of ball bearings under different load conditions. They proposed a novel mathematical method for solving an implicit set of nonlinear equations based on a new assumption of the initial conditions. To mitigate the numerical difficulties of time integration procedure, induced by rolling-elements coming and leaving the contact, Razpotnik et al. [15] extended the model from Lim and Singh [6]. They implemented modular smoothing of the load-displacement characteristics in the region of contact-state transition. To improve the calculation accuracy of non-hertzian contact pressure the high-precision half space theory was adopted by Kabus et al. [16] and [17].

Tapered-roller bearings (TRBs) are widely used in rotor dynamics. They are usually treated as a special case of a cylindrical roller bearing with a non-zero contact angle. The difference, in fact, is much more significant because TRBs have two different contact angles (the inner ring-roller and outer ring-roller contacts) and also because of their additional roller-flange contact. Cretu et al. [18] and [19] analysed the dynamics of TRBs under fully flooded conditions. The assumption of an elastohdydrodynamic (EHD) lubrication regime is common to the majority of TRB studies. In this way the friction forces can be either calculated or, even more commonly, neglected. Tong and Hong [20] analytically studied the characteristics of TRBs subjected to combined radial and moment loads. The same authors [21] investigated the influence of the roller profile and the speed on the stiffness of a TRB. Zhao et al. [22] studied the effect of gyroscopic moment on the damage of a tapered-roller bearing, which are found to occur under high-speed and high-load conditions, such as high-speed trains. Roda-Casanova and Sanchez-Marin [23] presented an illustrative study of the contribution of the deflection of the TRB to the misalignment of the pinion in a pinion-rack transmission. They stressed the importance of having accurate knowledge of the elasticity of the bearings. Houpert [24] studied the torque generated by the friction forces in a TRB, where he emphasised an important fact, i.e., TRBs are subjected to a high roller-flange torque. The roller-flange contact, which largely affects the power loss, was investigated also by Ai et al. [25]. In addition, Tong et al. [26] made numerical evaluation of the effect of misalignment on the generated friction forces and consequently evaluated the power loss of a TRB. It was shown that already a small misalignment can have a significant influence on the generated torque.

Experimental investigations of a TRB's dynamics are rare in the literature. Zhou and Hoeprich [27] measured the torque generated at different contacts in a TRB; however, they focused on the losses and not on the dynamics. Gradu [28] also analysed the TRB losses and compared them with equivalent ball bearing. Wrzochal et al. [29] presented a new device for measuring the friction torque in rolling-element bearings of different types, where the main goal was to establish a reliable device for quality control measurement. Discrepancy between theoretical and measured friction torque was presented and discussed. A comparative study, as presented by Zhang et al. [30] for angular-contact ball bearings, would also be beneficial for TRBs. Further, since TRBs are often used in applications that do not require high speed, the influence of friction on the dynamic properties would be generally welcomed.

In this paper a numerical and experimental characterisation of a TRB's dynamics is presented. First, a general bearing modelling technique is introduced, where the analytical model of Lim and Singh [6, 7] is embedded into a FEM model. Afterwards, a special test device is presented. There follows a description of a workflow for a bottom-up validation study. A TRB is mainly investigated, whereas ball bearing is also tested. The results in the form of frequency-response functions (FRFs) are compared for the measurements and the simulations. The non-rotating as well as low-speed-rotating scenarios are presented. Finally, a quasi-static load-displacement numerical analysis was performed to additionally verify the results.

1 BEARING MODELLING TECHNIQUE

Rolling-element bearings can be modelled as a part of a wider system in several different ways. Most often the system is studied by utilising a FEM model. The bearings are, due to their complex contact-related phenomena, represented by a special element that embeds the analytically calculated bearing-stiffness matrix $\mathbf{K}_b$. This technique introduces the so-called spider elements (commercially known as RBE3 element), as shown in Fig. 1. A spider element connects a raceway of a ring to one, central node. The motion of that central node depends on the weighted average of the motions at a set of connected grid points [31]. Two spider elements are needed,

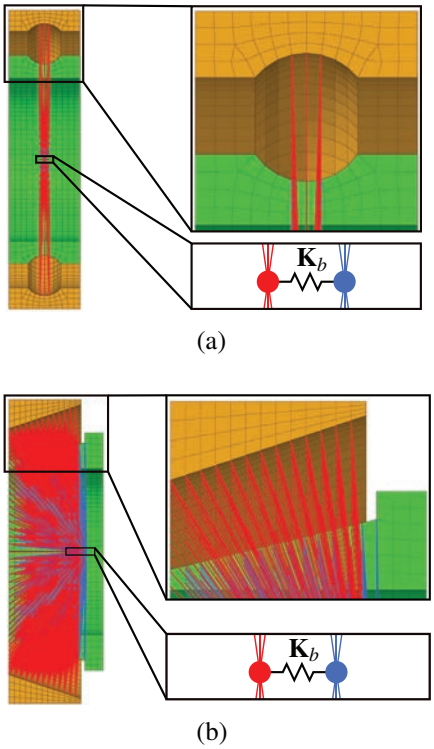

Fig. 1. *A cross-section view of a bearing in a FEM model with zoomed-in areas; a) ball bearing, and b) TRB*

each for one bearing ring. Central nodes, connected by $\mathbf{K}_b$, are located at exactly the same position. Fig. 1 separates them just for illustrative purposes. Bearing rings can be coarsely meshed since the mesh is only used to represent the shape of the ring and to serve as a connecting body for the spider element. Rolling elements are not modelled, since all contact-related phenomena are covered by the stiffness matrix. The source of the accuracy of the presented technique is not in the spider element itself, but in the bearing-stiffness matrix. In this study we implement the bearing-stiffness matrix from Lim and Singh [**6**] and [**7**]; however, any relevant bearing theory yielding the stiffness matrix can be implemented.

There are two types of FEM analyses used in the presented study, i.e., frequency-response modal analysis and quasi-static load-displacement analysis. Both assume that rolling elements are not rotating. However, the former is used to obtain dynamic response of the system when excited and subjected under different axial loads, and the latter is used to obtain load-displacement characteristics of a bearing.

2 TEST DEVICE

A simple test device was designed and built for validation purposes. It consists of the housing, a long shaft and a special nut, as shown in Fig. 2. It is important to note the shape of the nut, which is only in contact at both ends. This design ensures that the load dependency of the thread contact is negligible. A bottom-up validation approach was

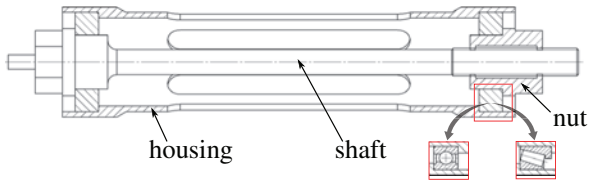

Fig. 2. *A simplified technical drawing of the test device, where all three possible configurations are shown*

utilised. Therefore, solid rings are inserted at first in order to prove the linearity of the system. Afterwards, two types of rolling-element bearings were tested, i.e., ball bearing and TRB, with the properties given in Table 1. In order to eliminate the influence of the surroundings, the device was tested with free-free boundary conditions (BCs). These conditions were achieved by hanging the test device via housing by thin ropes. The FRFs were measured between different

Table 1. *Bearings used in the test device.*

type	designation	d [mm]	D [mm]	B [mm]
ball	6006	30	55	13
tapered-roller	32006-X	30	55	17

parts of the system. An excitation was applied with a modal hammer, whereas the acceleration was measured by the accelerometer. The transfer path from the shaft to the housing is of special interest, since the bearing's dynamics are the most clearly seen there. The test device makes it possible to apply different axial preloads to the bearings and consequently to the entire system by turning the nut with respect to the shaft. The applied axial force is measured with the strain gauges located at the housing ribs. Additionally, the system can be investigated while the shaft is either stationary or rotating (up to 6000 rpm). For this purpose a special motor can be mounted to the system. In doing so, the free-free BCs are maintained, as shown in Fig. 3.

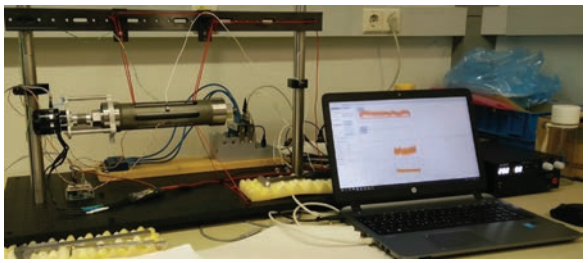

Fig. 3. *Experimental setup with attached motor*

3 WORKFLOW

The main goal was to evaluate the quality of the analytically calculated dynamic bearing model. The assessment was made for a non-rotating scenario by comparing the dynamic properties of the system in the form of FRFs. We focused on a representative FRF, namely Accelerance, where the excitation was performed on the shaft and acceleration was obtained at the housing, as shown in Fig. 4. All of the possible setups (solid rings, ball bearings, TRBs) undergo the same testing procedure. Four different axial preloads were inserted into the system. Thus, four different FRFs were obtained. Fig. 5 shows

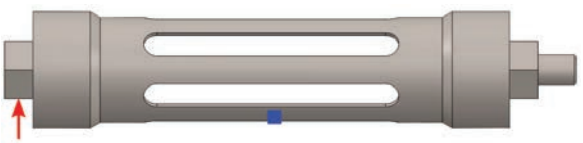

Fig. 4. *Excitation point and accelerometer position*

the corresponding workflow. The same workflow is followed for measurements and simulations. Finally, the FRFs are compared.

The rotating version of the test device was investigated only experimentally. A run-up investigation was utilised. By that we can see the potential change of the system's dynamics due to rotor-dynamic effects appearing in the rolling bearings, e.g., centrifugal forces and gyroscopic effects. Some researchers have pointed out these effects during high-speed applications [**1**], [**14**], [**21**], [**22**], and [**32**], where the effects start to become noticeable in the region between 5000 rpm and 10000 rpm, depending on the bearing type and load case. However, it is important to note that our testing did not exceed 6000 rpm. When the system rotates, there is no additional external excitation. The system is mainly excited by the white noise coming from the bearings. The resulting acceleration is measured and shown in a Campbell diagram.

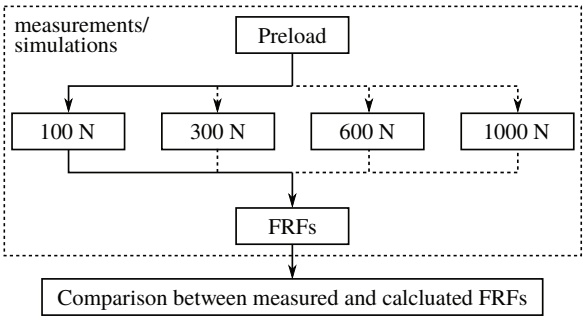

Fig. 5. *Workflow of the validation procedure for the non-rotating test device*

4 RESULTS

4.1 Solid Rings

With solid rings inserted it is possible to verify whether the system without bearings is linear or not. The linearity implies the load-independent dynamic properties of the system. Ideally, the presented system should be load-independent; however, due to contact issues, especially the thread contact, the load independence has to be experimentally proven. Fig. 6 shows the results. The measured FRFs, given in the form of Accelerance (A), are shown with a gray and black colour. The red curve corresponds to simulation. The preload was considered in simulations as well, but its effect is completely unnoticeable, thus only one line sufficiently represents the simulation results. It is clear that all the measured curves correlate well with each other regarding the eigenfrequency position. Damping, however, decreases with an increased preload. Also, the calculated FRF predicts the measured behaviour correctly. However, the peak around 1.45 kHz is more damped in the measured results.

Proving the linearity of the system with solid rings is an important step. All the non-linearities in the succeeding investigations (when real bearings are inserted) can now be associated with the bearing's behaviour.

4.2 Ball Bearings

The ball bearings, as given in Table 1, are inserted into the system. Fig. 7 shows the amplitude comparison between the measured and calculated results. It is clear that some peaks move their position with the increased preload, while the others do not. Those involving the modes of the shaft are affected, while the others are not. Fig. 8 shows the modes of the marked regions from Fig. 7. The stiffness of the bearing plays a crucial role there. All of them are pure modes of the shaft, only the mode at 2490 Hz is a combination

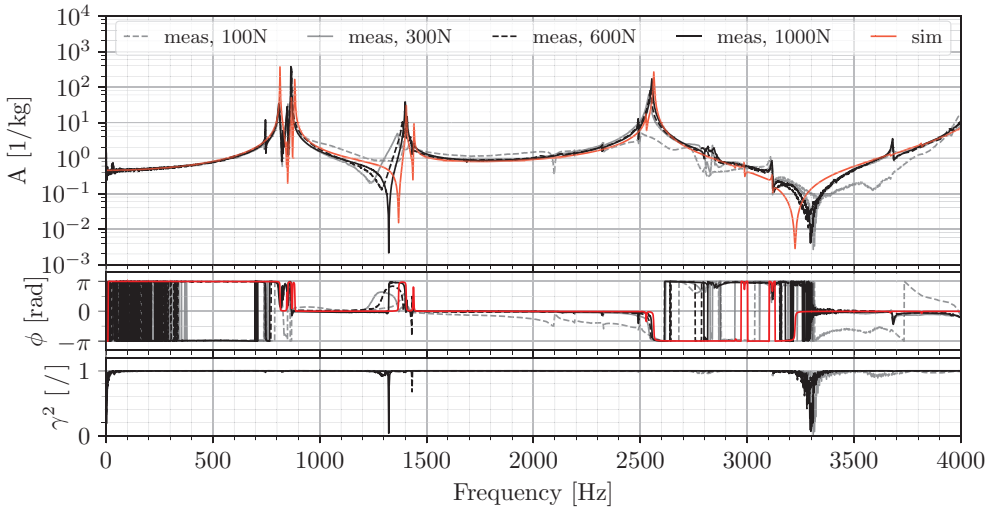

Fig. 6. *Load-dependency of the FRF (from top to bottom: magnitude, phase, coherence) for the test device with the inserted solid rings*

of shaft and the local movement of the housing ribs. Additionally, it is clear that the higher the preload, the higher is the bearing stiffness. This also causes the eigenfrequencies to increase. Comparing the spectra it can be seen that the frequency span of each affected eigenfrequency is around 100 Hz for the measured as well as the calculated FRFs. Some peak positions, however, differ slightly, but the general behaviour is well predicted. It is important to note that no FEM model updating was performed. Doing so would obviously align the calculated results completely with the measured ones.

So far, we have presented the non-rotating version of the test device. Since the bearings are meant to rotate it is crucial to determine whether the analytical bearing-stiffness matrix is an adequate representation of the bearing's dynamics also under operating conditions. A run-up test was performed. An extension to the motor was additionally mounted to the test device while maintaining its free-free BCs (see Fig. 3). The run-up test sequentially increases the motor speed from 500 rpm to 6000 rpm with a step of 100 rpm. At each step the acceleration on the housing (the same position as for the FRF investigation) was measured. The resulting Campbell diagram is shown in Fig. 9 for the preloads of 300 N and 1000 N. The preload of 100 N was found to be too loose for the run-up investigation. Already a slight torque induced by the motor caused a disturbance that changed the axial preload. At 300 N this effect is not noticeable any more. It is clear that the eigenfrequencies governed by the bearing stiffness do change with a higher preload in a similar manner to the non-rotating version. They are marked with red arrows. On the other hand, their position does not change while increasing the RPM in the investigated RPM region. Another important conclusion is that the locations of the eigenfrequencies remain at practically the same positions as in the non-rotating investigation.

The distinct change of eigenfrequencies dominated by the bearing stiffness is evident. Comparing the results for the non-rotating and rotating versions we notice that one dominating peak is missing in the rotating version, i.e., the one at 2490 Hz. The eigenmode of this peak is a combination of housing and shaft movements and is apparently changed due to the extension mounted to the housing.

The comparison between the measurements and the simulations shows good agreement for the non-rotating as well as for the rotating setup. As such it can be concluded that the analytical bearing-stiffness matrix seems to be an adequate representation of the actual bearing's dynamics for the ball type in the observed speed range.

4.3 Tapered-roller Bearings

The TRBs, as given in Table 1, are inserted into the system. Fig. 10 shows the amplitude comparison between the measured and calculated results. Both spectra have marked regions where the eigenfrequencies shift with respect to the inserted preload. Comparing the spectra it is clear that the positions of the regions differ tremendously. Investigating the eigenmodes gives us an insight into the problem. Fig. 11 shows all the calculated eigenmodes of the test device within the marked

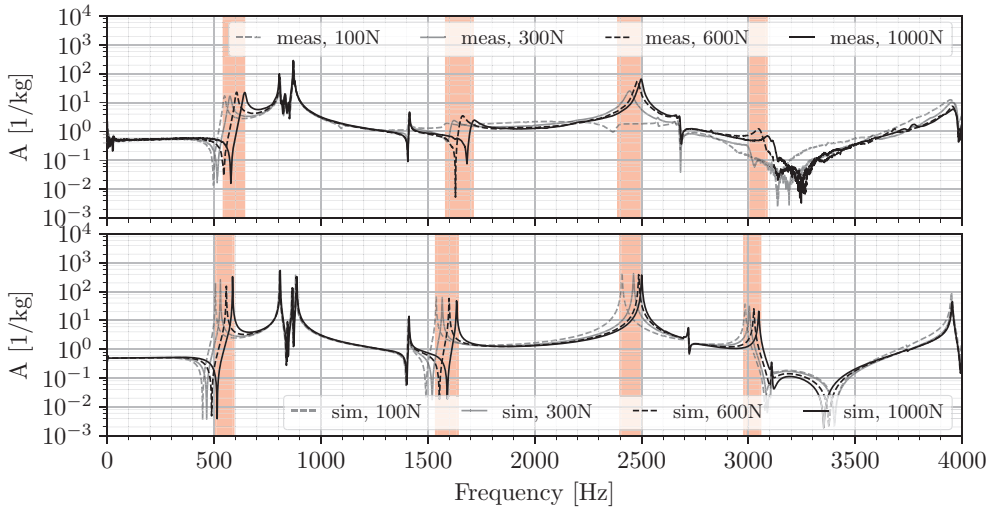

Fig. 7. *Comparison between the measured (upper part) and calculated (lower part) load-dependency of the chosen FRF for the test device with inserted ball bearings*

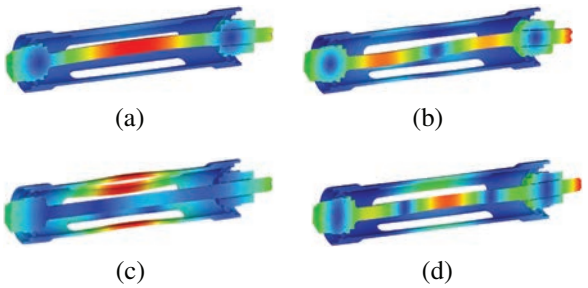

Fig. 8. *Selected calculated eigenmodes of the test device with ball bearings; a) Eigenmode at 590 Hz, b) Eigenmode at 1650 Hz, c) Eigenmode at 2490 Hz, and d) Eigenmode at 3085 Hz*

frequency band from Fig. 10. All the presented modes are governed by the bearing stiffness and do actually correspond to the first, second and third modes of the shaft. To show the measured modes we need to do a complete experimental modal analysis (EMA). For this purpose we used an approach with a high-speed camera. The measured eigenmodes are shown in Fig. 12. The first eigenmode obviously represents the first mode of the shaft, whereas the second mode represents the combination of the dominant local housing movement and the second mode of the shaft. The arrows in Fig. 12 indicate the direction of motion, where a different colour stands for a different phase. From the presented results it can be concluded that the analytically calculated bearing-stiffness matrix for the TRBs exhibits behaviour that is much too weak. As such the current modelling approach is not an adequate representation of the TRB's dynamics.

Since the non-rotating scenario has a huge gap between the measurements and the calculations we did not continue to the rotating scenario. Instead we tried to shed some light on possible causes for the observed differences with the help of a detailed FEM bearing model, as discussed in detail in the next section.

5 NUMERICAL INSIGHT

The analytical bearing-stiffness model seems to be a good representation of reality for the ball bearing, but considerably worse for the TRB. To find the origin of the problem we built a complete, detailed, full FEM bearing model for both bearing types (see Table 1) as depicted in Fig. 13. The goal is to compare the load-displacement characteristics, where the load is exerted incrementally in the axial direction. A quasi-static load-displacement analysis was performed on the full FEM bearing model. Further, the slope of the load-displcement curve is extracted, representing the total axial stiffness in the loaded direction, which is also compared. Due to its completeness, the FEM model represents the reference. Besides the full FEM model and the analytical model from Lim and Singh [**6**] and [**7**], the results from the widely used standard ISO/TS 16281 [**11**] are also included.

The results in the form of load-displacement characteristics and the corresponding stiffness for the ball bearing are shown in Fig. 14. All three approaches result in similar characteristics. There is a minor gap between both analytical approaches, whereas the FEM yields a slightly higher stiffness at a high preload.

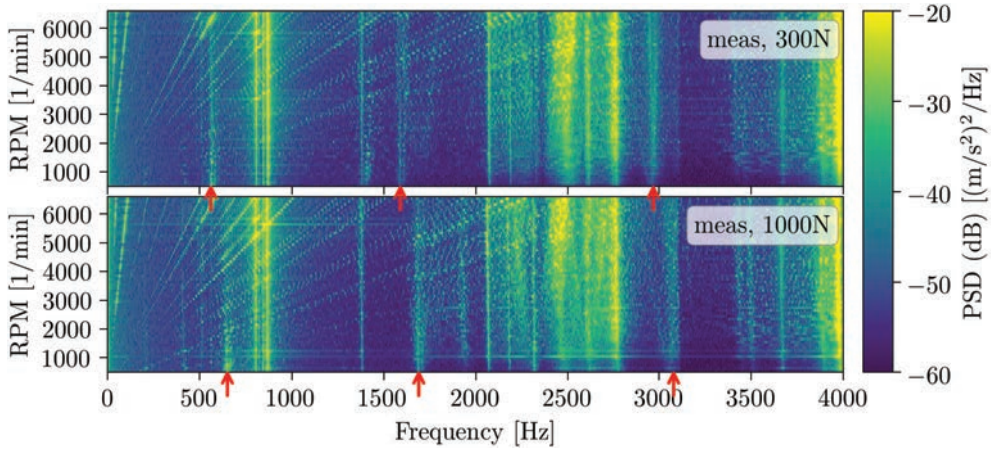

Fig. 9. *Campbell diagrams for the test device with inserted ball bearings loaded under 300 N and 1000 N*

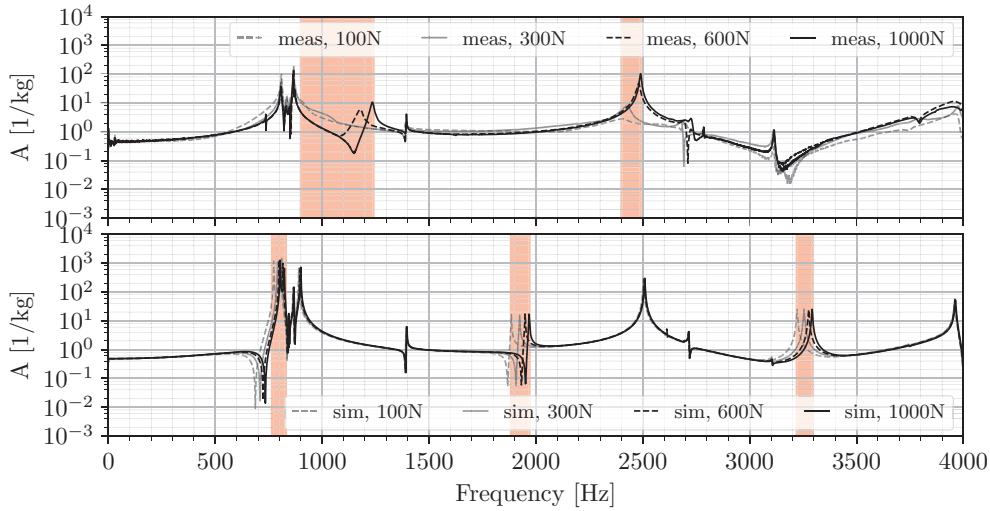

Fig. 10. *Comparison between the measured (upper part) and calculated (lower part) load dependency of the chosen FRF for the test device with inserted TRBs*

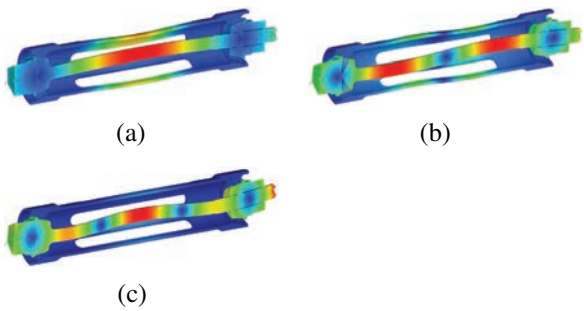

Fig. 11. *Selected calculated eigenmodes of the test device with TRB; a) Eigenmode at 820 Hz, b) Eigenmode at 1960 Hz, c) Eigenmode at 3300 Hz*

However, it can be concluded that all the models are sufficiently well correlated.

In the same manner we incrementally load the TRB in the axial direction. The results are shown in Fig. 15. The curves quantitatively differ significantly; however, they reflect the same tendency. Concerning the load-displacement characteristics, it is interesting that already both analytical approaches differ to a great extent. The same two approaches exhibit a similar level in the stiffness characteristic. The FEM model, on the other hand, yields a factor of two higher stiffness.

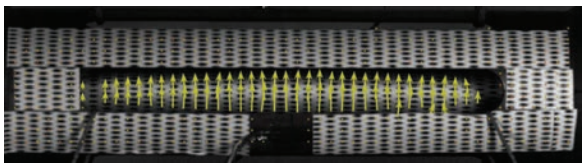

(a)

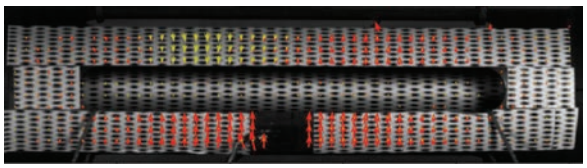

(b)

Fig. 12. *Measured eigenmodes of the test device with inserted TRB (using high-speed camera); a) Eigenmode at 1250 Hz, b) Eigenmode at 2490 Hz*

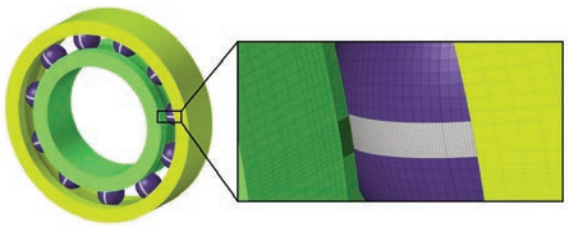

(a)

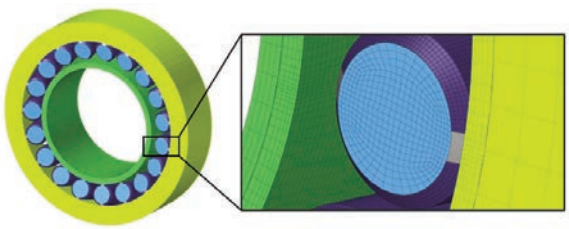

(b)

Fig. 13. *Full FEM model of a bearing; a) ball bearing, b) TRB*

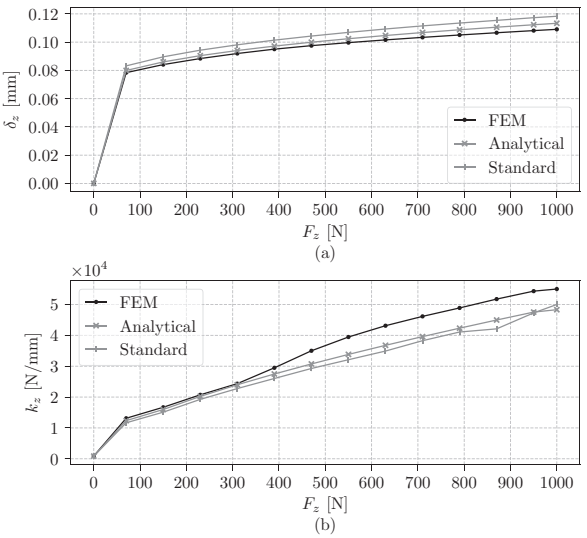

Fig. 14. *Ball bearing being incrementally loaded in the axial direction; a) load-displacement characteristic, b) corresponding total stiffness*

6 DISCUSSION

Modelling the dynamics of ball bearings with the presented approach seems appropriate. The discrepancy between the measurements and the simulations is negligible. On the other hand, the TRBs have a significant mismatch between the measured and calculated results. This is true for the dynamic testing (comparing FRFs) as well as for a simple quasi-static load-displacement investigation. The reason for such a disagreement is the inadequate bearing-stiffness model. The shortcomings can be outlined as:

1. The TRB has different contact angles in between the inner ring-roller and the outer ring-roller. The theory assumes that all the contacts are happening at the nominal contact angle, which is defined for the axis going through the centre of a roller. Consequently, no axial force is generated that pushes the rollers out of the initial contact and no flange is needed to prevent the rollers from escaping the contact. The roller-flange contact is thus neglected. This contact carries only minimal load; however, it should not be neglected, especially if the TRB is loaded in the axial direction only. It is important to note that the literature provides some theories that take into account different contact angles and flange contacts [**8**] and [**21**]. However, those theories provide a negligibly different stiffness matrix compared to the theory, which does not include the mentioned contacts. Having looked at the results, the stiffness should be of factorial difference.

2. Friction effects are neglected in all models, i.e., analytical, standard and FEM model. When the bearing operates in the hydrodynamic regime, the friction is expected to be very small and as such it is justified to neglect it in the stiffness calculation. However, when the bearing operates in the boundary or mixed-lubrication regime, the friction coefficients are expected to have a significant influence on the bearing's stiffness. Further, the dynamic load from the eigenmodes is expected to be small enough to not cause the transition from the stick to the slip state in the contact along the roller's line of action. That

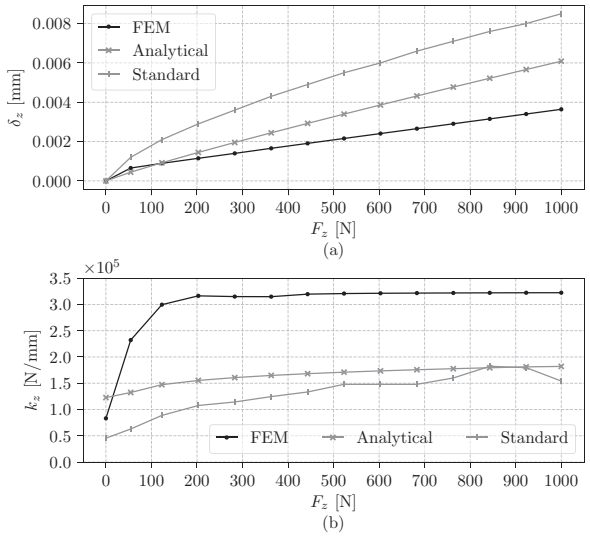

Fig. 15. *TRB being incrementally loaded in the axial direction; a) load-displacement characteristic, b) corresponding total stiffness*

being said, the stiffness of the TRB would have been significantly increased when the friction phenomena were also taken into account.

7 CONCLUSION

A bottom-up approach to characterise a bearing's dynamics is presented. A special test device was designed and built to assess the quality of the well-established modelling approach. The dynamic properties of the system were measured in the form of FRFs, where load-dependent nonlinearities, resulting from the bearings were observed. It was shown that the ball bearing model yields appropriate results, whereas the TRB model requires modifications. These outcomes were confirmed with a quasi-static, load-displacement numerical insight, where a full FEM model serves as a reference.

In future work it will be of great interest to see how a TRB reacts when loaded in other than the pure axial direction. In addition, the influence of a different lubrication regime would shed some light on questions relating to the friction. The presented study represents a good starting point for a possible new TRB model derivation.

8 ACKNOWLEDGEMENT

The authors would like to thank the ZF Friedrichshafen AG for supporting this research.

9 REFERENCES

[1] Jones, A.B. (1960). A general theory for elastically constrained ball and radial roller bearings under arbitrary load and speed conditions. *Journal of Basic Engineering*, vol. 82, no. 2, p. 309-320, **DOI:10.1115/1.3662587**.

[2] Harris, T.A. (1984). *Rolling Bearing Analysis*, John Wiley, New York.

[3] Rao, J.S. (1983). *Rotor Dynamics*, John Wiley, New York.

[4] While, M.F. (1979). Rolling element bearing vibration transfer characteristics: Effect of stiffness. *Journal of Applied Mechanics*, vol. 46, no. 3, p. 677-684, **DOI:10.1115/1.3424626**.

[5] Gargiulo, E.P. (1980). A simple way to estimate bearing stiffness. *Machine Design*, vol. 52, p. 107.

[6] Lim, T.C., Singh, R. (1990). Vibration transmission through rolling element bearings, part 1: Bearing stiffness formulation. *Journal of Sound and Vibration*, vol. 139, no. 2, p. 179-199, **DOI:10.1016/0022-460X(90)90882-Z**.

[7] Lim, T. C., Singh, R. (1994). Vibration transmission through rolling element bearings, part 5: Effect of distributed contact load on roller bearing stiffness matrix. *Journal of Sound and Vibration*, vol. 169, no. 4, p. 547-553, **DOI:10.1006/jsvi.1994.1033**.

[8] Mul, J. M., Vree, J.M., Maas, D.A. (1989) Equilibrium and Associated Load Distribution in Ball and Roller Bearings Loaded in Five Degrees of Freedom While Neglecting Friction-Part I: General Theory and Application to Ball Bearings. *Journal of Tribology*, vol. 111, no. 1, p. 142-148, **DOI:10.1115/1.3261864.**

[9] Lim, T.C., Singh, R. (1990). Vibration transmission through rolling element bearings, part 2: System studies. *Journal of Sound and Vibration*, vol. 139, no. 2, p. 201-225, **DOI:10.1016/0022-460X(90)90883-2**.

[10] Mul, J.M., Vree, J.M., Maas, D.A. (1989). Equilibrium and associated load distribution in ball and roller bearings loaded in five degrees of freedom while neglecting friction-Part II: Application to roller bearings and experimental verification. *Journal of Tribology*, vol. 111, no. 1, p. 149-155, **DOI:10.1115/1.3261865**.

[11] ISO/TS 16281:2008. *Rolling Bearings - Methods for Calculating the Modified Reference Rating Life for Universally Loaded Bearings*. International Organization for Standardization, Geneva.

[12] Cao, H., Niu, L., Xi, S., Chen, X. (2018). Mechanical model development of rolling bearing-rotor systems: A review. *Mechanical Systems and Signal Processing*, vol. 102, p. 37-58, **DOI:10.1016/j.ymssp.2017.09.023**.

[13] Guo, Y., Parker, R. G., (2012). Stiffness matrix calculation of rolling element bearings using a finite element/contact mechanics model. *Mechanism and Machine Theory*, vol. 51, p. 32-45, **DOI:10.1016/j.mechmachtheory.2011.12.006**.

[14] Fang, B., Zhang, J., Yan, K., Hong, J., Yu Wang, M. (2019). A comprehensive study on the speed-varying stiffness of ball bearing under different load conditions. *Mechanism and Machine Theory*, vol. 136, p. 1-13, **DOI:10.1016/j.mechmachtheory.2019.02.012**.

[15] Razpotnik, M., Čepon, G., Boltežar, M. (2018). A smooth contact-state transition in a dynamic model of rolling-element bearings. *Journal of Sound and Vibration*, vol. 430, p. 196-213, **DOI:10.1016/j.jsv.2018.05.041**.

[16] Kabus, S., Hansen, M.R., Mouritsen, O. (2012). A new quasi-static cylindrical roller bearing model to accurately consider non-hertzian contact pressure in time-domain simulations. *Journal of Tribology*, vol. 134, no. 4, art. ID 041401, **DOI:10.1115/1.4007219**.

[17] Kabus, S., Hansen, M., Mouritsen, O. (2014). A new quasi-static multi-degree of freedom tapered roller bearing model to accurately consider non-Hertzian contact pressures in time-domain simulations. *Proceedings of the Institution of ol. Mechanical Engineers, Part K: Journal of Multi-body Dynamics*, vol. 228, no. 2, **DOI:10.1177/1464419313513446**.

[18] Creju, S., Bercea, I., Mitu, N. (1995). A dynamic analysis of tapered roller bearing under fully flooded conditions. Part I: Theoretical formulation. *Wear*, vol. 188, no. 1-2, p. 1-10, **DOI:10.1016/0043-1648(94)06551-9**.

[19] Cretu, S., Mitu, N., Bercea, I. (1995). A dynamic analysis of tapered roller bearings under fully flooded conditions part 2: results. *Wear*, vol. 188, no. 1-2, p. 11-18, **DOI:10.1016/0043-1648(94)06552-7**.

[20] Tong, V.C., Hong, S.W. (2014). Characteristics of tapered roller bearing subjected to combined radial and moment loads. *International Journal of Precision Engineering and Manufacturing-Green Technology*, vol. 1, no. 4, p. 323-328, **DOI:10.1007/s40684-014-0040-1**.

[21] Tong, V.C., Hong, S.W. (2015). Effects of roller profile on the stiffness of tapered roller bearings. *Journal of Automation and Control Engineering*, vol. 3, no. 2, p. 151-156, **DOI:10.12720/joace.3.2.151-156**.

[22] Zhao, J.-S. Liu, W., Zhang, Y., Feng, Z.-J., Ye, J., Niu, Q.-B. (2013). Effects of gyroscopic moment on the damage of a tapered roller bearing. *Mechanism and Machine Theory*, vol. 69, p. 185-199, **DOI:10.1016/j.mechmachtheory.2013.06.002**.

[23] Roda-Casanova, V., Sanchez-Marin, F. (2017). Contribution of the deflection of tapered roller bearings to the misalignment of the pinion in a pinion-rack transmission. *Mechanism and Machine Theory*, vol. 109, p. 78-94, **DOI:10.1016/j.mechmachtheory.2016.11.013**.

[24] Houpert, L. (2002). Ball bearing and tapered roller bearing torque: analytical, numerical and experimental results. *Tribology Transactions*, vol. 45, no. 3, p. 345-353, **DOI:10.1080/10402000208982559**.

[25] Ai, S., Wang, W., Wang, Y., Zhao, Z. (2015). Temperature rise of double-row tapered roller bearings analyzed with the thermal network method. *Tribology International*, vol. 87, p. 11-22, **DOI:10.1016/j.triboint.2015.02.011**.

[26] Tong, V.-C., Hong, S.-W. (2016). The effect of angular misalignment on the running torques of tapered roller bearings. *Tribology International*, vol. 95, p. 76-85, **DOI:10.1016/j.triboint.2015.11.005**.

[27] Zhou, R.S., Hoeprich, M.R. (1991). Torque of tapered roller bearings. *Journal of Tribology*, vol. 113, no. 3, p. 590-597, **DOI:10.1115/1.2920664**.

[28] Gradu, M. (2000). Tapered roller bearings with improved efficiency and high power density for automotive transmissions. *SAE 2020 World Congress*, **DOI:10.4271/2000-01-1154**.

[29] Wrzochal, M., Adamczak, S., Domagalski, R., Piotrowicz, G., Wnuk, S. (2022). New device proposed for industrial measurement of rolling bearing friction torque. *Strojniški vestnik - Journal of Mechanical Engineering*, vol. 68, no. 10, p. 610-622, **DOI:10.5545/sv-jme.2022.275**.

[30] Zhang, J., Fang, B., Zhu, Y., Hong, J. (2017). A comparative study and stiffness analysis of angular contact ball bearings under different preload mechanisms, *Mechanism and Machine Theory*, vol. 115, p. 1-17, **DOI:10.1016/j.mechmachtheory.2017.03.012**.

[31] Altair Optistruct Eng. (2017). *Altair Optistruct Reference Guide*, Troy.

[32] Sheng, X., Li, B., Wu, Z., Li, H. (2014). Calculation of ball bearing speed-varying stiffness. Mechanism and Machine Theory, vol. 81, p. 166-180, **DOI:10.1016/j.mechmachtheory.2014.07.003**.

Strojniški vestnik - Journal of Mechanical Engineering 69(2023)7-8, 299-307
DOI:10.5545/sv-jme.2023.539
Original Scientific Paper
Received for review: 2023-01-29
Received revised form: 2023-05-15
Accepted for publication: 2023-06-06

Applying Parametric Analysis in Enhancing Performance for Double-Layer Scissor Lifts

Anh-Tuan Dang – Dang-Viet Nguyen – Dinh-Ngoc Nguyen*
Thai Nguyen University of Technology, Vietnam

This study presents a calculation procedure of applying the statistical method in determining design parameters for double-layer scissor lifts to improve their operation (e.g., lifting height, loading, stability). By parameterizing the mounting orientation of cylinders, the working of the mechanism is summarized as functions and evaluated. To verify the accuracy of obtained equations, a 2D model of the mechanism was constructed and simulated using Working Model software. The results obtained from the simulation indicate that by adjusting the mounting positions of cylinders, the platform's position and reactions on the device can be determined, enabling improvement of the system's performance. The results obtained from the study show the practical significance of applying parametric methods to the calculating process and optimizing the structure of multiple-layer scissor lifts.

Keywords: double-layer scissor lift, cylinder's orientation, kinematic analysis, parametric method

Highlights

- *Applying parametric analysis for a distinctive model of a double-layer scissor lift to obtain the reactions of each joint in the whole mechanism.*
- *The proposed method can assist the calculation process without the need to construct 3D models for complex simulations.*
- *Based on the acquired reactions and position information, the structure of the system can be further optimized, reducing the production cost and the calculation time.*
- *From the initial design parameters, hydraulic cylinders can be easily selected to meet the designer's requirements.*

0 INTRODUCTION

Scissor lifts are popular aerial platform lifts that use a scissor-shaped mechanism to lift objects or people over short distances in height. Although the first mechanism was used in Sweden in the early 1900s, it was not until the 1970s that scissor lifts gained popularity as commonly manufactured lifting structures. To select the appropriate lift for the job, lifting height, and loading are factors to be considered when choosing the equipment.

Based on the above requirements, several studies have been conducted on devices to test their functional ability. Solmazyiğit et al. [1] proposed the construction of and successfully manufactured a scissor lift device that enables lifting loads of up to 25 tons. Pan et al. [2] conducted a falling arrest test on a multi-layer scissor lift to check the structural stability, thereby ensuring tip-over safety for the system during the dropping process. Another study by Dong et al. [3] on an actual model also shows that the tip-over potential of the scissor lift system depends on the cylinder's speed. The study also indicates that the system's stability reduces when connecting joints are severely worn, or the structure is damaged.

In addition to manufacturing and testing on real devices, other studies also focus on theoretical models to evaluate the performance of lifting systems to select the optimized layouts. Spackman [4] applied mathematical techniques to analyse the mechanism of n-layer scissor lifts. The study not only analysed the reactions in the scissor members but also presented some design issues related to actuator placement, member strength, and rigidity. Kosucki et al. [5] suggested using a volumetric controller to regulate the speed of the cylinders. With significant advantages such as a simple structure and low cost, the paper presents the possibility of extending the use of volumetric control to operate low-power driving systems. Karagülle et al. [6] employed finite element analysis (FEA) on a 3D model created in Solidworks to ascertain the internal loads acting on each component of a single-layer system. Dang et al. [7] proposed using the parametric method to model single-layer scissor lifts and construct mathematical equations to determine cylinder loads and reactions at the joints. Using the same approach, Todorović et al. [8] applied Harris Hawks optimization (HHO) to reduce mass in the mechanism frames. By solving static equations for a single-layer structure, Čuchor et al. [9] suggested an accurate method for selecting a hydraulic cylinder capable of lifting loads up to 3.5 tons.

These studies demonstrate the significant influence of the cylinder on the operation of the lifts. It can be observed that for 3D models

*Corr. Author's Address: Faculty of International Training, Thai Nguyen University of Technology, Vietnam, ngocnd@tnut.edu.vn

constructed using graphic software, the calculation process is only performed for limited positions, thus making it difficult to evaluate the overall impacts of the cylinder's operation. In contrast, employing mathematical equations as a solving approach can greatly reduce the calculation and testing time, providing a more efficient method.

In this study, a specific structure of a double-layer scissor lift consisting of two cylinders is selected for analysis (Fig. 1). By determining the mathematical relationship between the movements of the cylinders and the platform, designers can choose the suitable dimensional arrangement for the cylinders that is beneficial for the required lifting.

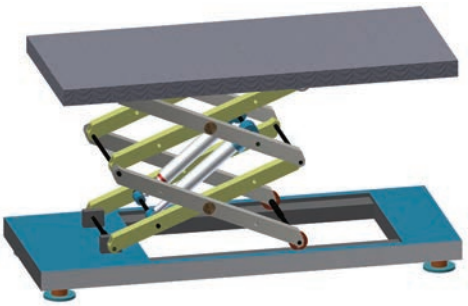

Fig. 1. *Structure of the studied system*

1 KINETIC ANALYSIS

From the 3D model of the system, a 2D model is represented, as shown in Fig. 2. The design problem can be described as follows: for a double-layer scissor mechanism with a fixed frame length a, designers must arrange two given hydraulic cylinders to utilize the maximum potential of the structure. Assuming the cylinders operate between the zero-stroke ($l_{Cyl.\min}$) and full-stroke positions ($l_{Cyl.\max}$) with a maximum thrust force F_{Cyl}, and the platform has a raising requirement ϭ Δh.

The problem then becomes one of determining the mounting position of joints P and Q in the two connected frames (AF and FC) while ensuring the stability of the lift and limiting the loading on the cylinders. Analysis of the lift construction shows that when the cylinder operates (the distance between P and Q changes), platform 5 moves to the corresponding height h. Although the length of the frames (a) and the arrangement dimensions (FQ, FP) of the cylinder are fixed, the stability of the mechanism is altered (angles γ at joints between frames E and F, and the distance l between supports A and B). Since there are too many parameter dimensions involved in the operation, designers may have difficulty choosing the correct layout to represent the movement of the platform.

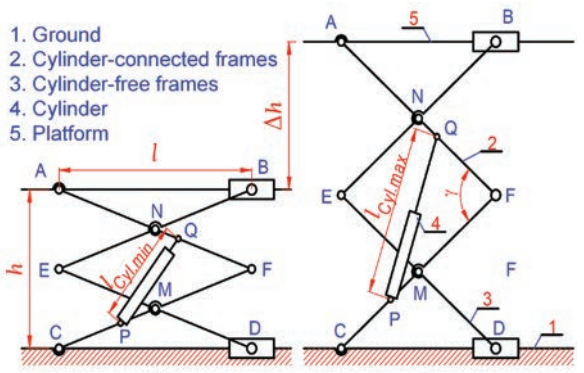

a) b)

Fig. 2. *Schematic diagram of the mechanism in: a) lowest position, and b) highest position*

Assign parameters for assembling dimensions QF = $\beta_1 \cdot a$, PF = $\beta_2 \cdot a$, and PQ = $\lambda \cdot a$ (with $0 < \beta_1, \beta_2 < 1$, $\lambda_{\max} > \lambda > \lambda_{\min} > 0$ is the length ratio of the cylinder compared to one frame); the system is parameterized as shown in Fig. 3.

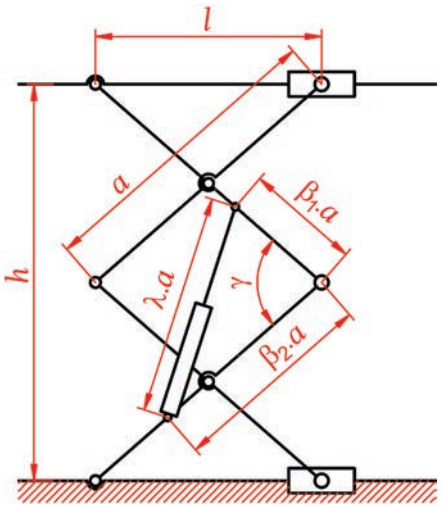

Fig. 3. *Parameterizing the device in Fig. 2*

When cylinder extends, platform height h can be calculated using the following equation:

$$h = 2a \sin\frac{\gamma}{2} = 2a\sqrt{\frac{1-\cos\gamma}{2}}. \quad (1)$$

The angle γ between frames is determined based on the relationship of the triangle MPQ:

$$\cos\gamma = \frac{\beta_1^2 + \beta_2^2 - \lambda^2}{2\beta_1\beta_2}. \quad (2)$$

Substitute Eq. (2) into Eq. (1); the height of the platform can be determined by the layout dimensions of the structure:

$$h = a\sqrt{\frac{\lambda^2 - (\beta_1 - \beta_2)^2}{\beta_1\beta_2}}. \quad (3)$$

The lifting efficiency of the system can be evaluated by the lifting ratio, which is determined by the lifting height of the platform when the cylinder extends its length from zero-stroke to full-stroke:

$$k_h = \frac{h_{\max} - h_{\min}}{a} = f\left(\lambda_{\max}, \lambda_{\min}, \beta_1, \beta_2\right). \quad (4)$$

It should be noted that when the platform is raised, γ between the frames increases and the loading distance between supports l decreases, which is also a factor affecting the stability of lift. This distance can be calculated using the equation:

$$l = a\cos\frac{\gamma}{2} = a\sqrt{\frac{(\beta_1 + \beta_2)^2 - \lambda^2}{4\beta_1\beta_2}}. \quad (5)$$

2 FORCE ANALYSIS

As described in the modelling step, due to the symmetry of the 3D structure, it is possible to investigate the reactions on the lift by analysing force on one side of the system. If the loading is 2P', the reactions at the bearings and cylinders in Fig. 2 can be correspondingly determined in terms of $P_G=(P'+W_p)/2$ (where W_p represents the weight of the platform, and G is the centroid of the total load P_G). In practice, the load on the system, specifically the lifting load P_G on the platform, may continuously change during the operation of the device. This occurs when workers walk on the platform to perform repair and maintenance tasks while the lift is still in motion. This situation not only exerts forces on joints but also causes deformation of the component frames, including bending, compression, or tensile stresses. Since these frames can be designed with rigid and sustainable materials, the impact of forces on them can be ignored, allowing the problem to be focused on revolution joints where bearings are assembled.

In the scope of this study, this paper is only concerned with analysing the static influence of forces on the structure (it considers that the load P_G is fixed on the platform during the movement of the cylinder, and the frame weight W of each frame is at its centre). This means that the distance between point G and support A is constant when lifting persons or objects from height h to h' (see Fig. 4). However, since the support distance l changes during the operation of cylinders, the magnitude of loads acting on joints A and B also changes, influencing the balance of the device and reactions on joints.

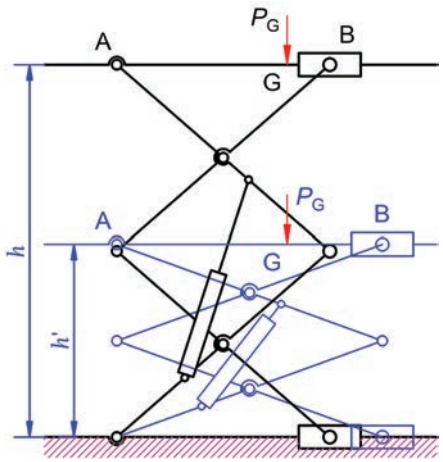

Fig. 4. *Location of load PG when the platform raises from the lowest to the highest position*

Assuming that the platform is raised slowly enough that the effect of acceleration can be ignored. Given the load on the system and the cylinder's weights are much smaller than the weight of the frames (W), the calculation of reactions on the structure can be outlined in the following steps:

First, the scissor structure is separated from moving platform 5 and ground platform 1 (see Fig. 5). Based on this figure, the reactions at supports A and B can be determined using moment equilibrium equations:

$$P_B = P_B' = \frac{P_G l_G}{l}, \quad (6)$$

$$P_A = P_A' = P_G - P_B = P_G - \frac{P_G l_G}{l}. \quad (7)$$

Similarly, the reactions at supports C and D can be calculated as:

$$P_C = P_C' = \frac{P_G l_G + 4W\frac{l}{2}}{l} = \frac{P_G l_G}{l} + 2W. \quad (8)$$

$$P_D = P_D' = P_G - \frac{P_G l_G}{l} + 2W. \quad (9)$$

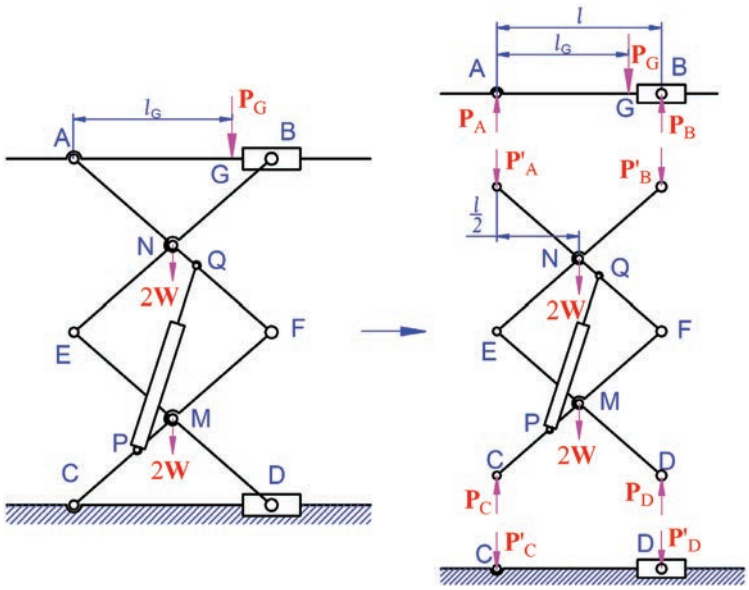

Fig. 5. *Separating component frames to determine reactions in the mechanism*

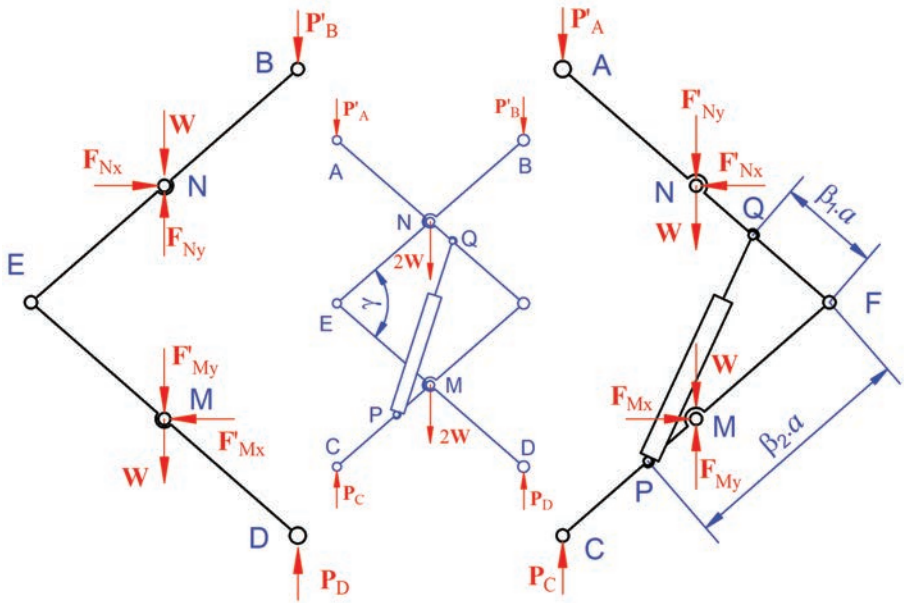

Fig. 6. *Release the connection at joints M and N*

Second, release the connection at joints M and N, and separate these reactions into directional components *Fx* and *Fy*. (see Fig. 6):

Balancing the moment in DEB frame:

$$\sum M_E = 0, \rightarrow$$

$$\left(P_D - P'_B\right) a\cos\frac{\gamma}{2} - \left(F_{Mx} + F_{Nx}\right)\frac{a}{2}\sin\frac{\gamma}{2} + \left(W_{Ny} - 2W - F_{My}\right)\frac{a}{2}\cos\frac{\gamma}{2} = 0. \qquad (10)$$

Third, continuing to release connections at E, F, and apply the moment equilibrium equation at point E for BE frame (see Fig.7);

$$\sum M_E = \left(F_{Ny} - W\right)\frac{a}{2}\cos\frac{\gamma}{2} - P'_B\, a\cos\frac{\gamma}{2} - F_{Nx}\frac{a}{2}\sin\frac{\gamma}{2} = 0. \qquad (11)$$

Draw F_{Nx} and F_{Mx} from Eq. (10):

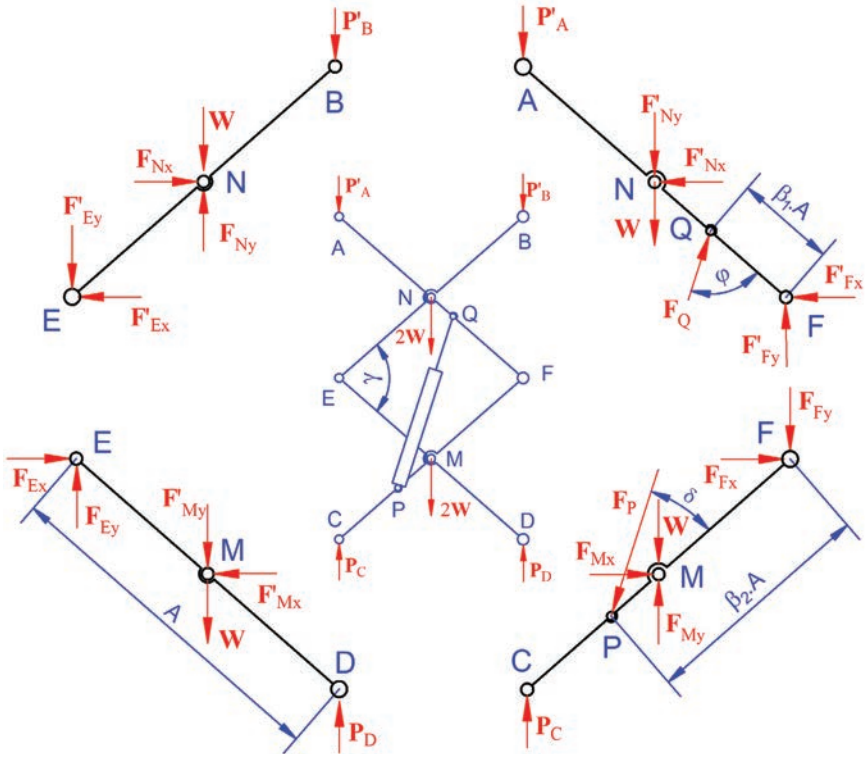

Fig. 7. *Release the connection at joints E and F*

$$F_{Nx} = F_{Mx} = \frac{W}{\tan\frac{\gamma}{2}}. \tag{12}$$

Draw F_{Ny} from Eq. (12):

$$F_{Ny} = 2P_B' + 2W = 2\left(\frac{P_G l_G}{l} + W\right). \tag{13}$$

Apply the moment equilibrium equation for AF frame:

$$\sum M_F = P_A' a\cos\frac{\gamma}{2} + \left(F_{Ny} + W\right)\frac{a}{2}\cos\frac{\gamma}{2} + F_{Nx}\frac{a}{2}\sin\frac{\gamma}{2} - F_Q\beta_1 a\sin\varphi = 0. \tag{14}$$

Substitute Eqs. (7), (12) and (13) into Eq. (14) and draw the cylinder's thrust force F_Q:

$$F_Q = \frac{\left(P_G + 2W\right)\lambda}{2\beta_1\beta_2\sin\frac{\gamma}{2}} = \frac{\left(P_G + 2W\right)\lambda}{\sqrt{\beta_1\beta_2\left[\lambda^2 - \left(\beta_1 - \beta_2\right)^2\right]}}. \tag{15}$$

It can be observed that the coefficient l_G in Eq. (15) has been omitted, implying that the position of loading P_G does not impact the magnitude of thrust force in cylinders. However, as this parameter remains present in the reaction at other joints, their magnitudes will vary and influence the stability of the system. By applying the equilibrium equation for frame AF, directional reactions at joint F can be computed as:

$$F_{Fx} = F_Q\cos\left(\frac{\gamma}{2} + \varphi\right) - F_{Nx}, \tag{16}$$

$$F_{Fy} = -F_Q\cdot\sin\left(\varphi + \frac{\gamma}{2}\right) + F_{My} + P_A' + W. \tag{17}$$

Subtitle β_1, β_2 and λ into these equations:

$$F_{Fx} = \left[\frac{\left(P_G + 2W\right)\left(\beta_2 - \beta_1\right)}{2\beta_1\beta_2} - W\right]\sqrt{\frac{\left(\beta_1 + \beta_2\right)^2 - \lambda^2}{\lambda^2 - \left(\beta_1 - \beta_2\right)^2}}, \tag{18}$$

$$F_{Fy} = P_G + \frac{P_G l_G}{a}\sqrt{\frac{4\beta_1\beta_2}{\left(\beta_1 + \beta_2\right)^2 - \lambda^2}} + 3W - \frac{\left(P_G + 2W\right)\left(\beta_1 + \beta_2\right)}{2\beta_1\beta_2}. \tag{19}$$

The total reactions in the remaining joints can be determined by combining their directional components:

$$F_E = \sqrt{F_{Ex}^2 + F_{Ey}^2}, \tag{20}$$

$$F_{\mathrm{F}} = \sqrt{F_{\mathrm{Fx}}^2 + F_{\mathrm{Fy}}^2}, \tag{21}$$

$$F_{\mathrm{M}} = F_{\mathrm{N}} = \sqrt{F_{\mathrm{Nx}}^2 + F_{\mathrm{Ny}}^2}. \tag{22}$$

3 RESULTS

To validate the accuracy of the calculation method, five 2D physical models were created using Working

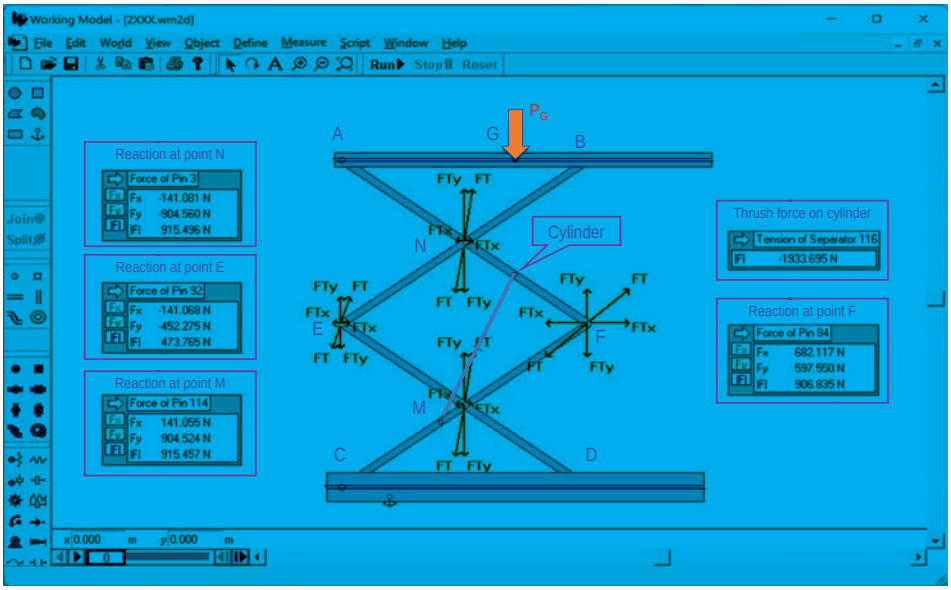

Fig. 8. *Export reactions at joints using Working Model*

Table 1. *Compare result of forces between calculation method and 2D model simulation*

$a = 1$ m; $W = 75$ N; $P_{\mathrm{G}} = 5000$ N		$l_{\mathrm{G}} = 1$ m			$l_{\mathrm{G}} = 5$ m		
		F_1 [N]	F_2 [N]	D [%]	F_1 [N]	F_2 [N]	D [%]
$\beta_1 = 0.20$ $\beta_2 = 0.65$ $l = 0.46$	FCyl	68,865.00	68,876.76	0.02	68,866.50	68,876.76	0.01
	FM	807.30	807.18	(0.01	2,657.36	2,657.27	0.00
	FE	67,138.51	67,150.27	0.02	66,835.78	6,846.14	0.02
	FF	1,288.87	1,287.93	0.07	5,224.77	5,224.64	0.00
$\beta_1 = 0.20$ $\beta_2 = 0.65$ $l = 0.74$	FCyl	17,991.60	17,992.64	0.01	17,990.90	17,992.64	0.01
	FM	938.33	938.66	0.04	4,385.43	4,386.01	0.01
	FE	12,454.58	12,455.55	0.01	9,637.26	9,638.13	0.01
	FF	1,874.53	1,875.04	0.03	8,770.51	8,771.54	0.01
$\beta_1 = 0.20$ $\beta_2 = 0.80$ $l = 0.62$	FCyl	50,998.50	51,102.72	0.20	51,006.00	51,102.72	0.19
	FM	693.59	695.64	0.30	2,647.89	2,650.97	0.12
	FE	49,127.06	49,227.89	0.20	48,696.98	48,839.48	0.29
	FF	1,225.13	1,228.80	0.30	5,257.09	5,261.63	0.09
$\beta_1 = 0.10$ $\beta_2 = 0.30$ $l = 0.22$	FCyl	71,199.00	71,372.29	0.24	71,226.80	71,372.29	0.20
	FM	652.18	653.41	0.19	2,678.20	2,681.35	0.12
	FE	68,427.42	68,545.39	0.17	67,549.09	67,706.62	0.23
	FF	1,215.76	1,218.03	0.19	5,334.71	5,341.76	0.13
$\beta_1 = 0.25$ $\beta_2 = 0.50$ $l = 0.30$	FCyl	26,339.80	26,351.61	0.04	26,339.80	26,351.61	0.04
	FM	665.36	666.31	0.14	2,664.44	2,664.92	0.02
	FE	23,158.51	23,169.49	0.05	22,373.90	22,385.29	0.05
	FF	1,217.95	1,219.00	0.09	5,301.81	5,302.57	0.01

with F_1 is reaction measured from Working Model;

F_2 is reaction obtained by calculation; and $\Delta = \left|\frac{F_1 - F_2}{F_2}\right| \times 100\,[\%]$ is the difference between the two methods.

Model software to measure the reactions at the joints (refer to Fig. 8). The obtained results from this step are then compared with the results calculated using equations, as presented in Table 1.

The first two models represent the results of the same structure with cylinder lengths of 0.46 m and 0.74 m, respectively. The remaining models depict structures with random cylinder orientations. The differences of less than 0.3 %, demonstrate the accuracy of the calculation model in determining the reactions in the mechanism. This indicates that we can accurately determine the design parameters without the need to construct or simulate the system in 3D virtual models, which can be time-consuming.

For detailed analyses, constraints such as the range of frame angular movement are applied ($\gamma_{min} = 10°$ and $\gamma_{max} = 120°$), the operational length of the cylinder (50 mm for zero-stroke and 80 mm for full-stroke, corresponding to $\lambda_{min} = 0.5$ and $\lambda_{max} = 0.8$ for the given model with $a = 1$ m), and the maximum thrust force $F_{Cyl} = 16$ kN. Based on this information, two graphs of lifting ratio k_h and the maximum loading for the cylinder at zero-stroke (lowest position) are constructed, as presented in Fig. 9.

The graph also indicates that to achieve the highest efficiency for the cylinder (maximum lifting ratio), the cylinder orientation must be selected as $\beta_1 = 0.31$ and $\beta_2 = 0.65$; Additionally, the loads in the other joints of this system can also be calculated, as shown in Fig. 10.

Eq. (3) shows that the position of the platform is determined by the displacement of the cylinder l_{Cyl} and the arrangement coefficients β_1, β_2. This implies that

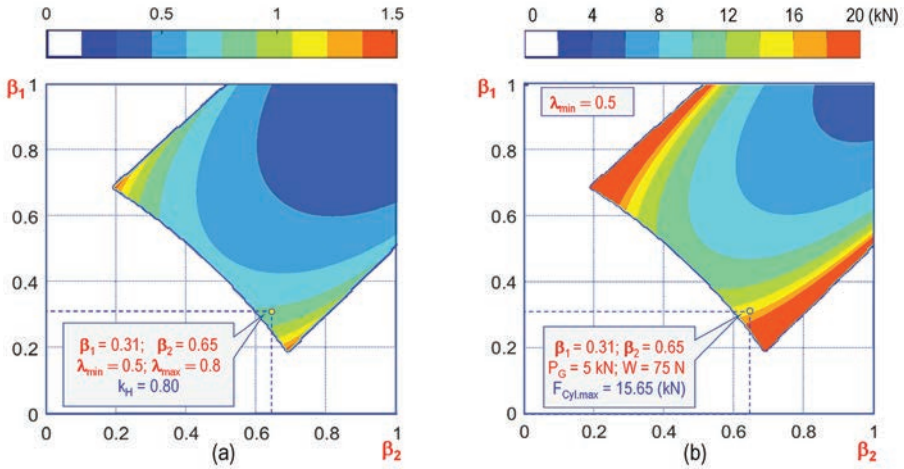

Fig. 9. *Graphs constructed from the given data (β_1, β_2); a) lifting ratio k_h, and b) maximum thrust force F_{Cyl}*

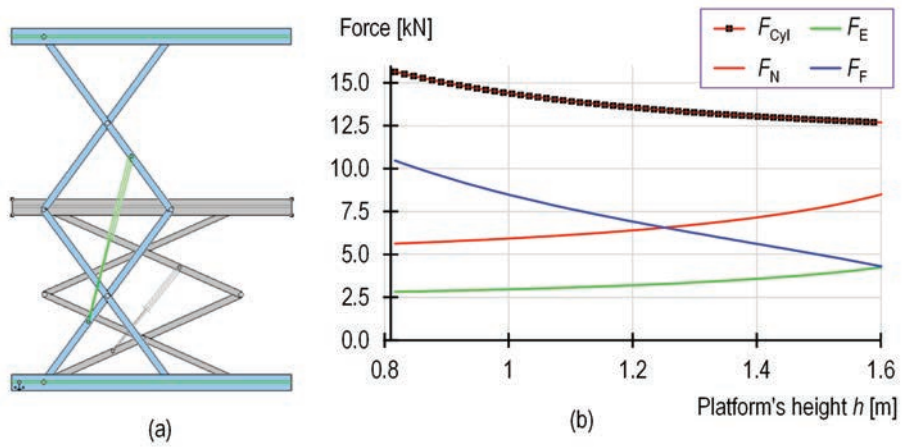

Fig. 10. *Structure of the new system: a) highest and lowest positions of the lift; and b) reactions on joints corresponding the movement of platform*

the lifting velocity of the platform can be determined by taking the derivative of Eq. (3):

$$\dot{h} = \frac{A\lambda\dot{\lambda}}{\sqrt{\beta_1\beta_2\left[\lambda^2 - \left(\beta_1 - \beta_2\right)^2\right]}}, \tag{23}$$

where $\dot{\lambda}$ is the extend rate of the cylinder.

The equation also indicates that by controlling the oil pump system, designers have the ability to modify the system's operation, particularly the movement of the platform. This feature can be achieved by using a time-control unit for the pumping system, allowing for complex platform movements. such as acquiring the complex movement of the platform by using a time-control unit for the pumping system. Fig. 11 illustrates the platform movement for a specific system selected from Fig. 10, in which the cylinder moves at different constant speeds of 1 m/s, 2 m/s, and 5 m/s. This corresponds to operation times for cylinder extension from zero stroke to full stroke length of 60 s, 150 s, and 300 s, respectively.

The results from Fig. 11 show that when the cylinder extend or raises the platform at a slower rate, there is a smaller difference in velocity during the movement. Conversely, faster movement of the cylinder leads to system instability, as varying velocity not only causes vibration but also creates acceleration and inertia forces.

Another application of the parametric method is selecting the appropriate cylinder in case the position of the cylinder has been given. For example, if the dimensions for the cylinders' arrangement are β_1 = 0.3 and β_2 = 0.6, the structure of the cylinder (length, stroke and force) can be calculated and summarized as shown in Fig. 12.

According to the requirement for structural stability, the angle γ between frames should be adjusted between 10 degrees and 120 degrees, meaning the cylinder length should be selected between 0.31 meters and 0.8 meters, according to Eq. (2).

Suppose the platform is required to be raised 0.5 meters. In that case, we can either select the cylinder with a 32 cm initial length and 12 cm stroke

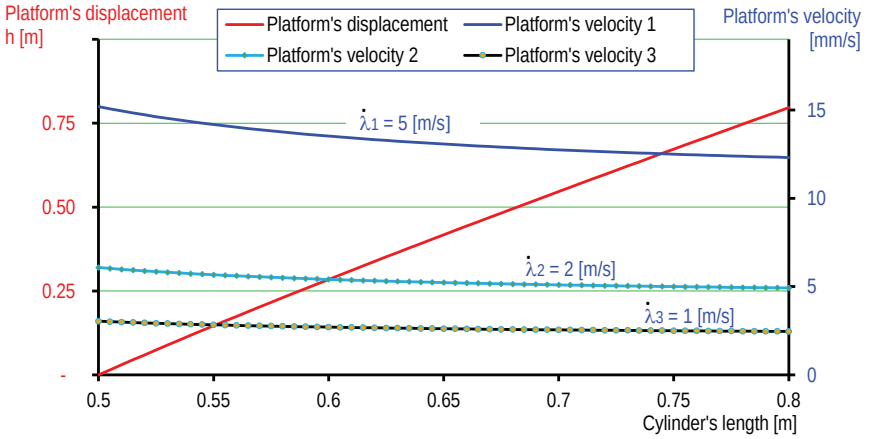

Fig. 11. *Movement of platform for selected structure with cylinder moving extends with different speeds*

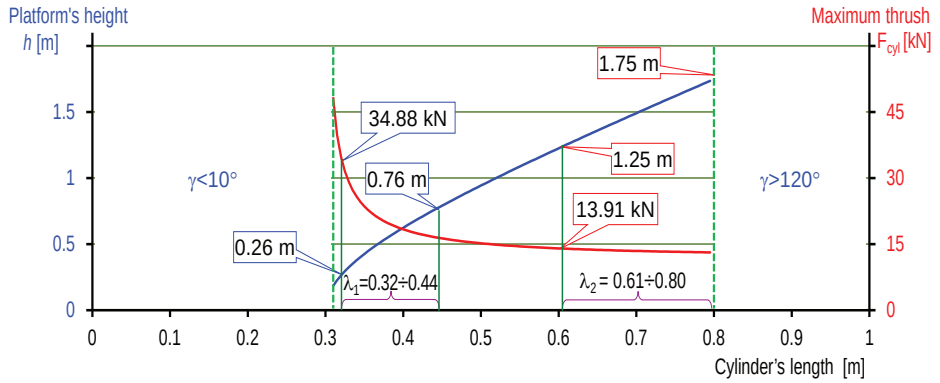

Fig. 12. *Data of cylinder corresponding to the raising height and loading requirement (a = 1 m; β_1 = 0,3; β_2 = 0,6; P_G = 5 kN; W = 75 N)*

(corresponding to h_{min} = 0.26 m and h_{max} = 0.76 m) with a maximum capacity of P_{max} = 34.88 kN or select another one with a 61 cm initial length and 19 cm stroke (h_{min} =1.25 m, and h_{max} = 1.75 m) with a maximum capacity P_{max} = 13.91 kN (having a longer stroke but a smaller thrust force requirement).

4 CONCLUSIONS

This study analyses the applicability of the parametric method in designing double-layer scissor lifts. The conclusions drawn from the study are presented as follows:

- By using simple dimensional parameters, it is possible to determine the important information of double-layer scissor lifts, such as the platform's height, cylinder's thrush force, and loading in revolution joints. This enables easy component selection without the need for complex 3D modelling or experimental tests.
- The parametric method allows for efficient selection of the appropriate cylinder based on design parameters and the given requirements.
- By analysing the reactions and position of the lift, it is possible to optimize the structure of the system, leading to cost reduction and shorter calculation time.

5 ACKNOWLEDGEMENTS

The authors wish to thank Thai Nguyen University of Technology for supporting this work.

6 REFERENCES

[1] Solmazyiğit, İ., Başkurt, R.C., Ovalı, İ., Tan, E. (2022). Design and prototype production of scissor lift platform 25 tons capacity. *The European Journal of Research and Development*, vol. 2, no. 4, p. 326-337, **DOI:10.56038/ejrnd.v2i4.177**.

[2] Pan, C.S., Powers, J.R., Hartsell, J.J., Harris, J.R., Wimer, B.M., Dong, R.G., Wu, J.Z. (2012). Assessment of fall-arrest systems for scissor lift operators: computer modeling and manikin drop testing. *Human Factors*, vol. 54, no. 3, p. 358-372, **DOI:10.1177/0018720811425024**.

[3] Dong, R.G., Pan, C.S., Hartsell, J.J., Welcome, D.E., Lutz, T., Brumfield, A., Harris, J.R., Wu, J.Z., Wimer, B., Mucino, V., Means, K. (2012). An investigation on the dynamic stability of scissor lift. *Open Journal of Safety Science and Technology*, vol. 2, no. 1, p. 8-15, **DOI:10.4236/ojsst.2012.21002**.

[4] Spackman, H. M. (1989). Mathematical Analysis of Scissor Lifts. Naval Ocean Systems Center San Diego Ca.

[5] Kosucki, A., Stawiński, Ł., Morawiec, A., Goszczak, J.. (2021). Electro-hydraulic drive of the variable ratio lifting device under active load. *Strojniški vestnik - Journal of Mechanical Engineering*, vol. 67, no. 11, p. 599-610, **DOI:10.5545/sv-jme.2021.7320**.

[6] Karagülle, H., Akdağ, M., Bülbül, İ. (2022). Design automation of a two scissors lift. *The European Journal of Research and Development*, vol. 2, no. 4, p. 178-191, **DOI:10.56038/ejrnd.v2i4.192**.

[7] Dang, A.T., Nguyen, D.N., Nguyen, D.H. (2021). A study of scissor lifts using parameter design. Sattler, KU., Nguyen, D.C., Vu, N.P., Long, B.T., Puta, H. (Eds) *Advances in Engineering Research and Application. Lecture Notes in Networks and Systems*, vol. 178, Springer, Cham, p. 75-85, **DOI:10.1007/978-3-030-64719-3_10**.

[8] Todorović, M., Zdravković, N. B., Savković, M., Marković, G., Pavlović, G. (2021). Optimization of scissor mechanism lifting platform members using HHO method. *The 8th International Conference, Transport And Logistics*, p. 91-96.

[9] Čuchor, M., Kučera, Ľ., Dzimko, M. (2021). Engineering design of lifting device weighing up to 3.5 tons. *Transportation Research Procedia*, vol. 55, p. 621-628, **DOI:10.1016/j.trpro.2021.07.095**.

Strojniški vestnik - Journal of Mechanical Engineering 69(2023)7-8, 308-316
DOI:10.5545/sv-jme.2023.578
Original Scientific Paper
Received for review: 2023-03-17
Received revised form: 2023-04-27
Accepted for publication: 2023-05-15

Machining of Hard-to-cut AISI 4462 Duplex Stainless Steel with an Environmentally Friendly Approach with Vortex Tube

Fikret Sönmez*
Manisa Celal Bayar University, Hasan Ferdi Turgutlu Faculty of Technology, Turkey

Machining is a manufacturing process that can be used to produce precision machine parts and has many advantages. The first is the ability to achieve superior surface quality. Tool wear is an inevitable phenomenon that occurs during machining. It is affected by many machining conditions; therefore, this process needs to be monitored and controlled. In this study, tool wear and surface roughness tests were carried out on AISI 4462 duplex stainless-steel materials, known to be a hard-to-cut material. For this purpose, tool wear and surface roughness analyses were implemented by using the environmentally friendly vortex tube cooling system in addition to wet turning conditions for the first time. For both methods, experiments were conducted at a 1 mm depth of cut, 120 m/min cutting speed, and 0.1 mm/rev feed with a 90 mm cutting length for each pass. Both tool wear and surface roughness were examined at the end of each pass. The analysis showed that wet turning gave better results in terms of tool life (19.8 minutes of tool life) compared to 11.1 minutes of tool life in vortex turning. In contrast, the surface roughness values differed up to two times in some experiments, and the vortex tube experiments gave better surface roughness values in all passes. In addition, the vortex tube experiments showed less built-up-edge (BUE) formation than the wet-turning experiments.
Keywords: vortex tube, machining, duplex stainless steel, tool life, surface roughness

Highlights
- *Tool wear is one of the most important outputs of the machining process.*
- *Estimating tool wear and modifying machining conditions based on it are important.*
- *Tool wear is directly dependent on cutting conditions, and unsuitable conditions dramatically increase wear.*
- *It is possible to reduce the surface roughness values by using a vortex tube.*
- *The surface roughness worsens due to the increase in tool wear.*

0 INTRODUCTION

Machining has many advantages over many other manufacturing methods. It is possible to achieve low surface roughness with machining, produce machine parts with high dimensional accuracy, and ensure the repeatability of the manufacturing process [1]. It is also known that machining processes are influenced by many factors, especially cutting speed, feed, and depth of cut [2] and [3]. During machining, friction occurs between the tool and the workpiece [4]. Due to this friction, the cutting tool wears out over time [5]. Tool wear is inevitable, although it is possible to reduce tool wear by choosing the right machining conditions. Machine parts can be machined with dry and wet machining methods [1]. In addition, the machining process can also be carried out using an environmentally friendly vortex tube. It is possible to transmit air cooled down to –50 °C to the contact area between the cutting tool and the workpiece by using a vortex tube. The vortex tube, also known as the Ranque-Hilsch vortex tube, is a piece of equipment that separates compressed air into two swirling streams, one hot and the other cold [6]. In addition, different cooling temperatures can be obtained by using various pressures and gases [7] and [8]. Thus, it may be possible to improve tool life and surface roughness. Machining can be used to produce parts for a wide variety of needs from many different materials. However, the machinability of some materials is more difficult compared to other materials. Stainless steel is one such material. Stainless steel materials are hard-to-cut due to their low thermal conductivity and high hardening tendency [9]. Duplex (ferritic-austenitic) stainless steels are one of the toughest stainless steels [1] and [10]. Stainless steel is one of the essential materials used by many sectors, despite being a hard-to-cut material. In addition, the development of these materials by various methods may increase the use of stainless steel [11] and [12]. Therefore, numerous researchers have attempted to investigate this material group in detail.

Szczotkarz et al. [13] analysed the values of flank wear and crater wear on AISI 316 stainless steel under different machining conditions. The researchers use dry, minimum quantity lubrication (MQL) and minimum quantity cooling lubrication (MQCL) with the addition of extreme pressure and anti-wear (EP/AW) cooling methods. The researchers emphasized that tool wear is accelerated under inappropriate cooling conditions. They also highlighted that wear is intense and tool life is completed quickly,

*Corr. Author's Address: Hasan Ferdi Turgutlu Faculty of Technology, Department of Mechanical Engineering, Manisa Celal Bayar University, Manisa 45140, Turkey, sonmezfikret@gmail.com

especially in dry machining conditions. Chen et al. [14] investigated the machinability performance of stainless-steel materials under different cutting parameters, specifically, cutting speed, feed, and depth of cut under dry cutting conditions. In their study, they inspected tool wear and surface roughness values. In the 18-minute tool life experiments, the researchers found that the tool wear first increased rapidly, then progressed at a constant speed, and then increased rapidly again. They also stated that increased tool wear had a negative effect on surface roughness. Derani et al. [15] performed tool wear and surface roughness tests on AISI 316 (austenitic) stainless steel under dry-cutting conditions. The researchers examined both nose wear and flank wear in the experiments and emphasized that nose wear accelerates faster than flank wear initially. They found that these two types of wear gradually increased, and finally, nose wear increased significantly. However, they also emphasized that despite an increase in tool wear, the surface roughness remained largely constant. Singh Bedi et al. [16] investigated tool wear on AISI 304 stainless steel under dry cutting conditions. They emphasized the increase in tool wear values over time. The researchers found flank wear, crater wear, built-up-edge (BUE), abrasion wear, and adhesion wear on the cutting tool in their investigation. The researchers also emphasized that the coating of the cutting tool is lost over time due to wear. Pekşen and Kalyon [17] carried out a tool wear analysis on AISI 430 stainless steel. Three different feeds and cutting speeds were used in these analyses. As a result of the analysis, the researchers suggested that the cutting speed and feed directly affect the tool life. The researchers also determined notch wear, crater wear, and flank wear on the cutting tool.

Yağmur [18] carried out analyses of tool wear and surface roughness using dry machining, MQL, and vortex tube cooling methods. The analyses were carried out using different cutting speeds and feeds. It has been observed that the results are close to each other in the experiments with the vortex tube and the experiments with the MQL. Therefore, in this study, it was understood that the vortex tube could be an alternative option to wet machining for machining. In their experiments with the vortex tube, Cukor et al. [6] pointed out that in some machining experiments, vortex machining may offer better tool life than wet machining. The researchers also discovered that overall production costs could be minimized using this environmentally friendly method. Pinar et al. [19] emphasized that similar results can be obtained with these two cooling methods in their experiments in which they compared vortex tube and wet machining processes. Thus, the researchers stated that it is possible to perform wet machining processes using the vortex tube method. Valic et al. [3] used different cutting speeds, feeds, and depth-of-cut parameters in their studies on X20Cr13 martensitic stainless steels. The researchers combined the vortex tube and MQL system and proposed an alternative method for machining stainless steel. In this proposed method, the air-oil mixture (vortex tube + MQL) resulted in an additional temperature reduction of -38.1 °C at the tool-work interface compared to the use of MQL alone.

The number of studies in the field of sustainable machining has been increasing. Korkmaz et al. [20] adopted dry, MQL, and nano-MQL methods for machining hard-to-cut nickel-based superalloys. As a result of the experiments, the researchers concluded that tool wear could be reduced by up to 60 % using sustainable methods. Airao et al. [21] used ultrasonic-assisted turning under dry, wet, MQL, and LCO_2 methods on hard-to-cut Ti-6Al-4V material. As a result of the experiments, the researchers proposed that LCO_2 and ultrasonic vibration could considerably reduce the specific cutting energy without sacrificing surface roughness or tool life. Shah et al. [22] used environmentally friendly lubrication techniques in their study. Electrostatic minimum quantity lubrication (EMQL), hybrid nanoparticles immersed in EMQL (HNEMQL), and electrostatic lubrication (EL) techniques were used in experiments with precipitation-hardened stainless steel. As a result, it is comprehended that the HNEMQL method provides up to 10 % lower power consumption compared to other methods. In contrast, the EL technique has the lowest tool wear. In addition, the researchers proposed that it is possible to reduce the *Ra* value by approximately 30 % with the EL technique.

In the examination of the existing literature, it is seen that while there are numerous studies on stainless steel, the number of studies on duplex stainless steel is limited. In addition, the number of studies using the vortex tube cooling method used in this study is very limited. Also, no study was found in which tool wear and surface roughness values were analysed over time.

In this study, tool wear analysis was carried out using AISI 4462 duplex stainless steel (a hard-to-cut material). Time-dependent analyses of tool wear and surface roughness values were also conducted. Furthermore, the effect of tool wear on the change in surface roughness of the machined part was thoroughly investigated.

1 MATERIALS AND METHODS

1.1 Materials

In this study, AISI 4462 (X2CrNiMoN2253) duplex stainless steel materials with a diameter of 75 mm and a length of 110 mm were used in the experiments. The chemical and mechanical properties of this material are shown in Table 1.

Table 1. *The chemical and mechanical properties of AISI 4462*

Element	C	Cr	Mo	Ni	Mn
wt.%	0.015	22.69	3.11	4.84	1.40

Mechanical properties	Yield strength [MPa]	Tensile strength [MPa]	Hardness [HBW]
Values	488	692	218

In the machining experiments, TNMG 160404-M3 (Grade TP2500) cutting inserts supplied by SECO, which were developed for P-class materials (steels), were used to clearly observe the tool wear. The utilized insert was suitable for average cutting conditions (designated as the P25 class). In addition, this insert was coated with Ti (C, N) + Al_2O_3 layers by CVD (chemical vapour deposition) method.

Moreover, a PTGNR 2020K16 tool holder with a 90° approach angle is preferred. It is crucial to determine the cutting speed, which has a prominent effect on tool wear. Depending on the material used (AISI 4462 duplex stainless steel), the cutting speed recommended by the tool manufacturer (SECO) is used as a reference. However, to observe the effect of wear more clearly, the cutting speed was preferred as 120 m/min. ISO 3685 [23], the primary standard for tool wear testing, was used to determine the cutting parameters other than the cutting speed. For this purpose, the parameters recommended by ISO 3685 were used, i.e., a depth of cut of 1 mm, a feed of 0.1 mm/rev, and a cutting-edge radius of 0.4 mm.

1.2 Methods

In the experiments, in addition to the conventional cooling approach of wet turning (5 % concentration), an environmentally friendly vortex cooling approach was also used. A vortex tube (Ranque-Hilsch vortex tube) was used to achieve a temperature of –23 °C at 5 bar pressure and measured using a K-type thermocouple and a Fluke 179 multimeter (Fig. 1).

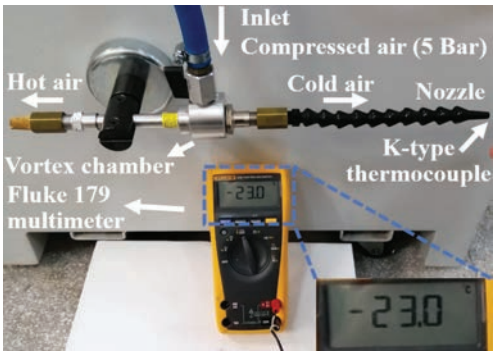

Fig. 1. *Vortex tube*

Turning experiments were carried out with a cutting length of 90 mm in each pass. After each

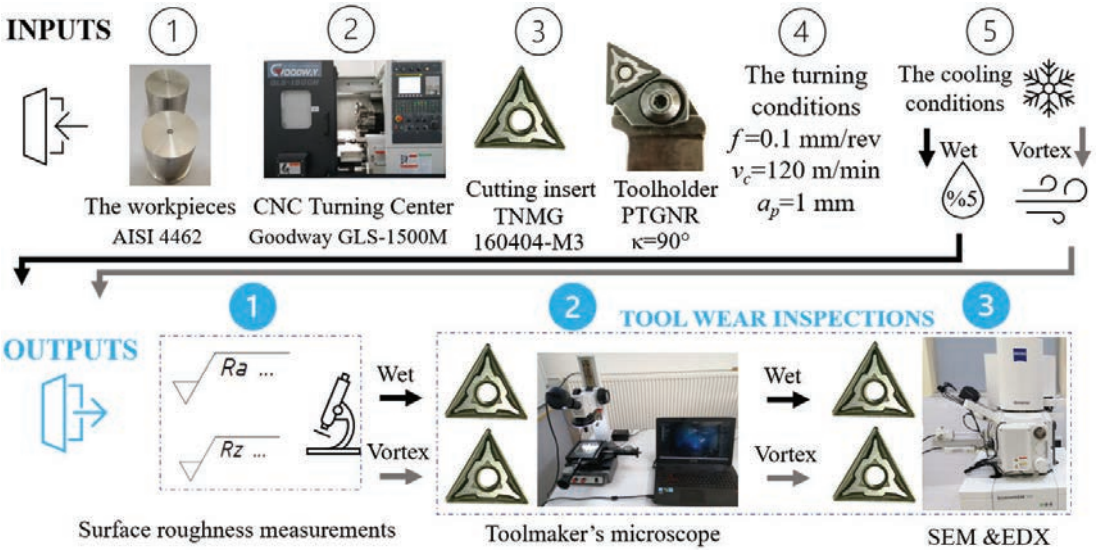

Fig. 2. *Experimental setup*

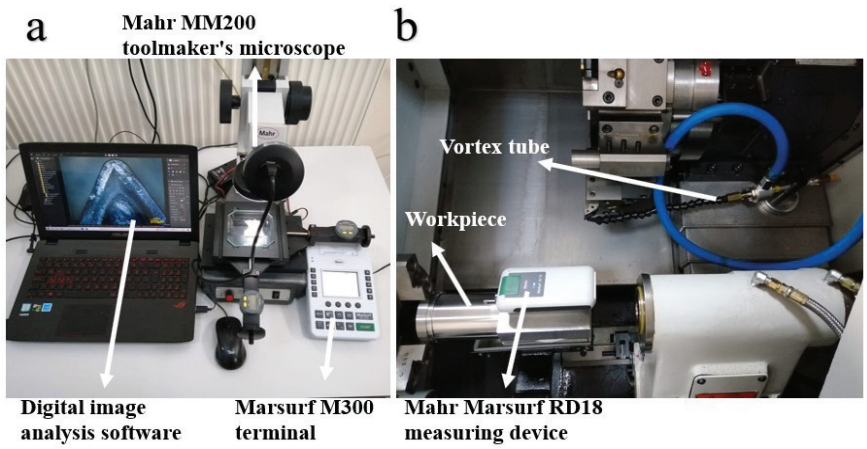

Fig. 3. *Measurement setup; a) tool wear measurement, and b) surface roughness measurement*

turning pass, the surface roughness values of the workpieces were measured according to the ISO 21920-3:2021 (formerly ISO 4288) standard [24]. The tool wear was measured by removing the cutting tool from the tool holder. Both flank wear values and notch wear values were observed in tool wear examinations. In addition, the cutting tools were examined by scanning electron microscope (SEM) and SEM energy dispersive X-ray (SEM&EDX) analysis at the end of all the experiments (Fig. 2).

The surface roughness values were measured with a Mahr M300 terminal and a Mahr Marsurf RD18 measuring device via Bluetooth connection. The tool wear measurements were performed using a Mahr MM200 toolmaker's microscope equipped with an M-shot MD30 camera via digital image analysis software (Fig. 3).

2 RESULTS AND DISCUSSION

2.1 Tool wear

Tool wear is one of the principal factors to monitor in machining. During the experiments, the cutting tool was removed from the tool holder after each pass, and the tool wear was measured, as shown in Fig. 3. The tool wear inspections performed at each pass are shown in Fig. 4.

In Fig. 4, time-dependent tool wear (flank and notch) can be clearly seen. Time-dependent tool

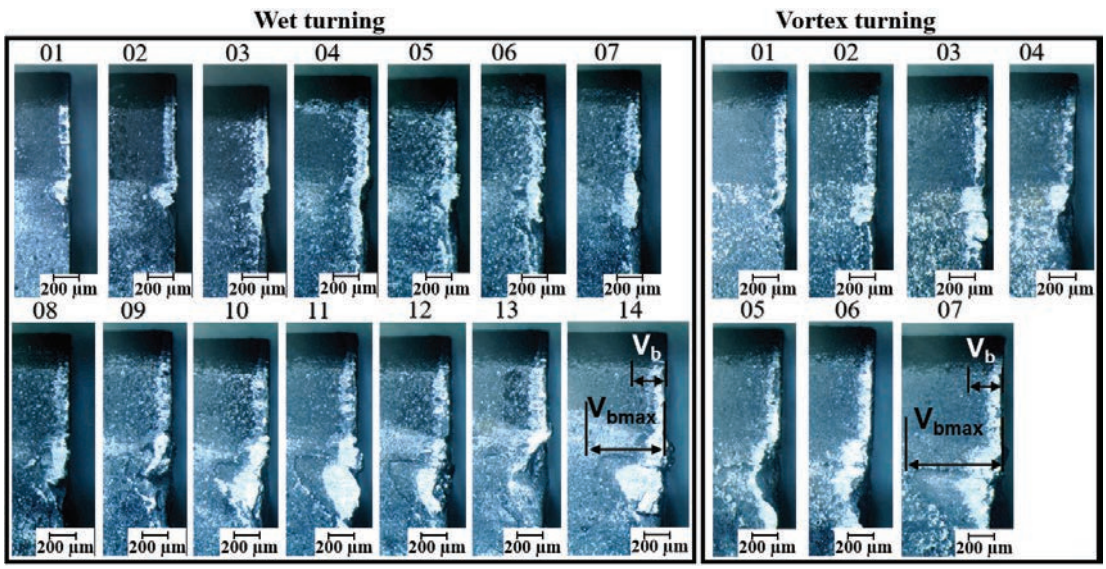

Fig. 4. *The tool wear (flank wear) inspections at each pass*

wear analysis according to tool wear inspections and measurements shown in Fig. 4 is shown in Fig. 5.

Single-point cutting tools are typically used in lathes. The tool life control of these cutting tools is carried out according to ISO 3685 [23], which specifies certain limits for tool wear. If the tool wear is regular, the flank wear limit value (V_b) is 300 µm, and if the wear is irregular, the notch wear limit value ($V_{bn\ ax}$) is 600 µm. Therefore, both flank and notch wear values were measured in the tool wear measurements. The experiments were terminated when the flank wear or notch wear value reached the limit value.

Both flank wear and notch wear increased rapidly in both wet turning and vortex cooling conditions (Fig. 5). In both cooling conditions, notch wear increased faster than flank wear; this is a known situation. Derani et al. [15] found that notch wear is more than twice as high as flank wear in the first phase of tool wear. The flank wear, in contrast, increased rapidly and then continued to do so at a constant rate almost to the end of the experiments. Acceleration of flank wear towards the end of tool life is a known fact [15] and [25]. However, in this study, an acceleration zone of the flank wear value was not detected. Notch wear is directly influenced by cooling conditions. The wear rate of the notch wear decreased with the wet turning. In the experiments performed with the vortex tube, it was determined that the value of notch wear increased dramatically at the end of the 6th pass.

In the experiments, flank wear and notch wear, which are the tool life criteria, were reached almost simultaneously. As a result of 19.8 minutes of tool life under the wet turning conditions (14th pass), the tool life was completed according to both flank wear and

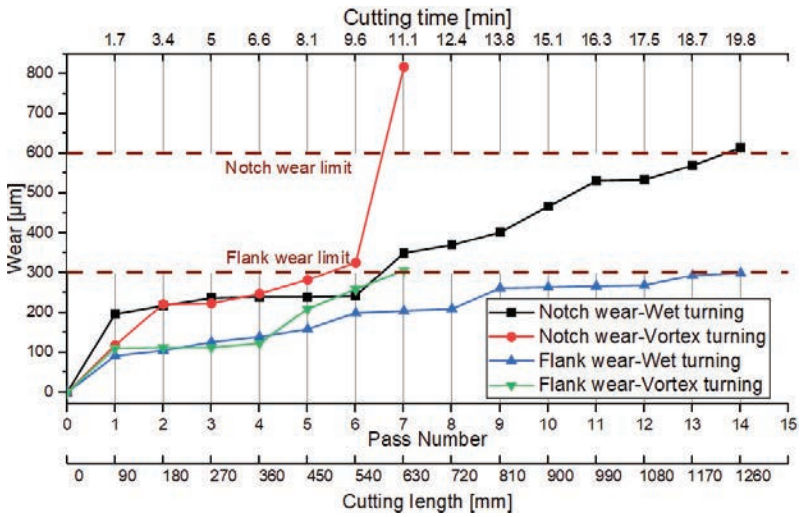

Fig. 5. *Tool wear*

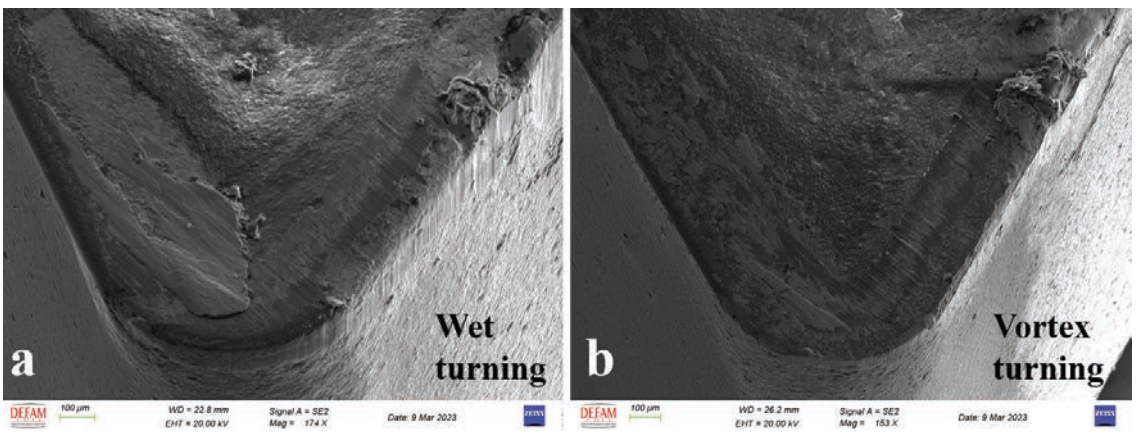

Fig. 6. *The SEM images of the cutting tools SEM images of cutting tools; a) wet turning after 19.8 minutes of cutting time, and b) vortex turning after 11.8 minutes of cutting time*

notch wear criteria. In the experiments with the vortex tube, the tool life was completed after 11.1 minutes (7th pass). When both cooling methods are evaluated together, it is comprehended that the experiments with the vortex tube have an efficiency of 56 % compared to the wet turning.

SEM analyses were carried out to compare the cutting edges concerning each other. Fig. 6 shows both the nose and top surfaces of the cutting tools employed with both cooling conditions.

Similar types of tool wear are observed on the tools in both cooling conditions (wet and vortex tube). The BUE formation is commonly observed in the machining of stainless steels [4]. However, in the wet turning conditions, significant BUE formation was detected on the top surface, whereas in the vortex tube experiments, BUE formation was limited (Fig. 6). The BUE formation observed in the wet turning cutting tool was also investigated using SEM-EDX analysis (Fig. 7).

Fig. 7a presents three selected areas for inspecting the chemical composition of the cutting insert via SEM-EDX. As can be clearly seen in Fig. 7d, the chemical composition includes significant amounts of Cr (21 %), Ni (4 %), and Mo (2 %) as determined by the examination made in the BUE observed area (red rectangle). The composition is consistent with the chemical composition of the AISI 4462 material used in the experiments and directly confirms the formation of BUE. In addition to the high W content seen in Fig. 7b, the presence of many other elements indicates both the loss of the WC insert coating and the apparent BUE formation. A significant Al content was detected in Fig. 7c. It is comprehended that it is an unworn surface since the cutting tool coating had Ti (C, N) + Al_2O_3 layers.

2.2 Surface Roughness Measurements Results

One of the most significant features desired in the mechanical parts manufactured with machining is the achievement of the expected surface roughness values. In this study, the surface roughness measurements were carried out on the computer numerical control (CNC) turning centre without removing the workpiece. Five different surface roughness measurements were taken on the workpiece, and the average of these values was calculated. The average surface roughness values obtained are illustrated in Fig. 8.

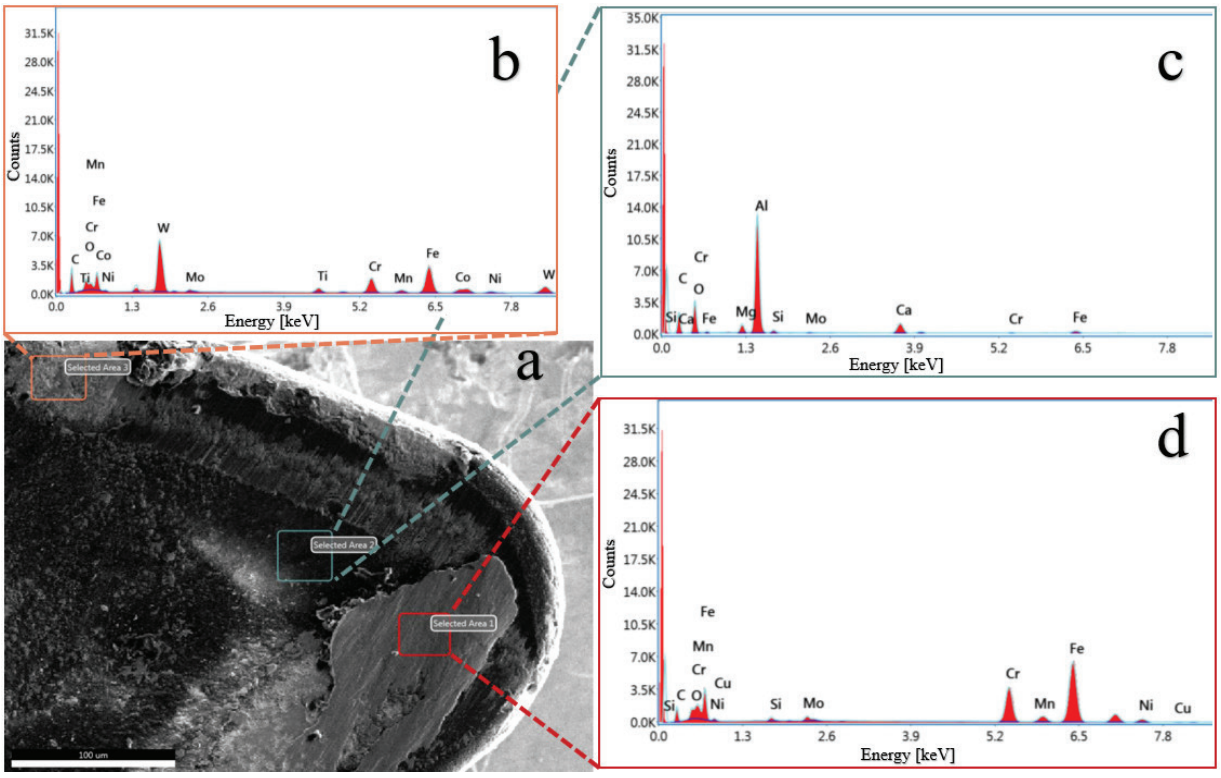

Fig. 7. *The SEM-EDX analysis of the wet turning cutting tool after 19.8 minutes of cutting time; a) top surface of the cutting tool, b) EDX analysis of area 3, c) EDX analysis of area 2, and d) EDX analysis of area 1*

It is known that surface roughness can vary depending on tool wear. In many studies, an increase in tool wear causes the deterioration of surface roughness values [26] and [27]. Selecting the appropriate experiment conditions has an outstanding influence on the surface roughness. Maruda et al. [28] used sustainable MQCL methods in turning steel materials in their study. In addition, MQCL MQCL&EP/AW was also investigated. As a result of the study, it was encountered that the surface roughness could be improved by up to 29 % with MQCL and up to 70 % with MQCL&EP/AW. Therefore, a detailed study of the effect of cooling conditions on surface roughness was conducted.

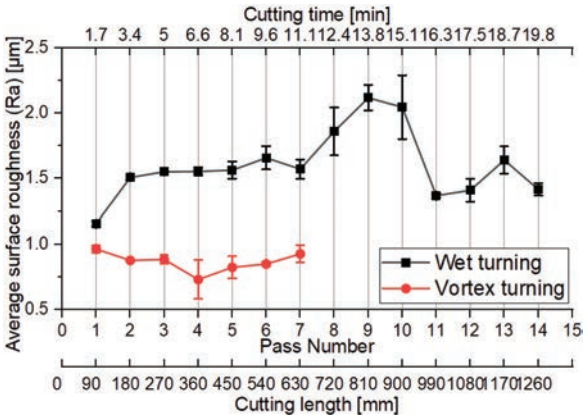

Fig. 8. *The average surface roughness (Ra) values*

Interesting results were obtained in this study. While it would be expected that the surface roughness values would be better under wet turning conditions, better results were acquired in the vortex tube experiments. The feed and cutting speed values used in the experiments and the chip breaker form of the cutting tool directly affect the chip formation. In the examinations, it was comprehended that the cutting tool could not partially perform the chip-breaking function under the current experimental conditions, and the chip could not be removed from the cutting area at some moments. Although the tool life is completed early in the experiments with the vortex tube, it is understood that much better surface quality can be obtained because it helps to remove the chips from the workpiece surface. As a result, much better surface quality was achieved in the experiments with the vortex tube. In addition, this surface quality obtained was not directly affected by tool wear, and superior results were obtained throughout all passes. This is thought to be due to the prominent BUE formation seen in cutting processes using wet turning in tool wear analyses (Fig. 7a).

In the wet turning condition, it is observed that the surface quality deteriorates over time due to tool wear. However, it is comprehended that the surface quality has improved after 15.1 minutes of tool life. This situation is also seen in some literature studies [15]. Cutting tools used in turning can provide better surface quality as a result of wear towards the end of their life [15] and [29].

The most effective parameter in evaluating surface roughness is the average surface roughness (*Ra*) parameter. However, the *Ra* parameter can only provide general information about the surface; therefore, the maximum height of the profile (*Rz*) parameter is also analysed (Fig. 9).

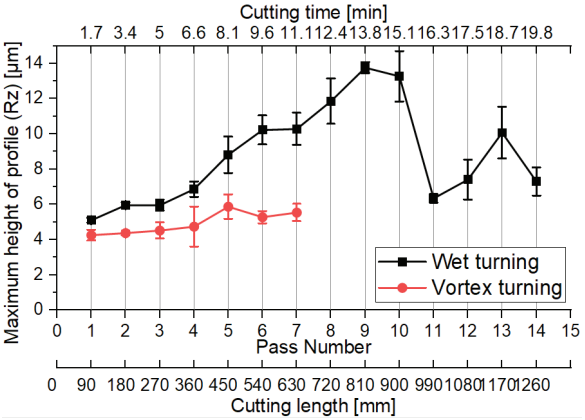

Fig. 9. *Maximum height of profile (Rz) values*

Similar to the *Ra* parameter, which gives principal information about surface roughness, vortex cooling creates better surface quality in the *Rz* parameter (Fig. 9). Under wet machining conditions, the *Rz* parameter is 5.45 times of *Ra* parameter on average, under the vortex turning conditions *Rz* parameter is 5.75 times of *Ra* parameter on average.

Tool life, workpiece surface roughness, and sustainability are the main topics of discussion in industrial machining processes. Within the scope of this study, it was found that the use of the vortex tube, which may contribute to sustainability, could be a satisfactory alternative in industrial practice, especially since it offers better surface quality.

3 CONCLUSIONS

Machining is a complex process influenced by numerous factors. Tool life and surface roughness are of immense importance in controlling this process. In this study, tool wear and surface roughness experiments were carried out on the material AISI 4462 (X2CrNiMoN2253), which is duplex stainless

steel and belongs to the class of hard-to-cut materials. The experiments were conducted at a cutting speed of 120 m/min, a depth of cut of 1 mm, and a feed of 0.1 mm/rev. Experiments were conducted with both wet and vortex tube cooling methods for the first time on AISI 4462.

Experiments were carried out with a 90-mm cutting length for each pass, and at the end of each pass, both tool wear and surface roughness were investigated. As a result of these experiments, the following results emerged:

- Tool life under wet turning conditions was completed after 19.8 minutes (14th pass) based on flank wear and notch wear standards. However, in the experiments with the vortex tube, the tool life was completed in 11.1 minutes (7th pass). The BUE formation on cutting tools was observed in both methods.
- In both wet and vortex cooling conditions, both notch and flank wear were rapidly worn within 1.4 minutes of cutting time (first pass). Both types of wear continued to increase at a constant wear rate under wet turning conditions. However, under the vortex cooling conditions, the tool was rapidly worn, especially after 6.6 minutes of cutting time, and the tool life was completed.
- Similar types of wear were observed in both wet and vortex cooling conditions. In particular, abrasion wear and the BUE formation were evident. Interestingly, however, the vortex tube experiments revealed less BUE formation than the wet-turning experiments. The interesting situation was presumably an indication of chip control problems. In vortex cooling conditions, better chip control was achieved in all experiments. In particular, the selected low feed value (0.1 mm/rev) may have caused the insert's chip breaker geometry not to function appropriately. Since the loss of chip control is due to the low feed, further studies may investigate increasing the feed values to analyse the effects of wet and vortex cooling methods.
- Better surface roughness was expected under the wet machining conditions; however, better surface roughness values (*Ra* and *Rz*) were determined in the experiments with the vortex tube. In general, vortex cooling resulted in two times better surface quality, and the lowest surface roughness was obtained with about 0.65 µm for *Ra* and about 3 µm for *Rz*. This could be explained by the fact that the BUE formation was lower in the experiments performed with the vortex tube. In addition, this situation showed that a possible consequence of the chip control problem may be seen in the surface roughness.
- Under wet machining conditions, the surface roughness deteriorated up to two times due to tool wear, reaching approximately 2.2 µm. This deterioration was not observed in the vortex tube experiments. Stable surface roughness values were mostly obtained in the vortex tube experiments, while decreasing surface roughness values were obtained in some experiments. However, it is interesting to note that some improvement in surface roughness values was detected towards the end of the tool life under wet machining conditions.
- The vortex tube, a sustainable approach, could be a suitable alternative in industrial applications, especially because it provides a higher surface quality.

According to the data obtained within the scope of this study, investigating the use of a vortex tube with the MQL system in detail in future works may be of interest. Experiments can be performed by using MQL and a vortex tube together. It would also be interesting to use nanoparticles in MQL applications. In addition, these processes can be investigated using the finite element method.

4 REFERENCES

[1] Stephenson, D.A., Agapiou, J.S. (2018). *Metal Cutting Theory and Practice.* CRC press, Boca Raton, **DOI:10.1201/9781315373119**.

[2] Tzotzis, A., García-Hernández, C., Huertas-Talón, J.-L., Kyratsis, P. (2020). 3D FE modelling of machining forces during AISI 4140 hard turning. *Strojniški vestnik - Journal of Mechanical Engineering*, vol. 66, no. 7-8, p. 467-478, **DOI:10.5545/sv-jme.2020.6784**.

[3] Šterpin Valić, G., Kostadin, T., Cukor, G., Fabić, M. (2023). Sustainable machining: Mql technique combined with the vortex tube cooling when turning martensitic stainless steel X20CR13. *Machines*, vol. 11, no. 3, art. ID 336, **DOI:10.3390/machines11030336**.

[4] Wu, J., He, L., Wu, Y., Zhou, C., Zou, Z., Zhan, G., Zhou, T., Du, F., Tian, P., Zou, Z., Zhang, X. (2021). Enhancing wear resistance and cutting performance of a long-life micro-groove tool in turning AISI 201. *Coatings*, vol. 11, no. 12, art. ID 1515. **DOI:10.3390/coatings11121515**.

[5] Baday, Ş., Ersöz, O. (2021). Comparative investigations of cryo-treated and untreated inserts on machinability of AISI 1050 by using response surface methodology, anova and taguchi design. *Proceedings of the Institution of Mechanical Engineers, Part C: Journal of Mechanical Engineering Science*, vol. 236, no. 3, p. 1751-1765, **DOI:10.1177/09544062211023117**.

[6] Cukor, G., Šterpin-Valić, G., Kostadin, T., Fabić, M. (2019). Sustainable turning of martensitic stainless steel. *Transactions of FAMENA*, vol. 43, no. 3, p. 1-12, **DOI:10.21278/tof.43301**.

[7] Pinar, A.M., Uluer, O., Kırmaci, V. (2009). Optimization of counter flow ranque-hilsch vortex tube performance using taguchi method. *International Journal of Refrigeration*, vol. 32, no. 6, p. 1487-1494, **DOI:10.1016/j.ijrefrig.2009.02.018**.

[8] Rajaguru J., Arunachalam N. (2020). A comprehensive investigation on the effect of flood and MQL coolant on the machinability and stress corrosion cracking of super duplex stainless steel. *Journal of Materials Processing Technology*, vol. 276, art. ID 116417, **DOI:10.1016/j.jmatprotec.2019.116417**.

[9] Callister Jr., W.D., Rethwisch, D.G. (2020). *Callister's materials Science and Engineering*. John Wiley & Sons, Hoboken.

[10] Ortner, H.M., Ettmayer, P., Kolaska, H. (2014). The history of the technological progress of hardmetals. *International Journal of Refractory Metals and Hard Materials*, vol. 44, p. 148-159, **DOI:10.1016/j.ijrmhm.2013.07.014**.

[11] Ali, S., Irfan, M., Niazi, U.M., Rani, A.M.A., Rashedi, A., Rahman, S., Khan, M.K.A., Alsaiari, M.A., Legutko, S., Petru, J., Trefil, A. (2022). Microstructure and mechanical properties of modified 316l stainless steel alloy for biomedical applications using powder metallurgy. *Materials*, vol. 15, no. 8, art. ID 2822, **DOI:10.3390/ma15082822**.

[12] Ali, S., Irfan, M., Muhammad Niazi, U., Rani, A.M.A., Shah, I., Legutko, S., Rahman, S., Jalalah, M., Alsaiari, M.A., Glowacz, A., AlKahtani, F.S. (2021). Synthesis, surface nitriding and characterization of ti-nb modified 316l stainless steel alloy using powder metallurgy. *Materials*, vol. 14, no. 12, art. ID 3270, **DOI:10.3390/ma14123270**.

[13] Szczotkarz, N., Mrugalski, R., Maruda, R.W., Królczyk, G.M., Legutko, S., Leksycki, K., Dębowski, D., Pruncu, C.I. (2021). Cutting tool wear in turning 316l stainless steel in the conditions of minimized lubrication. *Tribology International*, vol. 156, art. ID 106813, **DOI:10.1016/j.triboint.2020.106813**.

[14] Chen, J., Wang, Y., Zhang, Y., Yang, S., Zhang, X. (2020). Investigation on tool wear mechanism during dry cutting 304 stainless steel. *Manufacturing Technology*, vol. 20, no. 1, p. 36-44, **DOI:10.21062/mft.2020.011**.

[15] Derani, M.N., Ratnam, M.M., Nasir, R.M. (2021). Improved measure of workpiece surface deterioration during turning using non-contact vision method. *Precision Engineering*, vol. 68, p. 273-284, **DOI:10.1016/j.precisioneng.2020.12.016**.

[16] Singh Bedi, S., Prasad Sahoo, S., Vikas, B., Datta, S. (2021). Influence of cutting speed on dry machinability of AISI 304 stainless steel. *Materials Today: Proceedings*, vol. 38, p. 2174-2180, **DOI:10.1016/j.matpr.2020.05.554**.

[17] Pekşen, H., Kalyon, A. (2021). Optimization and measurement of flank wear and surface roughness via Taguchi based grey relational analysis. *Materials and Manufacturing Processes*, vol. 36, no. 16, p. 1865-1874, **DOI:10.1080/10426914.2021.1926497**.

[18] Yağmur, S. (2021). The effects of cooling applications on tool life, surface quality, cutting forces, and cutting zone temperature in turning of Ni-based Inconel 625. *The International Journal of Advanced Manufacturing Technology*, vol. 116, p. 821-833, **DOI:10.1007/s00170-021-07489-2**.

[19] Pinar, A.M., Filiz, S., Ünlü, B.S. (2015). A comparison of cooling methods in the pocket milling of AA5083-H36 alloy via Taguchi method. *The International Journal of Advanced Manufacturing Technology*, vol. 83, p. 1431-1440, **DOI:10.1007/s00170-015-7666-1**.

[20] Korkmaz, M.E., Gupta, M.K., Boy, M., Yaşar, N., Krolczyk, G.M., Günay, M. (2021). Influence of duplex jets MQL and nano-MQL cooling system on machining performance of Nimonic 80A. *Journal of Manufacturing Processes*, vol. 69, p. 112-124, **DOI:10.1016/j.jmapro.2021.07.039**.

[21] Airao, J., Nirala, C.K., Bertolini, R., Krolczyk, G.M., Khanna, N. (2022). Sustainable cooling strategies to reduce tool wear, power consumption and surface roughness during ultrasonic assisted turning of Ti-6Al-4V. *Tribology International*, vol. 169, art. ID 107494, **DOI:10.1016/j.triboint.2022.107494**.

[22] Shah, P., Khanna, N., Zadafiya, K., Bhalodiya, M., Maruda, R.W., Krolczyk, G.M. (2020). In-house development of eco-friendly lubrication techniques (EMQL, nanoparticles+EMQL and EL) for improving machining performance of 15-5 PHSS. *Tribology International*, vol. 151, **DOI:10.1016/j.triboint.2020.106476**.

[23] ISO 3685:1993. *Tool-life Testing with Single-point Turning Tools*. International Organization for Standardization, Geneva.

[24] ISO 21920-3:2021. *Geometrical product specifications (GPS) - Surface texture: Profile - Part 3: Specification operators*. International Organization for Standardization, Geneva.

[25] Letot, C., Serra, R., Dossevi, M., Dehombreux, P. (2015). Cutting tools reliability and residual life prediction from degradation indicators in turning process. *The International Journal of Advanced Manufacturing Technology*, vol. 86, p. 495-506, **DOI:10.1007/s00170-015-8158-z**.

[26] Zawada-Michalowska, M., Piesko, P., Jozwik, J. (2019). Tribological aspects of cutting tool wear during the turning of stainless steels. *Materials*, vol. 13, no. 1, art. ID 123, **DOI:10.3390/ma13010123**.

[27] Elbah, M., Yallese, M.A., Aouici, H., Mabrouki, T., Rigal, J.-F. (2013). Comparative assessment of wiper and conventional ceramic tools on surface roughness in hard turning AISI 4140 steel. *Measurement*, vol. 46, no. 9, p. 3041-3056, **DOI:10.1016/j.measurement.2013.06.018**.

[28] Maruda, R.W., Wojciechowski, S., Szczotkarz, N., Legutko, S., Mia, M., Gupta, M.K., Nieslony, P., Krolczyk, G.M. (2021). Metrological analysis of surface quality aspects in minimum quantity cooling lubrication. *Measurement*, vol. 171, art. ID 108847, **DOI:10.1016/j.measurement.2020.108847**.

[29] Niaki, F.A., Mears, L. (2017). A comprehensive study on the effects of tool wear on surface roughness, dimensional integrity and residual stress in turning IN718 hard-to-machine alloy. *Journal of Manufacturing Processes*, vol. 30, p. 268-280, **DOI:10.1016/j.jmapro.2017.09.016**.

Strojniški vestnik - Journal of Mechanical Engineering 69(2023)7-8, 317-325
DOI:10.5545/sv-jme.2023.577
Original Scientific Paper
Received for review: 2023-03-17
Received revised form: 2023-05-16
Accepted for publication: 2023-05-30

Inventory Risk Decision-Making Techniques Using Customer Behaviour Analysis

Ivan Marc – Tomaž Berlec*
University of Ljubljana, Faculty of Mechanical Engineering, Slovenia

More recent research shows the significant impact of accurate demand forecasting on the operation of supply chain system and thus on the performance of the company. Inventories in the production process could represent waste, which results in higher storage costs and consequently a higher product price, which in turn reduces company's competitiveness on the market. Nevertheless, a company must implement a lean production process and consequently carefully control storage and inventory costs. The introduction of a lean production process is closely linked to the risk of stock-outs, and knowledge of this risk in relation to customer habits is therefore a useful piece of information for the line manager's decision-making. This paper will present a mathematical model that relates customer demand for a product to the inventory level in the warehouse or between the work operations of the production process and the risk of potential penalties that arises with the introduction of a lean production process. With this model we can simulate, how to improve the production processes with still acceptable risk, with the goal of achieving a balance between stocks and the leanness of the production process. The paper demonstrates the use of a mathematical model on a concrete example from practice for risk simulation when choosing different production scenarios resulting from changed customer behaviour.

Keywords: lean production, customer demand, risk simulation, inventory optimisation

Highlights

- *A mathematical model is presented that allows fast and easy simulations of inventory management based on consumer buying behaviour.*
- *The probability density function of demand was chosen in the mathematical model.*
- *The changes in the production process can be monitored in terms of inventory costs and the risk that there may be insufficient products available to meet customer needs.*
- *By simulating three different scenarios, the optimum inventory level was found to be 30,000 pieces, at which the inventory costs are minimal with a moderate risk of 17 %.*

0 INTRODUCTION

Nowadays, companies decide to implement lean production which aims to reduce costs by eliminating all activities that do not add value [1]. In doing so, companies usually first decide to reduce inventories, that create unnecessary costs, mainly by tying up capital and occupying production areas. Of course, caution should be exercised when reducing inventory, as excessive inventory reduction can lead to business consequences and risks. It is important to determine where the lowest limit of inventory minimization can be and which parameters have a dominant influence. The aforementioned problem can be described with a mathematical model that can serve as a basis for simulating various scenarios that management can predict based on what is happening on the market. This paper presents the results of a follow-up study [2] in which, by using a mathematical model, a significant correlation between a product demand $E[X]$, the optimal inventory level z_0 and the average cost of product (ACP), as well as the impact of excess inventory and storage costs $E[C]$ in the production process on the average cost of product was demonstrated. An excess inventory level in the production process was found to raise the average cost of product ACP, weaken a company's position on the market and increase the company's inefficiency. To this end, control charts have been developed that can be used to control the inventory level in the work operations of the production process and, consequently, to control the average cost of product ACP. The paper [2] concludes with the measures to be implemented to correct the production flow y_0 and to correct the optimal inventory level z_0 in the production process depending on the changed demand $E[X]$.

Introducing lean principles into the production process means making changes to the existing production process, which often entails risks such as interruptions in the production process, non-fulfilment of contractual obligations to customers, loss of goodwill, loss of market, loss of revenue, non-competitiveness, payment of penalties, etc. This paper will therefore focus on identifying a risk β that may arise in the production process as a consequence of inventory level optimisation. A shortage of needed products may mean that customer requirements are not met and the consequences may be penalties, loss

*Corr. Author's Address: University of Ljubljana, Faculty of Mechanical Engineering, Aškerčeva 6, SI 1000 Ljubljana, Slovenia, tomaz.berlec@fs.uni-lj.si

of customers, loss of market share or even loss of market.

Using a mathematical model and simulation, we will demonstrate the possibility of implementing a lean production process using an example of inventory optimisation, so that line management will also have control over the risks associated with inventory optimisation in the production process. The mathematical model allows to simulate different production scenarios according to the customer's requirements and to determine the level of inventories so that the average cost of product is minimised.

The mathematical model can also be extended along the entire supply chain, since every link in the chain, especially the weakest one, is important for the performance, competitiveness and profitability of the entire supply chain.

The aim of this paper is to present a mathematical model and its use in a simulation to find the best ratio between customer demand for a product, the optimal inventory level, including the safety inventory, the optimal storage costs, risk, lean production process due to inventory and the average cost of product ACP. An important advantage of the simulation based on the developed mathematical model is to eliminate those scenarios where the ACP could exceed the market price due to too high storage costs.

1 LITERATURE REVIEW

In the study **[2]**, the authors identify the impact of the optimal total inventory level in the production process on the average cost of product ACP. Using a mathematical model, in which customer demand and an intermediate inventory level in the company's production process and storage costs are linked together, a negative impact of excessive intermediate inventory level on the final price of the product can be identified. In this paper, the authors prove the assumption that, in extreme cases, storage and inventory costs can cause the average cost of product ACP to rise even to a price level higher than the price recognised by the market. Seyedan and Mafakheri **[3]** state that demand forecasting and planning refer to forecasting the quantities and timeframes of customer requirements. They are of the opinion that the objective of such forecasts is to achieve customer satisfaction by meeting customer needs in a timely manner. Accurate demand forecasting could improve the efficiency and robustness of production processes and related supply chains, as resources will be matched to demands, leading to a reduction in inventories and waste.

Uhrin et al. **[4]** investigated the role of a company's external and internal resources and the impact of their variability on the degree of lean production implementation. They presented an analysis of the effects of environmental risk and past operational performance of a company on the level of lean production implementation. The paper contributes to explaining the circumstances that ultimately lead to the implementation of lean production. As a consequence, the external and internal environment influences a company's commitment to increase lean production. Petropoulos et al. **[5]** assess that demand forecasting is a prerequisite for decision-making on inventories and plays a key role in supply chain management. How to improve the accuracy of forecasts has always been a focus of research in academia and business, and the study argues that forecasts are designed to help business decisions and should be assesses on the basis of their economic implications. The study compares the performance of several commonly used forecasting methods in terms of achieving inventory control objectives, taking into account a simulation approach. The authors in **[6]** argue that for any company, in addition to reducing lead times, cost reduction is also a necessity. Therefore, monitoring and controlling manufacturing costs over time can be an important driver for improvement. In **[7]**, the authors use stochastic and hybrid models, which they consider to be very close to reality. They explain the structure of supply chains, the decisions to be taken in a typical supply chain and the models developed for supply chain planning and optimisation. The paper further explores simulation and optimisation to solve stochastic and hybrid models, their applications in the supply chain domain and future research directions arising from the emphasis on sustainability, robustness and resilience of supply chains and opportunities.

Authors in **[8]** highlight the accuracy of demand forecasting as it has a significant impact on the performance of the supply chain system and thus on the performance of company’s business operations. An accurate forecast will allow a company to make the best use of its resources. Synchronisation of customer orders with production is crucial for a timely fulfilment of orders. This paper presents a system that can improve the accuracy of demand forecasting for more efficient inventory management, also in a Smart Industry 4.0 concept. In their study **[9]**, Pusztai et al. presented a method for implementing a risk-adjusted production plan. Two examples of order allocation with inventory costing were presented, one with inventory costing and one without inventory costing. The authors consider that

such information can play a key role in the initial contract negotiations as it also includes potential risks. In their study [10], Perera et al. conclude that the success of a supply chain is highly dependent on the effectiveness of inventory management by taking into account customer behavioural patterns, which is largely neglected by decision-makers in production. In their study [11], Maheshwari et al. pointed out the problem of managing big data also in terms of customer behaviour. The role of big data analysis related to customer behaviour in supply chain management (SCM), logistics (LM) and inventory management (IM) is of paramount importance for inventory optimisation. Soares do Amaral et al. in their study [12] highlight the importance of simulation for evaluating different "what-if" system scenarios to reduce costs and risks especially in industry and service 4.0. The use of modern decision-making support analytical tools and simulation are therefore indispensable to ensure customer satisfaction and cost reduction. In the study [6] and [13], the authors present a framework for value flow optimisation by combining value flow cost and cost-time profiles. Value flow mapping represents a very effective tool for visualising activities within a production flow, focusing on the duration of activities in order to eliminate non-value-added activities. A good cost analysis system is useful and applicable in helping managers to understand the detailed costs of different short-term and long-term activities and processes, which is why stochastic production planning models have been proposed by various authors [14] and [15]. The paper [16] also proposes a stochastic production planning model to reduce risk, for a manufacturing company with seasonal demand and market growth uncertainty, to prevent excess inventory and stockout. In the paper [17] even a two-stage stochastic Linear Programming approach is proposed to investigate a production planning problem where the non-homogeneous characteristics of logs result in random process yields which are modelled as scenarios with discrete probability distributions. Paper [18] focuses on developing a stochastic approach to costing systems that considers the variability in the process cycle time of the different workstations in the assembly line and provides a range of values for the product costs, allowing for a better perception of the risk associated to these costs instead of providing a single value of the cost. The proposed model allows a better analysis of the margins and optimization opportunities as well as investment appraisal and quotation activities. Real production systems are characterised by a high degree of variability and uncertainty, which can have a drastic impact on the price of a product. Uncertainty factors in production processes are mainly demand, cycle time and available resources.

Afonso et al. [18] also used a stochastic approach to product costing in a production process. Based on their work, it is possible to further analyse the variation in costs associated with risks. They consider that the use of descriptive statistics makes sense because it gives the ability to understand and evaluate the behaviour of cycle times and their impact on costs. The approach allows for a better detection of the risks associated with product costs. In his study [19], the author concludes that non-economic theories, such as psychological or psychoanalytical theories, also allow a better understanding of other factors influencing consumer behaviour that need to be taken into account. Consumer behaviour is considered to be a holistic approach and consumer behaviour is based on perceptions towards a product. The theories and models developed in the study can serve as a basis for determining consumer buying behaviour. In [20], Radhakrishnan et al. investigate the effective inventory management in the supply chain and argue that inventory management is one of the important areas of supply chain management. They have developed a novel and efficient approach using a genetic algorithm that clearly determines the maximum possible excess inventory level and the shortage level required to optimise inventory in the supply chain. In the paper [21], Prasertwattana et al. investigate material ordering and inventory control in supply chain systems. The effect of control policies is analysed under three different configurations of supply chain systems. The authors consider that the problem is solvable using an evolutionary optimization method known as differential evolution (DE). The results show that the incentive scheme compliance policy is appropriate and outperforms other policies and can improve the efficiency of the whole system and of all members in the supply chain management framework.

Based on the literature review, a new methodology for decision-making support on inventory levels is proposed in conjunction with an analysis of the changing customer habits based on a mathematical model and simulation. We have not yet found a similar solution in the literature.

2 METHODOLOGY

Knowing the purchase behaviour of customer, a probability density function of the product demand can be determined. This information is provided by

the sales department, using data on sales in previous periods and forecasts of future sales.

The probability density function of product demand $f_X(x)$ is approximated as closely as possible to the actual purchase behaviour of the customer. The chosen probability density function, (Eq. (1)) of the demand X for product is a good approximation of the behaviour of customer demand in practice [2].

$$X \rightarrow f_X(x) = a^2 x \cdot e^{-ax}. \tag{1}$$

If the function $f_X(x)$ is multiplied by x and integrated on the interval 0 to ∞, mathematical hope $E[X]$ is obtained. The theoretical mean value of $E[X]$ (Eq. (2)) is then equated with the mean value $\bar{x}$ obtained from real customer demand data (Eg. (3)) and the constant production flow y_0 (Eq. (4)).

$$E[X] = \int_0^\infty x \cdot f_X(x)\,dx = \frac{2}{a}, \tag{2}$$

$$\frac{2}{a} = \bar{x}, \tag{3}$$

$$y_0 = \bar{x}. \tag{4}$$

If the probability density function of customer demand $f_X(x)$ is known, the probability density function of warehouse stock fluctuations $f_Z(z)$ (Eqs. (5) to (7) can also be determined.

$$\Delta Z = y_0 - X,$$

$$Z = z_0 + \Delta Z,$$

$$X = z_0 + y_0 - Z,$$

$$Z \rightarrow f_Z(z) = f_X(x)\left|\frac{dx}{dz}\right|, \tag{5}$$

$$f_Z(z) = a^2 (z_0 + y_0 - z) \cdot e^{-a(z_0 + y_0 - z)}, \tag{6}$$

$$f_Z(z) = a e^{-(az_0+2)} \left[(az_0 + 2) - az\right] e^{az}, \tag{7}$$

where ΔZ is inventory fluctuations due to variable demand X, y_0 constant production flow equal to the average demand quantity $E[X]$, X variable product demand, a parameter of probability density function of customer demand, z_0 initial inventory level, and z inventory level in warehouse or between working operations.

Fig. 1 shows the inventory cost fluctuations p, q, h in a warehouse or between work operations.

Wherein in Fig. 1 $C(z)$ represents storage cost [€], $C(z) = p$ storage cost of a product when it is not in stock [€/PC], $C(z) = q$ safety inventory costs [€/PC], $C(z) = h$ storage cost of a product when it is in stock [€/PC], s safety inventory [PC], and z the number of pieces in stock in the warehouse [PC], and PC represents piece.

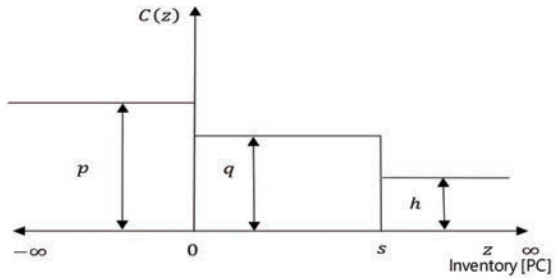

Fig. 1. *Cost fluctuations in a warehouse or between work operations*

Here, the key question is, of course, how much inventory and how much safety inventory can there be between work operations, and what are the costs and risks of: 1) not paying penalties for not delivering products to the customer on time and 2) having excess production in the warehouse and potentially being uncompetitive because of excessive storage costs?

The simplest solution is to opt for more inventory in the warehouse or between work operations, which means that excess production is created, which in turn, from the point of view of lean principles, represents wastes such as redundant transport, warehousing, processing, poorer product quality, increased warehousing costs, inefficiency, uneconomic and consequently uncompetitive business.

The solution to the problem and the elimination of waste is seen in the introduction of a lean production process with a focus on optimising inventory levels in the warehouse and between work operations. We believe that this is feasible if we have a good knowledge of the customer's buying behaviour and of the risk when interruptions (shortages) may occur in the production process. In this case, we can set an objective that the total waste in the production process or logistics chain should be minimal, which can be achieved by minimising the initial inventory z_0.

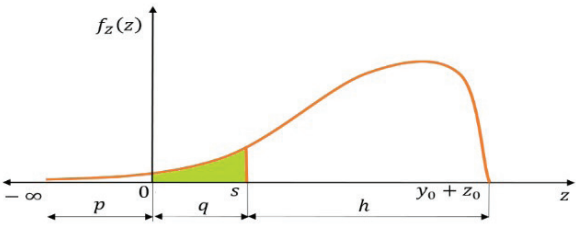

Fig. 2. *The figure shows the probability density function of inventory fluctuations*

We now define a mathematical algorithm in Eqs. (8) to (10) that will relate the parameters with each other, namely z_0 (optimal initial inventory level), the risk β of being out of stock at a given moment in the warehouse or between work operations due to interruptions in the production process, the storage costs $E[C]$ as a function of p, q and h, the safety inventory s, the customer buying behaviour $E[X]$ and the penalties Q that we will have to pay if we fail to meet demand due to a production failure. Fig. 2 shows the probability density function of inventory fluctuations in the warehouse or between two work operations in relation to the costs p, q and h. The mathematical algorithm is given by Eqs. (8) to (10).

$$E\left[C(z)\right](z_0) = \left|\int_{-\infty}^{0} p\, z f_Z(z)\,dz\right| + \int_0^s q\, z f_Z(z)\,dz + \int_s^{y_0+z_0} z h\, f_Z(z) + Q\beta, \tag{8}$$

$$E\left[C(z)\right](z_0) = hz_0 + \frac{1}{a}e^{(az_0+2)} \cdot \left\{\left[p+q+aQ+e^{as}(q-h)\cdot(as-1)\right]az_0 + 4(p+q) + 3aQ + e^{as}(q-h)\cdot(as-2)^2\right\}, \tag{9}$$

$$\frac{dE[C]}{dz_0} = 0,$$

$$z_{0optim} = \frac{he^{(az_0+2)} - 3(p+q) - 2ah - e^{as}(q-h)\left[(as-2)^2 - (as-1)\right]}{a\left[p+h+aQ+e^{as}(q-h)(as-1)\right]} \rightarrow min, \tag{10}$$

To determine the minimum value according to the proposed mathematical method, a simulation model has been developed and is shown in Fig. 3.

The simulation is carried out using the standard software tool MS Excel and is therefore easy to use, so that the line management can use it whenever there is a change in the input parameters, which depend mainly on market conditions.

The following variables appear in the simulation model, z_0 is initial inventory level [PC], s safety inventory level [PC], β risk [%], $E[C]$ average storage cost as a function of z_0 [€], and Q penalties that have to be paid due to unfulfilled requests to the customer [€].

3 CASE STUDY

In the selected company, we have carried out a material value flow analysis in the production process of a Basic hinge (Fig. 4). We have focused on the cold forming and surface protection operations. Using the proposed model, we want to determine how much inventory should be held to keep the process lean and to identify the risk β that may arise from optimising the inventory level z_0. The capacity of the Basic hinge assembly system is 68,500 PC per day, which corresponds to the customer demand ordering an average of $y_0 = E[X] = 50{,}000$ PC of hinges.

The input data of the model shown are p, q, h, s, Q, z_0 and x. The parameter a depends on customer buying behaviour, so cannot be influenced, and x represents actual monthly orders. When we enter the

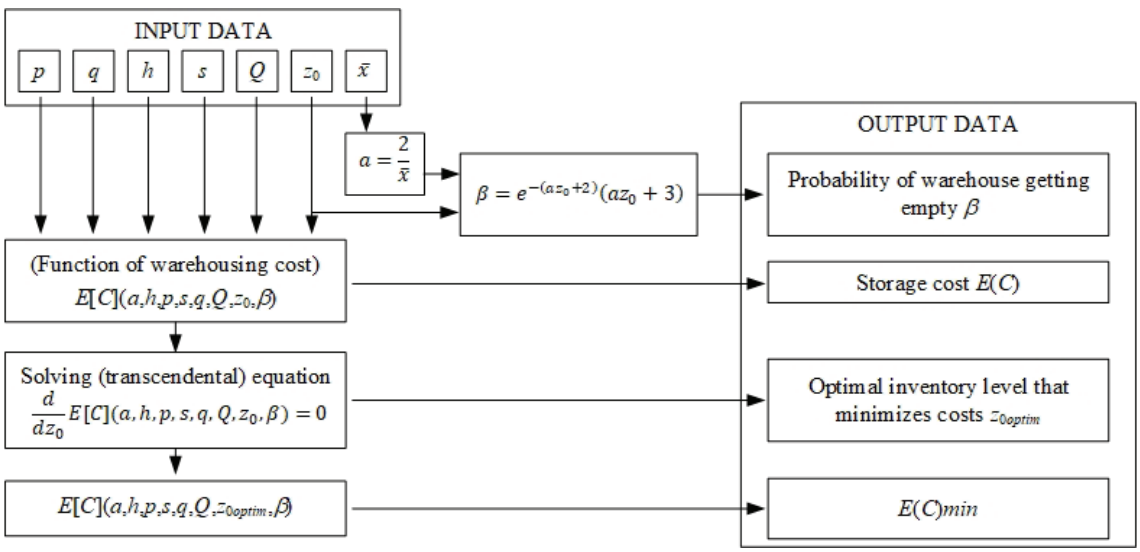

Fig. 3. *Mathematical algorithm for simulation in Excel*

input data into the Excel software using our algorithm, we get the output data β, $E[C]$ and z_0.

When we solve the equation $dE[C]/(dz_0) = 0$ using numerical calculation methods, we obtain the optimum z_{0optim}, where the cost $E[C]$ is a minimum. In the simulation we use the "What if experiments". In our example we are interested in the function $E[C]$ $(a,h,p,s,q\ Q,z_0,\beta)$. β depends indirectly on a and z_0. Using this function, in addition to z_0, we can simulate the behaviour of the cost for different values of a, h, s, q, p, Q and β.

If we want to obtain the optimal value z_{0optim} immediately, it can also be obtained by the exact mathematical Eq. (10) and the given parameters a, h, s, q p and Q without simulation. In our case, s can also be referred to as the strategic stock necessary for the smooth running of the production process.

In this paper, we have limited ourselves to presenting three scenarios using a practical example. There are many possible combinations, and the choice of the best balance between inventory, costs and risks is in the hands of management. We have found some similar studies in the literature that indicate that solving the problem from the point of view of the balance between inventory, costs and risks is important and at the same time interesting for the academic community. We believe that the proposed model is therefore interesting and useful for practice.

It can be seen from Fig. 4 that the quantity of products transported daily between the two operations, or the daily quantity demanded by the customer (Q_{td}) is Q_{td} = 50,000 PC/Wd, where Wd represents work day. The quantity of products between the two operations or the quantity of products in transition between the two operations (Q_b) is Q_b = 466,666 PC. Other used variables in Fig.4 are: W represents number of workers at the workplace, WP workplace number, Tp process time, Tc cycle time, Ts setup time, A availability, Tps process time for series, Qs quantity in one series processed and S scrap.

The status between the two operations is an interesting data point for us, because it is clearly an overproduction which represents a cost or waste for the company. We will verify the claim that waste is in question here by applying the proposed mathematical model (Eqs. (8) to (10)). Let us assume that the daily storage cost of the cup semi-finished product is h = 0.5 €/PC, the cost of storing the safety inventory of the cup semi-finished product q = 1 €/PC, the cost of the cup semi-finished product when it is not in stock p = 2 €/PC, the quantity of the safety inventory of the cup s = 1,000 PC, and the penalties to be paid if there is an interruption in the production process and we are not able to fulfil the customer's order Q = 10,000 €. The customer's average daily order is $E[X]$ = 50,000 PC of Basic hinges.

The following findings are also important for the simulation, including the data that represent limitations in the optimisation process.

The inventory level of the cup semi-finished product z_0 between the cold forming and surface protection operations in the existing production process is excessive and is in fact overproduction and waste. This is in contrast to a lean production process.

Since the inventory level is excessive, the risk β of production failure is practically non-existent or negligible.

The storage costs of excessive quantities of the cup semi-finished product are high and therefore increase the average cost of the cup semi-finished product, raising the price of the finished Basic hinge product and thus weakening the product's position on the market. Excessive inventories generate a range of different wastes (transport, additional storage space, redundant processing, increased changeover times, questionable quality and increased defect volumes).

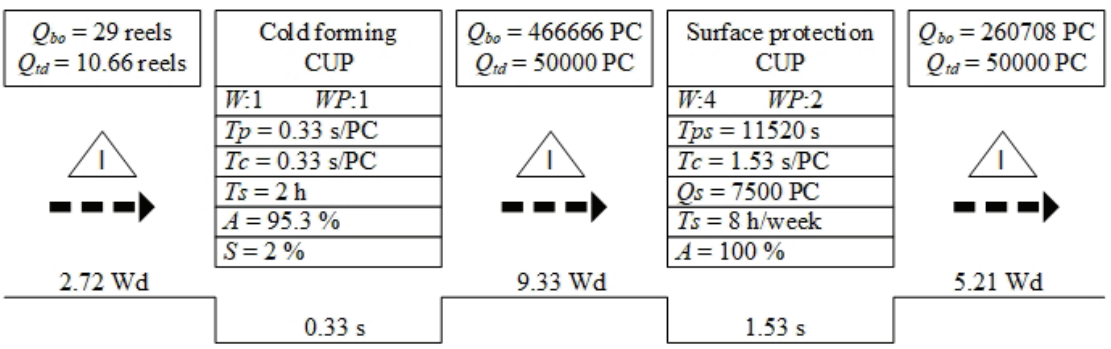

Fig. 4. *Material value flow for the Basic hinge*

4 ANALYSIS AND DISCUSSION

We have selected three scenarios to analyse the lean production process by varying the inventory level between the cold forming and surface protection operations. The simulation was carried out in MS Excel environment.

Scenario 1: Since the daily demand is 50,000 PC, the line manager in the first scenario has decided on an initial inventory z_0 = 30,000 PC, i.e., 60 % of the daily safety inventory, which can be considered as an optimistic decision because in this case there should be no production failure of more than half a day.

Scenario 2: In the second scenario, the manager has increased the initial inventory to 60,000 PC, which represents 110 % of the daily safety inventory, which can be considered a plausible scenario. Even if there is a slight change in demand, there is still one day's safety inventory if a production failure occurs.

Scenario 3: In the third scenario, the initial inventory was further increased to 100,000 PC, which represents 200 % of the daily safety inventory, which can be considered a pessimistic decision because in this case there is a safety inventory for two days of production failure.

Using the mathematical model and the simulation software developed in MS Excel, the line manager in charge of production found out very easily what the storage costs $E[C](z_0)$ and the risk β are for each scenario chosen.

Fig. 5 shows a possible choice between the optimal inventory z_0, the storage costs $E[C](z_0)$ and the risk costs β. The coloured boxes show the values for the selected values for the 3 scenarios previously proposed that could allow a lean production process in the case of reducing the inventory level of the cup semi-finished product between the cold forming and surface protection work operations.

z_0	$E[C](z_0)$	β
0	43,037.95	0.40
10,000	36,480.39	0.30
20,000	32,865.68	0.23
30,000	28,247.71	0.17
40,000	29,563.30	0.12
50,000	31,868.36	0.09
60,000	34,910.93	0.06
70,000	38,497.64	0.04
80,000	42,482.45	0.03
90,000	46,756.48	0.02
100,000	51,239.37	0.01
110,000	55,872.31	0.01
120,000	60,612.57	0.008
130,000	65,429.28	0.006

Fig. 5. *Possible choice between the inventory z_0, the storage costs $E[C](z_0)$ and risk costs β*

Fig. 6 shows the results from Fig. 5 in graphical form. Fig. 6 clearly shows where the minimum value $E[C](z_0)$ is, and hence the optimal inventory level z_0 is

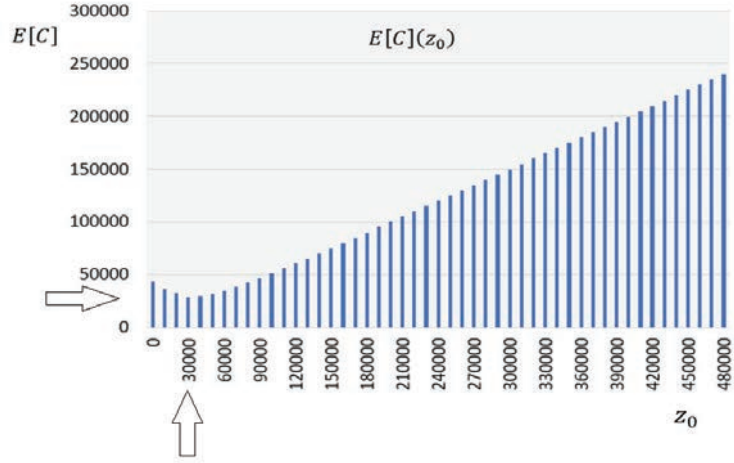

Fig. 6. *Storage cost fluctuations $E[C](z_0)$ as a function of the selected inventory level z_0*

determined. A more detailed analysis of the simulation results for all 3 scenarios is as follows:

Scenario 1: The storage costs are the lowest, $E[C](z_0)$ = 28,247.71 €. As a consequence, there is a slightly higher risk of production failure β = 17 %. In Fig. 5, Scenario 1 is indicated by the red box and in Fig. 6 it is indicated by the arrows.

Scenario 2: It represents higher storage costs $E[C](z_0)$ = 34,910.93 € but a lower risk of production failure, β = 6 %. In Fig. 5, scenario 2 is indicated by a black box.

Scenario 3: It represents even higher storage costs $E[C](z_0)$ = 51,239.37 € but the lowest risk of process disruption β = 1.7 %.

Given the target function, the optimal decision is at min z_0. This target is reached in the first scenario, where the selected quantity of the initial inventory is 30,000 PC and the cost $E[C](z_0)$ = 28,247.71 €. According to the production management, a risk of 17 % is acceptable.

Hypothetically, bearing the lean production principles in mind, we should have opted for a production without inventories, but in this case the costs are 43,037.95 € and the risk is 40.6 %, which is too high a risk. We have noted that in the mathematical model, and therefore in the simulation, the dominant variable is Z or z_0 (optimal value), since this variable affects both the cost $E[C]$ and the risk β. The larger the inventory Z, the higher the cost and the lower the risk, and vice versa. Thus, the management's decision depends mainly on the developments on the market. The greater the competition, the leaner the production process must be (because of lower costs) and the quantity Z must be close to z_0, even if the risk is higher. If the risk is higher, it means that the market situation must be closely monitored, and the simulation must be run again with the proposed model to choose a new inventory strategy adapted to the conditions.

Since we did not find a similar approach to inventory minimization in the literature, it is not possible to compare the results with other similar studies. Therefore, the management of the company in question has analysed the results in detail and found that they are useful for decision making regarding the level of inventory.

5 CONCLUSIONS

Inventory management is an important aspect of managing the production process and the entire logistics chain. This paper presented a mathematical model that allows fast and easy simulations of inventory management based on consumer buying behaviour. For the mathematical model, the probability density function of demand $f_X(x)$ was chosen which, in our opinion [1], best approximates the actual real-life customer buying behaviour. Based on the chosen function $f_X(x)$, the changes in the inventory fluctuation z_0, the storage costs $E[C](z_0)$ and the risk costs β can be calculated in the production process as a function of the changed customer demands.

This paper is a follow-up to a previous study, which presented the negative effects of too high inventory levels of semi-finished products per time unit of observation on the average cost of the ACP product and thus on the final price of the product. This time, we have extended and additionally focused on the risk that may arise when deliberately reducing inventory levels between the work operations of a production process with the aim of approaching the desired lean production process. Logically, reducing the inventory level between work operations increases the risk of interrupting the quantities available to supply the customer and, of course, vice versa. In the practical case under consideration, the proposed model was used to simulate three possible scenarios of a lean production process on an example of inventories, storage costs and risk costs. Only two work operations have been chosen, cold forming and surface protection, as an example, but the model could be extended very easily to the whole logistics chain.

In the present case, there was clearly overproduction and thus waste. Between the two work operations observed, an inventory of as many as 466,666 PC was determined. By simulating three different scenarios, the optimum inventory level was found to be 30,000 PC, at which the inventory costs are minimal with a moderate risk of 17 %. The presented simulation method, based on a mathematical optimisation model, is a simple tool that provides the line management with an efficient decision-making support regarding the quantities to be produced in a given time interval, depending on the customer behaviour. The simulation can also be useful for the sales management to analyse, during the negotiations with customers, what the desired quantities mean for the production costs and to negotiate the selling price accordingly.

The scientific contribution of the presented model and simulation for decision-making support is that by analysing consumer buying behaviour, the changes in the production process can be monitored in terms of inventory costs and the risk that there may be insufficient products available to meet customer needs. There are few useful solutions in the literature for solving these problems, which are every-day

problems in manufacturing. The limitation of the study is that the proposed method is only suitable for batch production.

Our further research will focus on the development of a cost, analysis stream map (CASM) model that will offer a detailed overview of the entire production process in terms of demand, average cost of product ACP and risk. By incorporating CASM, the proposed method will be suitable for the optimisation of lean processes depending on customer behaviour also in industry 4.0. and can be integrated in the ERP or MES companies.

8 REFERENCES

[1] Tanasić, Z., Janjić, G., Soković, M., Kušar, J. (2022). Implementation of the Lean Concept and Simulations in SMEs - a Case Study. *International Journal of Simulation Modelling*, vol. 21, no. 1, p. 77-88, **DOI:10.2507/IJSIMM21-1-589**.

[2] Marc, I., Kušar, J., Berlec, T. (2022). Decision-making techniques of the consumer behaviour optimisation of the product own price. *Applied Sciences*, vol. 12, no. 4, art. 2176, art. ID 2176, **DOI:10.3390/app12042176**.

[3] Seyedan, M., Mafakheri, F. (2020). Predictive big data analytics for supply chain demand forecasting: methods, applications, and research opportunities. *Journal of Big Data*, vol. 7, art. ID 53, **DOI:10.1186/s40537-020-00329-2**.

[4] Uhrin, Á., Moyano-Fuentes, J., Cámara, S.B. (2019). Firm risk and self-reference on past performance as main drivers of lean production implementation. *Journal of Manufacturing Technology Management*, vol. 31, no. 3, p. 458-478, **DOI:10.1108/jmtm-02-2019-0074**.

[5] Petropoulos, F., Wang, X., Disney, S.M. (2019). The inventory performance of forecasting methods: Evidence from the M3 competition data. *International Journal of Forecasting*, vol. 35, no. 1, p. 251-265, **DOI:10.1016/j.ijforecast.2018.01.004**.

[6] Gracanin, D., Buchmeister, B., Lalič, B. (2014). Using cost-time profile for value stream optimization. *Procedia Engineering*, vol. 69, p. 1225-1231, **DOI:10.1016/j.proeng.2014.03.113**.

[7] Nag, B., Pal, R. (2022). Simulation optimization for supply chain decision making. *Winter Simulation Conference*, p. 2853-2863, **DOI:10.1109/wsc57314.2022.10015379**.

[8] El Jaouhari, A., Alhilali, Z., Arif, J., Fellaki, S., Amejwal, M., Azzouz, K. (2022). Demand forecasting application with regression and IoT based inventory management system: A case study of a semiconductor manufacturing company. *Journal of Engineering Research in Africa*, vol. 60, p. 189-210, **DOI:10.4028/p-8ntq24**.

[9] Pusztai, L.P., Nagy, L., Budai, I. (2023). A risk management framework for industry 4.0 environment. *Sustainability*, vol. 15, no. 2, art. ID 1395, **DOI:10.3390/su15021395**.

[10] Perera, H.N., Fahimnia, B., Tokar, T. (2020). Inventory and ordering decisions: a systematic review on research driven through behavioral experiments. *International Journal of Operations & Production Management*, vol. 40, no. 7/8, p. 997-1039, **DOI:10.1108/IJOPM-05-2019-0339**.

[11] Maheshwari, S., Gautam, P., Jaggi, C. K. (2021). Role of big data analytics in supply chain management: current trends and future perspectives. *International Journal of Production Research*, vol. 59, no. 6, p. 1875-1900, **DOI:10.1080/00207543.2020.1793011**.

[12] Amaral, J.V.S.D., Montevechi, J.A.B., Miranda, R. de C., Junior, W.T. de S. (2022). Metamodel-based simulation optimization: A systematic literature review. *Simulation Modelling Practice and Theory*, vol. 114, art. 102403, **DOI:10.1016/j.simpat.2021.102403**.

[13] Jordan, E., Berlec, T., Rihar, L., Kušar, J. (2020). Simulation of cost driven value stream mapping. *International Journal of Simulation Modelling*, vol. 19, no. 3, p. 458-469, **DOI:10.2507/ijsimm19-3-527**.

[14] Orellana, R., Carvajal, R., Escárate, P., Agüero, J. C. (2021). On the uncertainty identification for linear dynamic systems using stochastic embedding approach with Gaussian mixture models. *Sensors*, vol. 21, no. 11, art. ID 3837, **DOI:10.3390/s21113837**.

[15] Wang, C.-N., Nhieu, N.-L., Tran, T.T.T. (2021). Stochastic Chebyshev goal programming mixed integer linear model for sustainable global production planning. *Mathematics*, vol. 9, no. 5, art. ID 483, **DOI:10.3390/math9050483**.

[16] Zhang, X., Prajapati, M., Peden, E. (2011). A stochastic production planning model under uncertain seasonal demand and market growth. *International Journal of Production Research*, vol. 49, no. 7, p. 1957-1975, **DOI:10.1080/00207541003690074**.

[17] Zanjani, M.K., Kadi, D.A., Nourelfath, M. (2013). A stochastic programming approach for sawmill production planning. *International Journal of Mathematics in Operational Research*, vol. 5, no. 1, p. 1-18, **DOI:10.1504/ijmor.2013.050604**.

[18] Afonso, P., Vyas, V., Antunes, A., Silva, S., Bret, B.P.J. (2021). A stochastic approach for product costing in manufacturing processes. *Mathematics*, vol. 9, no. 18, art. 2238, **DOI:10.3390/math9182238**.

[19] Goswami, K. (2020). To buy or not to buy: An analysis of the problematic of consumer behaviour. *International Journal of Management*, vol. 11, no. 10, p. 525-532, **DOI:10.34218/IJM.11.10.2020.050**.

[20] Radhakrishnan, P., Prasad, V.M., Gopalan, M.R. (2009) Genetic algorithm based inventory optimization analysis in supply chain management. *IEEE International Advance Computing Conference*, p. 418-422, **DOI:10.1109/IADCC.2009.4809047**.

[21] Prasertwattana, K., Shimizu, Y., Chiadamrong, N. (2007). Evolutional optimization on material ordering and inventory control of supply chain through incentive scheme. *Journal of Advanced Mechanical Design, Systems, and Manufacturing*, vol. 1, no. 4, p. 562-573, **DOI:10.1299/jamdsm.1.562**.

Strojniški vestnik - Journal of Mechanical Engineering 69(2023)7-8, 326-338
DOI:10.5545/sv-jme.2023.541
Original Scientific Paper
Received for review: 2023-01-31
Received revised form: 2023-03-28
Accepted for publication: 2023-05-15

Finite Element Analysis of Notch Depth and Angle in Notch Shear Cutting of Stainless-Steel Sheet

Kaan Emre Engin*
Adiyaman University, Faculty of Engineering, Turkey

Piercing is a crucial process in the sheet metal forming industry, and the surface quality of the pierced part is an important parameter that defines the overall quality of the product. However, obtaining a good surface quality is a challenging task that depends on the effect of several process parameters and necessitates the use of non-conventional procedures. Notch shear cutting is a relatively new progressive approach in which the workpiece is indented with a notch form with a predefined notch angle and depth, and then the indented workpiece is subjected to conventional piercing. In this study, conventional piercing and notch shear cutting processes were experimentally performed on 1.4301 stainless steel sheet of 2 mm thickness. Then, finite element (FE) analyses were conducted utilizing Deform-2D software. After ensuring that the experimental and simulation works were consistent with each other, the FE analysis of notch shear cutting was carried out for three distinct notch depths (15 %, 30 %, and 60 % of the workpiece thickness) and six different notch angles (10°, 20°, 30°, 40°, 50°, and 60°). Investigations were performed on shear zone length distributions, which are direct indications of the surface quality on sheared workpieces, crack propagation angles, and required cutting loads. The best surface quality was obtained when the notch angle was set to 50° and the notch depth was set to 15 % of the workpiece thickness. It was also observed that notch angle and notch depth had a certain level of influence on required cutting load.

Keywords: metal cutting, notch cutting, piercing, surface quality

Highlights

- *The primary objective of the study was to determine the influence of notch angle and notch depth on surface quality and required cutting in notch shear cutting of 1.4301 sheets of 2 mm thickness.*
- *Both experimental and finite element (FE) analyses were performed to validate the consistency of two methods. Deform-2D software was utilized for numerical analysis whereas a die set was manufactured for experimental work.*
- *The overall best quality which surpassed the surface quality of piercing was achieved with a notch angle of 50° and a notch depth of 15 % of the workpiece thickness.*
- *It was determined that when the notch angle increased, the required cutting load decreased. This was also true for increasing notch depth, but the load incurred during the generation of notch depth must be included in the total energy consumption.*

0 INTRODUCTION

Piercing is a fundamental process in the sheet metal forming industry and is defined as the cutting of the sheet metal from the stock with a die set consisting of a predefined shaped punch and a lower die. The primary purpose of the piercing process is to avoid workpiece rework and maintain good surface quality. Burrs and protruding surfaces create an impediment to achieving this goal. Burrs can cause early tool wear, reduced corrosion resistance and because of their sharp formations, can become the primary source of accidents. These negative impacts result in poor overall process production quality.

To remove these formations from the surface, conventional grinding and other cleaning procedures are necessary, resulting in additional labour hours, higher costs, and specific people being withdrawn from the main operating cycle and allocated solely to these deburring and cleaning activities **[1]**.

Due to the nature of the process, numerous parameters should be adjusted and understanding the effect of these parameters is the key step to achieving good cutting results and lower energy consumption. Adjustments in clearance **[2]** and **[3]**, cutting speed **[4]**, workpiece and tool material **[5]**, tip form **[6]**, tool coatings **[7]** and wear characteristics **[8]** to **[12]** have significant effects on both surface quality and energy aspects in conventional piercing procedures.

However, a relatively recent procedure known as "notch shear cutting" has been developed with the goal of improving the surface quality of sheared sheet components. A notch with specified characteristics is pushed onto the workpiece in this progressive method. The operation then proceeds with the conventional piercing method.

Few studies have investigated the notch shear cutting of sheets and related parameters. Studies investigating different aspects of the notch shear cutting proved that good surface quality with reduced burr formations can be achieved by using this method.

Sachnik et al. **[13]** used workpieces DC04, 1.4301, ENAW-6014 and CuSn6 with 1 mm thickness and performed both closed and open cuts with a

*Corr. Author's Address: Adiyaman University, Faculty of Engineering, Altinsehir Mah. 3005. Sok. No:13, Adiyaman, Turkey, kengin@adiyaman.edu.tr

special progressive die. They mainly investigated the formation of burrs and how they change according to the notch placement on the workpiece. Both simulation and experimental works had been accomplished. The investigations were done for different values of notch cutting parameters as notch depth (30 % to 60 % of the sheet metal thickness), notch's radius (0.05 mm, 0.125 mm, and 0.2 mm) and clearance (6 %, 8 %, and 10 % of the material thickness). They showed that the burr formation is directly linked with the position of the notch and notch height. They also stated that around 40 % notch heights gave the most burr-free surfaces.

Krinninger et al. [14] investigated the effect of notch parameters on the workpiece by using both experimental and finite element method (FEM) for sheet materials made of aluminium alloys ENAW-5754 and ENAW-6014 with a thickness of 1.0 mm. The clearance between the die and punch was 3 % of the workpiece thickness. They designed a progressive die set to perform the experimental work. Notches were both applied from the topsides and downsides of the workpiece; 25 % and 40 % of the notch depths and a fixed value of 60º as the notch angle were applied on the workpieces. They discovered that while the topside notch could lower the required cutting forces, in general, there was no reduction in cutting forces when the percentage drop in sheet thickness was considered. With downside notches, they observed that a surface distribution without burr could be achieved.

Feistle et al. [15] performed notch shear cutting studies on press-hardened components (PHC) made of aluminium-silicon-coated manganese-boron steel (22MnB5) sheets at room temperature. The shearing of PHC steels at room temperature causes difficulties due to their higher mechanical properties. Moreover, the wearing of tools progresses rapidly, which contributes to the formation of more burrs at the edges of the workpieces. The workpieces had 1.5 mm thickness. The die clearance was 15 % of the workpiece thickness. The notch angle was 60º. Notch depths were 16 % and 40 % of the workpiece thickness. Three notch variables (without notch, topside notch, and downside notch) were examined by both FEM and experimental methods. They measured the zone distributions on the sheared surfaces and calculated the required shearing force. They stated that cutting loads were reduced for notched specimens and provided improved surface quality free of burrs.

The existence of a notch on the workpiece introduces additional parameters to be investigated. The mentioned studies investigated some values of notch depth, but the notch angle values were generally limited to 60º. Furthermore, none of the studies investigated the effect of these parameters on stainless steels which are one of the most used materials in industrial applications. The surface quality and required cutting load change according to notch depth and notch angle for stainless steels should be investigated with varied values of these two parameters. If correct parameter adjustments can be established for 1.4301 sheets during notch shear cutting and high surface quality can be produced, then a technical advantage can be acquired over conventional piercing techniques.

To achieve this, experimental and computational validations for conventional piercing and notch shear cutting were conducted initially. Following the consistency of the findings between experimental and computational work, three different notch depths (15 %, 30 % and 60 % of the workpiece thickness) and six different notch angles (10º, 20º, 30º, 40º, 50º, and 60º) were employed to execute the notch shear cutting of 1.4301 stainless steel sheet; the influence of these variables on the surface quality and required cutting load were investigated using finite element analysis.

1 PROCESS PARAMETERS

1.1 Notch Depth, Notch Angle, and Surface Distribution on the Workpiece

As an addition to the parameters of conventional piercing, notch shear cutting introduces new parameters such as notch depth, which is the percentage of the height of the notch to the thickness of the workpiece; notch angle, which is the angle value of the notch indented on the surface of the workpiece; and notch radius, which is the radius given to the tip of the notch.

Notch shear cutting is a progressive process. The related illustration of the steps of the process was given in Fig. 1. First, a notch indenter with a predetermined angle, depth, position, and radius is manufactured (Fig. 1a). In the second step, the indenter is forced against the workpiece, resulting in the development of a notch (Fig. 1b). Then, in the last step, the notched workpiece is subjected to conventional piercing and the process is completed (Fig. 1c).

Shearing of the material is a complicated phenomenon. When a workpiece is pierced, it goes through a series of stages before being entirely ruptured. Zones typical of piercing are generated on the workpiece's surface during these stages. Rollover (die roll) zone, shear (burnished) zone, fracture zone, and burr formation are the four zones mentioned. By measuring these zones and observing how much

they dominate the overall surface length, the surface quality of the sheared workpiece can be assessed.

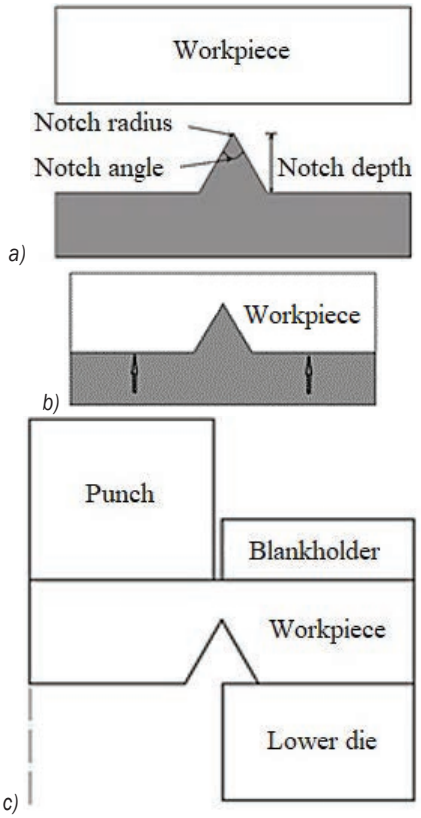

Fig. 1. *The illustration of the steps of notch shear cutting and related components; a) manufactured indenter with predetermined notch properties, b) formation of notch on the workpiece and, c) conventional piercing of the notched workpiece*

Rollover and burrs are the least desired zones on the surface, and investigations often involve methods and parameter modifications for eliminating these zones. Stahl et al. **[16]** implemented two-stage shear cutting instead of one-stage shear cutting of truck frame parts and revealed the effects of different process parameters on the improvement of surface quality and burr formations along with fatigue enhancement of the sheared parts. Mucha and Tutak **[17]** studied the impact of clearance on the burr size formed on a thin steel sheet with a 55 HRC hardness during the blanking of angled hooks, as well as the wear characteristics of the punch. Nishad et al. **[18]** collected and compared the methodologies used to improve the process and elaborated on how the parameters of the process impact the result. A long shear zone length is the most desired situation.

The illustration of these zones was given in Fig. 2. Denting the surface with a notch before piercing has the potential to reduce burr forms while extending the shear zone length.

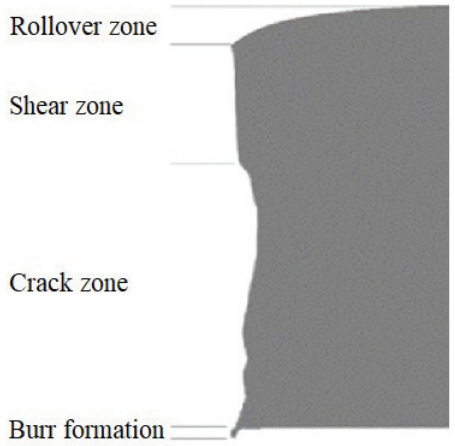

Fig. 2. *Zone distributions on the sheared surface*

Notch angle and depth are essential parameters that can influence crack propagation and orientation as well as zone distributions.

Determining the optimal values of these parameters are important. The upper limit of the notch angle value was set using a fine-blanking approach.

Generally, a notch is produced on the workpiece prior to cutting using a v-ring indenter to keep the workpiece in place and the side angle of the v-ring indenter is normally kept constant as 60º in related procedures like fine blanking. From this point of view, the upper limit of the notch angle was set at 60º; moreover, 10º, 20º, 30º, 40º, and 50º were added to observe how they influenced the results. From low to high, notch depths were set at 15 %, 30 %, and 60 % of the workpiece thickness, respectively.

2 EXPERIMENTAL METHODOLOGY

The first step in the study was to conduct the experiments. Although this study relied heavily on finite element (FE) analysis, computational results should be cross-checked with experimental data. If computational and experimental work for piercing and notch shear cutting could be verified to be consistent with one another, the simulation work would be expanded to study the influence of other notch shear cutting parameters.

The stock material was 1.4301 stainless steel sheet. The mechanical characteristics of the material have crucial importance in shear-cutting processes. Due to this situation, the mechanical characteristics of 1.4301 sheet were determined as the beginning phase of the research. If the mechanical characteristics

of the workpiece material were defined with errors in the software, the results would almost certainly differ from those obtained via experimental work. 1.4301 stainless steel sheet is used in a variety of industrial applications, including mining, maritime and structural applications as well as the manufacture of bolts, screws, and containers [19].

Tensile tests were used to get the stress-strain graphs that the software required. A stock 1.4301 stainless steel sheet was supplied from local sheet metal vendors. The dimensions of the stock material were 2000 mm × 1000 mm with 2 mm thickness to satisfy the tensile testing standards. The chemical composition and the mechanical properties of the material according to the manufacturer's sheets are given in Tables 1 and 2.

Table 1. *Chemical composition of 1.4301 sheet*

Composition	Weight [%]	Composition	Weight [%]
C	0.08	Si	0.75
Mn	2.0	S	0.03
P	0.04	Ni	9.0
Cr	19.0		

Table 2. *Mechanical Properties of 1.4301 sheet*

Properties	Value	Properties	Value
Tensile strength	515 MPa	Elongation at break	60 %
Yield strength	210 MPa	Hardness (Rockwell B)	80

Using a water jet, the specimens were cut out of the stock according to ASTM E8 standards, considering the rolling directions (0º, 45º, 90º). The goal of using a water jet is to lessen the thermal effects that arise on the material's surface. The sides of the specimens were also polished to prevent the notch effect from occurring during tensile tests. Fig. 3 shows the dimensions of the test specimen (Fig. 3a) and the actual test specimen (Fig. 3b).

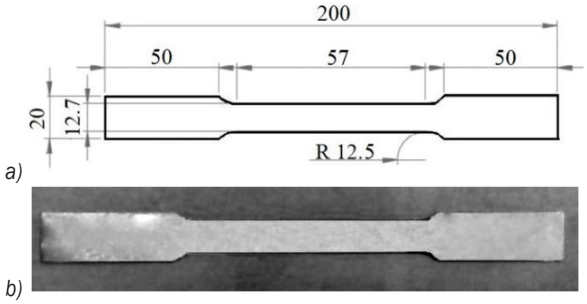

Fig. 3. *a) Dimensions, and b) the actual image of one of the tensile test specimens*

Fig. 4 depicts the metallographic structure of 1.4301 sheet observed by using a scanning electron microscope (Zeiss Gemini SEM 500). A Shimadzu AG-X Plus tensile testing machine was used to measure the engineering curve of 1.4301 sheet.

To reduce the margin of error, the tensile tests were repeated six times at room temperature for each rolling direction at a strain rate of 0.05 s^{-1}.

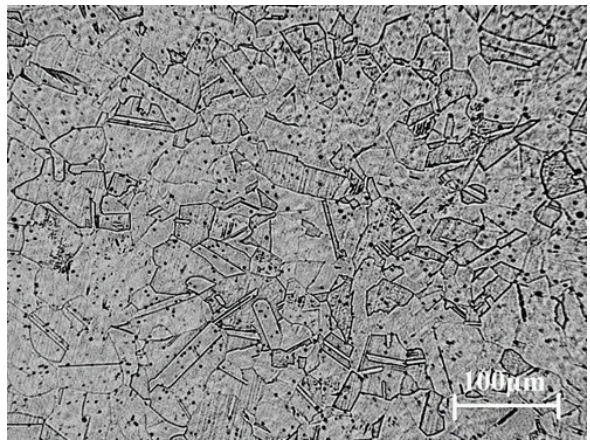

Fig. 4. *Metallographic structure of 1.4301 stainless steel sheet*

First, engineering stress was measured, and then true stress is obtained by using true stress-strain equations expressed in Eqs. (1) and (2) as:

$$\sigma_t = \sigma(1+\varepsilon), \tag{1}$$

$$\varepsilon_t = ln(1+\varepsilon), \tag{2}$$

where σ_t and σ represent true and engineering stresses, ε_t and ε are true and engineering strains. The obtained engineering and true stress-strain curve of 1.4301 sheet were given in Fig. 5.

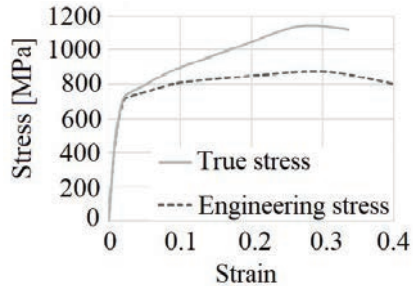

Fig. 5. *True and engineering stress-strain diagram of 1.4301 stainless steel sheet*

In the second phase, both piercing and notch shear-cutting operations were carried out experimentally. A manufactured die set was used to perform piercing and notch shear cutting. It consisted of six parts: the

punch, upper die block, guides, a fixed-type blank holder, lower die, and lower die block. The blank holder and die blocks were constructed of S235JR, while the remainder of the components were made of heat-treated 1.7225 steel. The die set (Fig. 6a) and its exploded view (Fig. 6b) are shown.

Due to the progressive nature of notch shear cutting, which necessitates the formation of a notch on the workpiece's surface before conventional piercing can begin, a special hollow punch was produced to be used as an indenter. The manufactured hollow punch's tip sides had a 60º notch angle and a notch tip radius of 0.5 mm. The depth of the hollow was adjusted to 1.2 ± 0.1 mm to prevent the hollow punch to penetrate further than the notch depth of 60% of the workpiece thickness. The total length of the punch was 80 mm. Fig.7 shows the illustration of the hollow punch (Fig. 7a) and the formation of the notch indenter (Fig. 7b).

Clearance between the die and the punch was calculated according to Eq. (3) as:

$$C = 100((D_m - D_p)/2t)\ [\%]\ , \qquad (3)$$

where D_m is the lower die diameter, D_p is the punch diameter and t is the workpiece thickness.

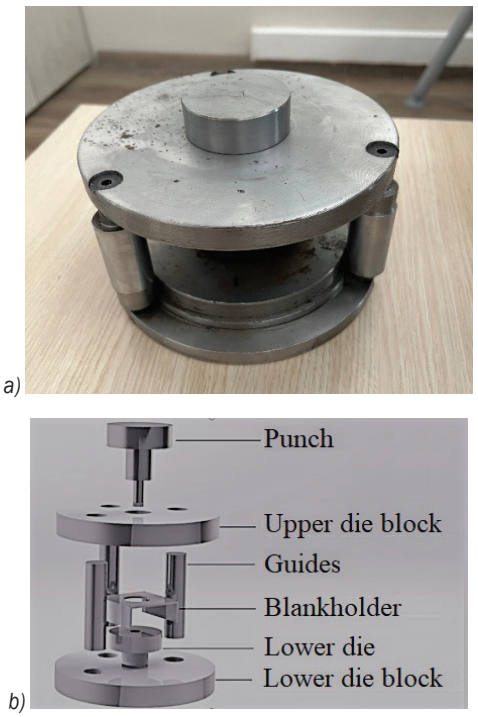

Fig. 6. *a) The die set, and b) it's exploded view*

The die clearance was fixed at 5 % of the thickness of 1.4301 sheet, which was 2 mm, for both experimental and computational work.

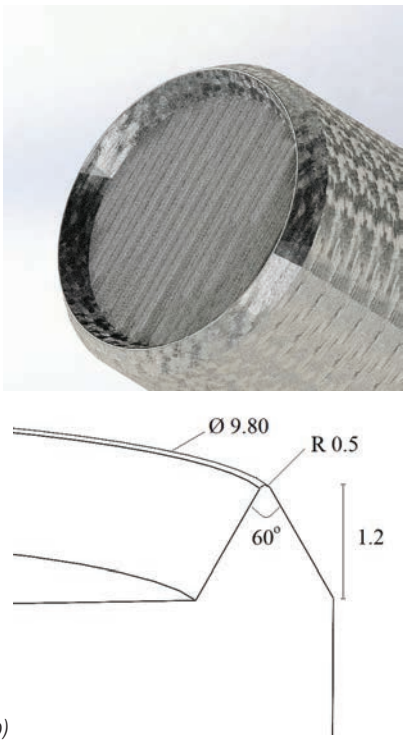

Fig. 7. *a) Illustration and b) dimensions of hollow punch in [mm]*

The lower die diameter was 10 mm; based on Eq. (3), the calculated and fabricated punch diameter to perform a conventional piercing process was 9.80 mm. The total length of the punch was 80 mm. Experiments were conducted utilizing a hydraulic press with a capacity of 300 kN and under a ram speed of 1 mm/s. To keep the punches in place, a punch holder was manufactured and attached to the press's ram.

Fig. 8. *a) Notch indentations on the workpiece, and b) conventionally pierced workpiece*

The piercing operation was carried out using the manufactured die set while the notch shear-cutting process was carried out in a progressive manner. The notch is first produced on the downside of the workpiece. Following that, the standard piercing process was performed. Fig. 8 shows an example of notch creation on the workpiece surface (Fig. 8a) and one of the typically pierced workpieces (Fig. 8b), respectively.

3 NUMERICAL SIMULATION AND MODEL VERIFICATION

Deform-2D software was used to execute the computational work. Sheet metal shearing is one of the many forming techniques that the software can model. The software employs axisymmetric modelling which implies that only half of the setup is required to run it. The workpiece was modelled as a plastic object, whereas the punch, lower die and blank holder were defined as rigid bodies. Shear friction occurs when the workpiece deforms and is a function of the yield stress. The friction between the workpiece and the shearing tools was assumed to remain constant and was calculated as follows in Eq. (4):

$$fs = mk\,, \tag{4}$$

where f_S is the frictional stress, k the shear yield stress, and m the friction factor. According to the software's database, shear friction was given a value of 0.12.

Large plastic stresses are generated over a narrow zone between the punch and the die during shearing. At that small deformation zone, the material was considered to be isotropic and yielding followed Holloman's equation which was stated in Eq. (5) as:

$$\bar{\sigma} = K\varepsilon^{-n}, \tag{5}$$

where $\bar{\sigma}$ is the effective stress, ε the effective strain, K is the material constant, and n the strain hardening exponent [20].

Deform-2D database includes the material properties for 1.4301 stainless steel. Fig. 9 demonstrated the consistency of the flow stress-strain curve of 1.4301 stainless steel in Deform-2D's database and the computed flow stress-strain curve obtained from the tensile tests by using Holloman's equation.

Fracture initiation in a piercing process usually begins at the punch's or lower die's contacting edge. For computational studies, the fraction criterion is critical because good criterion choice brings the outcome values closer to the experimental results.

For the purposes of numerical analyses, the normalized Cockroft and Latham fracture criterion were utilized.

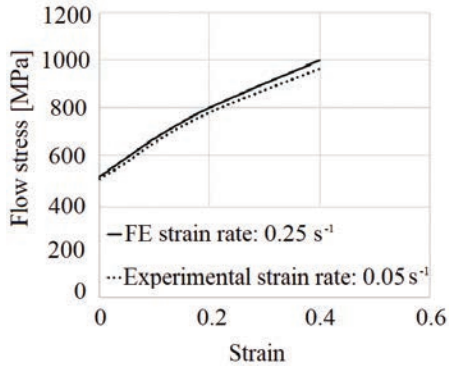

Fig. 9. *Flow stress-strain curve of 1.4301 stainless steel*

The criterion indicates that when effective strain equals the critical value (C), fracture initiation begins at the point where the value is reached. The criterion was given in Eq. (6) as:

$$\int_0^{\bar{\varepsilon}^f} \left(\frac{\sigma^*}{\bar{\sigma}} \right) d\bar{\varepsilon} = C, \tag{6}$$

where σ^* is the maximum principal stress, ε^f the fracture strain, C the critical value (damage factor), and $\bar{\sigma}$ and $\bar{\varepsilon}$ are the expressions of effective stress and effective strain.

To simplify the criterion, the ratio between maximum principal and effective stress was assumed to be constant at the shearing zone. This assumption resulted in $\varepsilon^f = C$ meaning that crack initiation starts at the point where effective strain and critical values become equal [21].

The critical value, C, can be evaluated by a tensile test regardless of the working operation. The critical value of 1.4301 sheet was defined as 0.54, which was acquired from the conducted tensile test.

The software employs a step-based iteration mechanism; at each step, it verifies the workpiece's values. If the values described by mesh formations on the workpiece approach the critical value, element deletion is applied to the associated meshes to view the fracture initiation and propagation. This function is governed by two parameters: "fracture steps" and "fracture elements." The value of fracture steps sets the step interval at which the simulation pauses and element deletion is performed. This value was selected as 1, the minimal value. This signifies that element deformation is considered at each step. Fracture elements are the number of elements that must exceed

the critical damage value for the simulation to halt and delete elements. This value was set as the system default to 4. Automated mesh generation was used and defined to be executed for every 0.02 mm progression of the top die to provide optimum re-meshing.

Element deletion improves visualization coherence with experimental outcomes. However, negative aspects of this approach include volume deterioration and excessive mesh deletion if mesh element numbers are maintained low. Low mesh numbers result in an imprecise representation of the shear region where the zones interweave. This circumstance results in inaccurate calculations of the cutting load and interpretations of the zone lengths derived from simulation results.

The density of the meshes at the shear zone must be as dense, small, and numerous as possible to prevent volume loss and accurate propagation of the fracture, which enables consistent visualization of the variation in zone distribution. Initially, the meshes on the workpiece were evaluated with varying element counts; however, as the element count reached 8,100, isoparametric quadratic elements, it was determined that there was no change in cutting load above this element count. Tough, to obtain optimum surface distribution on the sheared workpieces, 10,000 isoparametric quadratic elements which are the maximum number of elements that can be defined in Deform-2D and 9,786 number of nodes with 0.03 mm element size were used. The simulation parameters were given in Table 3.

Table 3. *Simulation parameters*

Parameter	Value
No. of elements	10,000
No. of Nodes	9,786
Element size	0.03 mm
Fracture steps	1
No. of fracture elements	4
Remesh criteria	Every 0.02 mm of the punch penetration

In addition, mesh elements were stacked as closely as possible with the use of mesh windows to raise the total number of elements in the shearing zone.

For both piercing and notch shear cutting processes, the distribution of zones and the cutting load values were estimated after conducting both computational and experimental work.

The numerical analysis phase of the notch shear-cutting process required two sequential steps to duplicate experimental conditions for the most accurate results. Fig. 10 shows the steps applied during the computational work of notch shear cutting. First, it was necessary to push the predefined notch indenter into the workpiece (Fig. 10a) and produce the indentation (Fig. 10b). The notched workpiece was then placed in a typical piercing setup (Fig. 10c) and the following steps were carried out (Fig. 10d).

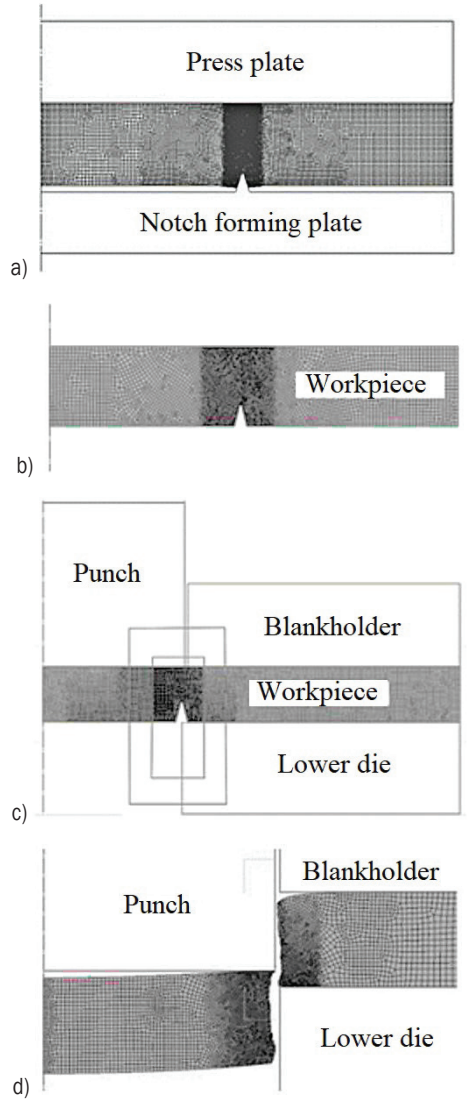

Fig. 10. *The steps of simulation process; a) formation of notch at the downside of the workpiece, b) notched workpiece, c) conventional piercing, and d) completion of the process*

3.1 Ideal Crack Condition

During a shearing operation, the fracture of the material begins at the corners of the punch and die that are in contact. The creation of a fracture propagates rapidly, resulting in the separation of

material at the intersection with the opposite corner. The ideal crack (Φ) occurs when the required angle of crack propagation (θ) is directed toward the punch and die cutting edges. In many instances, however, the real propagation (β) of a fracture does not follow this anticipated pattern, resulting in secondary cracks that cause surface flaws on the workpiece. When the angle values of β and θ are closest, the optimal cutting condition may be attained.

This situation can be expressed in Eq. (7) as:

$$\Phi = \beta - \theta \cong 0 \,. \tag{7}$$

The ideal crack propagation angle can be expressed in Eq. (8) as:

$$\theta = \text{Arctan}\left(\frac{c}{t - u_p}\right), \tag{8}$$

where C is the clearance, t the sheet metal (workpiece) thickness, and u_p the punch penetration corresponding to the first crack initiation within the sheet. The directions of angle β and angle θ were illustrated in Fig. 11.

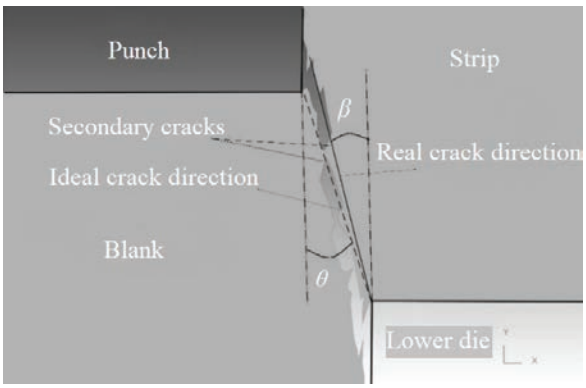

Fig. 11. *Illustration of Ideal crack propagation angle (θ) and real crack propagation angle (β)*

4 RESULTS AND DISCUSSION

Both experimental and numerical work were performed under the clearance value of 5 % of the workpiece thickness which was 2 mm, with a 10 mm lower die diameter and 9.80 mm punch diameter for conventional piercing with a punch speed of 1 mm/s.

Throughout the notch formation sequence, the hollow punch with a 60º notch angle, a notch tip radius of 0.5 mm, and a notch depth of 60 % of the workpiece thickness (1.2±0.1 mm) was utilized. During the second phase (piercing after notch generation) of notch shear cutting, the same settings as with conventional piercing were employed.

Fig. 12 depicts a comparison of the change in cutting load between simulation and experimental tests.

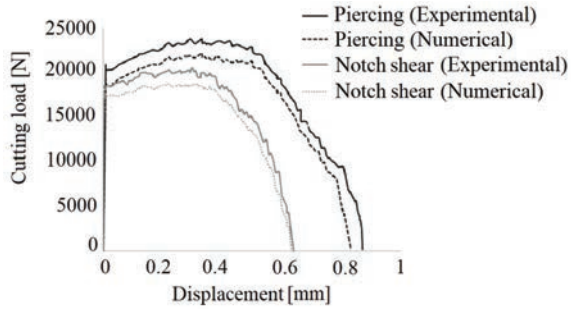

Fig. 12. *Comparison of required cutting load between computational and experimental work*

The experimental and numerical findings were within 5 % range of each other on average. This was the outcome of the experimental environment's external influences such as dust, additional friction between tools and load cell accuracy. The rest of the research was carried out with computational work once the measurements were verified to be identical.

Figs. 13 and 14 compare the zone distribution for conventional piercing and notch shear cutting, respectively.

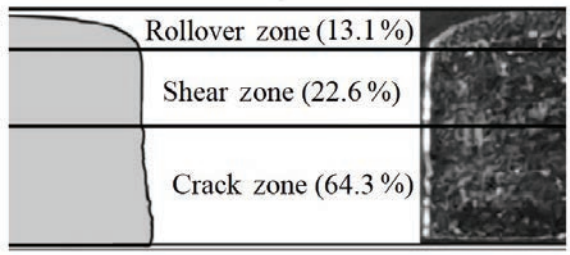

Fig. 13. *Comparison of zone distributions between computational and experimental work (Piercing)*

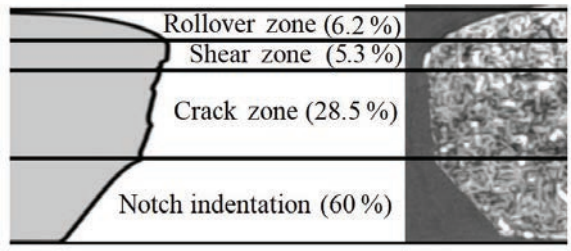

Fig. 14. *Comparison of zone distributions between computational and experimental work (Notch shear cutting)*

The computational work was completed by following the outlined sequential stages to replicate the experimental work. First, three values of notch depth

(15 %, 30 % and 60 % of the material thickness) and 6 different notch angles (10º, 20º, 30º, 40º, 50º, and 60º) with 0.5 mm notch tips were virtually penetrated to the downside of 1.4301 sheet with 2 mm thickness. After the material was notched, the piercing stage of the process was simulated using the configuration in which the lower die diameter was 10 mm, the punch speed was 1 mm/s, and the clearance was 5 % of the material thickness. As in the experimental study, the punch diameter was 9.80 mm, no radiuses were specified at the punch's edges, and the tip of the notch was aligned with the punch's cutting edge at shearing in every simulation.

Required cutting loads to shear the workpiece, fracture propagation angles and zone distributions were investigated. In cutting operations, cutting load is an important parameter that specifies the required loading capacity of the press and plays a crucial role in overall energy usage. It was discovered that the cutting loads necessary to shear notched materials were less than the load value for the piercing operation (28.5 kN). The deeper the notch penetrated into the material; the less cutting force was required at the sequential piercing step. This outcome was anticipated due to the reduction in material thickness following the creation of a notch in the workpiece. A 15 % notch depth resulted in the highest whereas 60 % notch depth resulted in the lowest required cutting load for each notch angle. For example, when the notch angle was fixed to 60º, the required cutting loads were obtained 22.2 kN for 15 % notch depth, 16.6 kN for 30 % notch depth, 11.8 kN for 60 % notch depth, respectively. The effect of the notch depth on the required cutting load is unique to notch shear cutting, regardless of the workpiece shape, and is consistent with the literature [22]. Another observation was made on the effect of notch angles. Apart from the notch depth, the required cutting load decreases with increasing notch angle due to the decrease in the cross-sectional area of the workpiece between the punch and die. The changes in required cutting load according to notch depths and angles are given in Fig. 15.

Although it might be thought that a deeper notch has the advantage of a lower cutting load, it is important to remember that two phases are necessary to complete the entire notch shear-cutting process. If load comparisons were conducted exclusively for the shearing portion of the operation, it might be argued that a notch could reduce the cutting load.

To account for each phase of the operation, however, 15 kN should be added to the total load values which was the average of the loads required to form the notch into the surface of 1.4301 sheet for each of the depths listed.

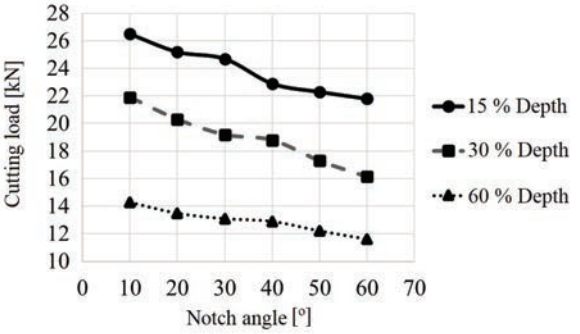

Fig. 15. *Cutting load change according to notch angle and notch depth*

Fig. 16 illustrated the disparities between the ideal angle (θ) of crack propagation and the real angle (β) of crack propagation.

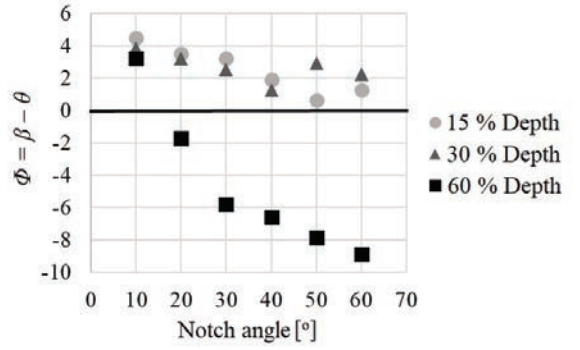

Fig. 16. *The difference between real crack propagation angle (β) and ideal crack propagation angle (θ)*

The best surface quality can be achieved when the difference between these two angles is closest to zero.

The distribution of zones and the propagation of cracks are interrelated; therefore, an improper crack propagation difference will lead to secondary cracks and protruding surfaces.

Deform-2D can measure distances on the sheared workpiece in relation to zone distributions, and the character of the cut (smooth or protruded) can be clearly visualized and estimated by using the software's post-processor section once the simulation is complete. Fig. 17 shows the shear zone percentage change according to notch depth and notch angle.

A comparison of Figs. 15 and 16 demonstrated that the difference between crack propagation angles and shear zone percentages were in correlation. For piercing processes, the optimal zone distribution

(best surface quality) occurs when the rollover and crack zone lengths are minimal and free of burr formation while the shear zone length is maximal; 15 % of the notch depth with 10º, 20º, and 30º notch angles resulted in burr formation, which was the least desirable outcome. The development of protrusions reduced as the notch angle increased, and at 50º the longest shear zone length and the shortest crack zone with almost no protrusions were reached.

From Fig. 16, it was observed that the closest values to zero amongst all notch depths and all notch angles were achieved when notch angle value was selected as 50º and the notch depth value was selected as 15 % of the workpiece thickness. Fig. 17 confirmed this result, the shear zone percentage, 24.56 %, was also the highest at these values.

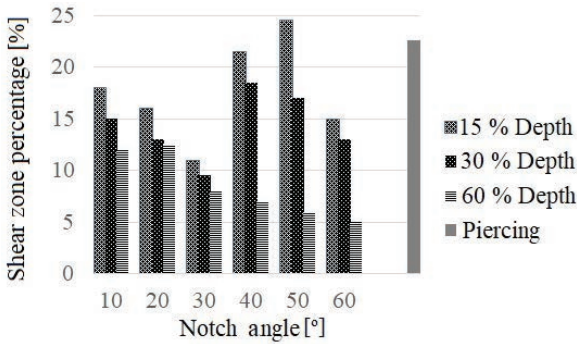

Fig. 17. *Shear zone percentage change according to notch depth and notch angle*

The shear zone length of the specimen measured after piercing (22.6 %) could only be surpassed by using these values. This situation showed that a technical advantage can be obtained over conventional piercing with proper adjustments. The relationship between crack propagation angles and shear zone percentages was in accordance with previous studies. Using the angles of crack propagation, Hambli et al. **[23]** devised an algorithm for predicting optimal clearance. They established a tolerance convergence percentage of 1 % and stated that an optimal clearance could be reached when the difference between crack angles satisfied this value, indicating that no secondary cracks occurred, and good surface quality was acquired. Engin and Eyercioglu **[24]** and **[25]** studied the influence of different process parameters on 1.4301 stainless steel sheets with different thicknesses and diameters. They observed that the best surface quality on the sheared workpieces was achieved when the difference between crack propagation angles was minimal. Fig. 18 displays the surfaces of sheared workpieces in relation to the notch depth, notch angle, and independently for piercing, as established by the Deform-2D software.

A further observation was made on another impact of notch depth. It was determined that the length of the shear zone dropped dramatically when the notch depth increased, independent of the notch angle. This is due to the workpiece's pre-deformation during notch formation.

When the workpiece was subjected to the conventional piercing phase, which was the second step of the process, shear and fracture zones were generated following the top portion of the notch.

In the case of deeper notches, there remained a reduced region for shear zones to develop, and this was the main reason for the drop in shear zone length. Figs. 17 and 18 demonstrated that the crack zone dominated the surface and the shear zone decreased below 7 % for notch angles between 40º and 60º and for 60 % notch depth. This case revealed that even though pre-deformation (notch) on the workpiece appeared to make the shearing region less affected during piercing, deeper notches were not a guarantee of high surface quality and notch angles should be taken into consideration.

Regardless of notch depth, notch angles determined the crack propagation course and, in turn, affected the shear zone length. It was clearly understood that the obtained results depended on the combined effect of notch angle and notch depth values. For every notch depth value, the notch angle difference altered the crack propagation. As indicated before, for 15 % notch depth, lower notch angle values resulted in burr formation. When notch angle values increased, burr formations started to reduce up to a limit where the best surface quality could be obtained. In the event of higher notch depths, such as 30 %, the shear zone lengths decreased incrementally from 15 % to 10 % between 10º and 30º notch angles but reached their peak at a 40º notch angle with a length value of 22.43 %, and then started to decrease again.

This situation showed that for every value of notch depth, there exists a notch value at which the shear zone length could reach its peak height.

This criterion was met with a 50º notch angle at 15 % notch depth, a 40º notch angle at a 30 % notch depth, a 20º notch angle at a 60 % notch depth for 1.4301 sheet, respectively.

However, it should be clearly stated that the general form of the sheared surfaces is also an important parameter. As mentioned before, the primary objective was to obtain the best possible surface quality to transcend conventional piercing. For deeper penetrations such as 30 % and particularly

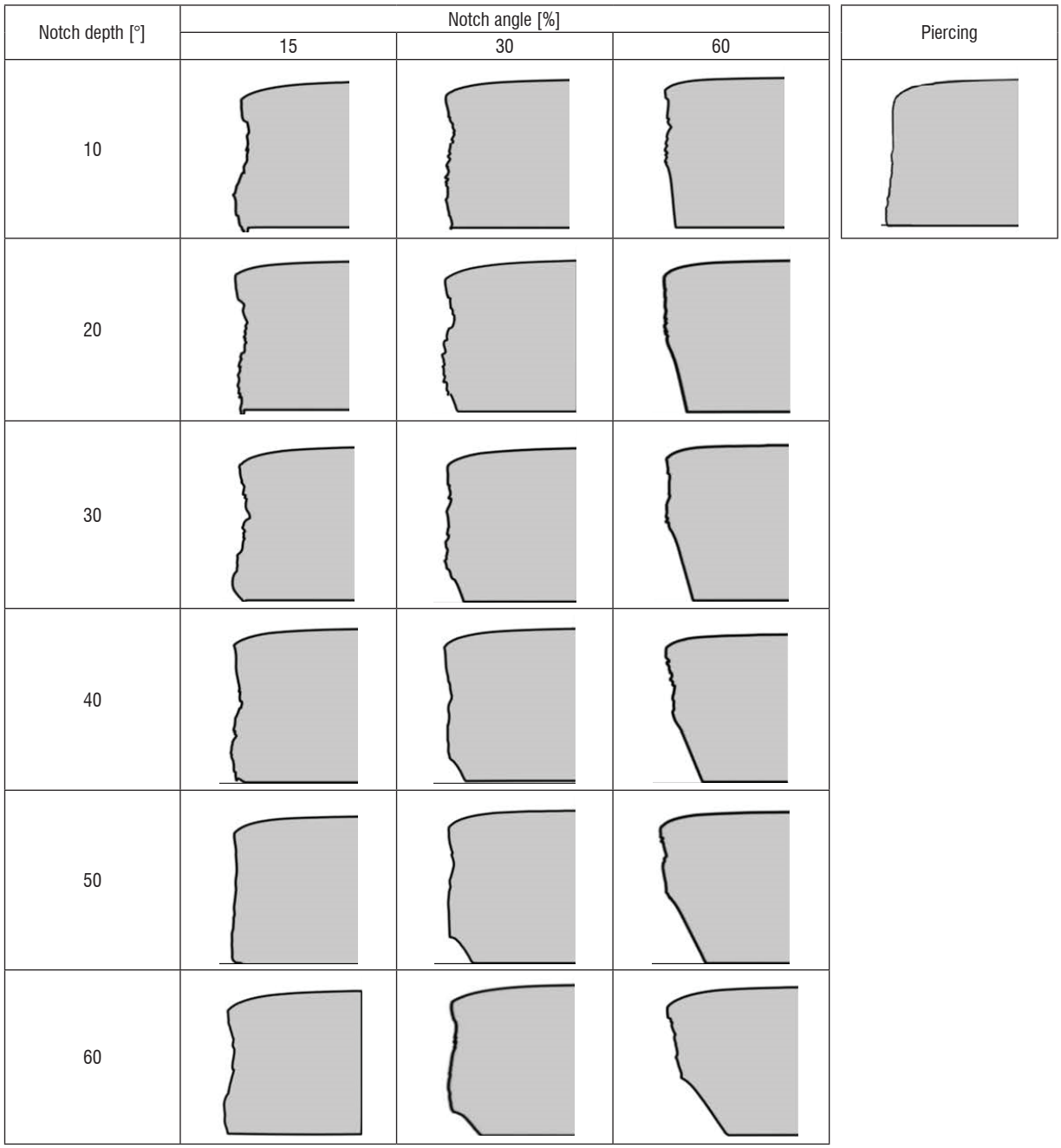

Fig. 18. *Visual representation of sheared parts as a function of notch depth and notch angle generated by the Deform-2D software*

60 % notch depths, the increase in the notch angle resulted in the reduction of burr formation; however, the form of the workpiece gradually deteriorated and took a conical shape at the downside. This circumstance is equally undesirable. At high values of notch depth, it must be considered that the use of wider notch angles may result in the deformation of the sheared material's shape.

Typically, the outputs of piercing/ shearing processes are restricted to the parameters applied specifically for that workpiece material. The same situation applies to this research. In terms of zone distributions, a 50º notch angle and 15 % notch depth outperformed the shear zone length value of conventional piercing to produce the greatest surface quality and form. However, it is limited to

1.4301 sheets if and only if these conditions are satisfied. Any change in the notch forming position, clearance, punch/die diameters, shearing speed and, most importantly, the workpiece material modifies every effect and may result in varied outputs. Due to the interdependent interactions between regulating parameters, it is difficult to establish an optimal setting for shearing and cutting operations that accounts for all process variables and workpiece materials.

5 CONCLUSIONS

The main aim of this study was to determine the effect of notch angle and notch depth on the surface distribution and required cutting force during notch shear cutting of 1.4301 stainless steel sheet workpieces to fill a gap in the literature due to an absence of research on notch shear cutting of commonly used stainless steels. Compared to piercing, notched shear cutting is a relatively novel method for cutting metal sheets. Conventional piercing and notch shear cutting were carried out to compare the results to those obtained from simulations. The remainder of the study is then completed virtually. Using Deform-2D software, a FEM study of notch shear cutting was performed for three different notch depths (15 %, 30 %, and 60 % of the workpiece thickness) and six different notch angles (10º, 20º, 30º, 40º, 50º, and 60º). The results obtained in this study are summarized below.

- For specimens with deeper notches and wider notch angles, the required cutting load was observed to decrease. In addition, cutting specimens with notches required less load than conventional piercing. This is a direct by-product of the material's decreased thickness due to the notch formation on the workpiece. Due to the progressive nature of the operation, the load applied during notch formation must be added to the total value of the required cutting load, resulting in an increase in total energy consumption. In addition, it may take longer to complete the whole process than piercing, which is not a progressive operation like notch shear cutting.
- There was an ideal value for each notch depth and notch angle at which the sheared surface was as good as possible in comparison to the other values for these two parameters. This condition was achieved at a 50º notch angle for a 15 % notch depth, at a 40º notch angle for a 30 % notch depth, and at a 20º notch depth for 60 % notch angles, respectively. In contrast to the ideal values, however, values that depart from them might lead to increased surface flaws. In addition, the specimen's base became conical due to the increasing notch depths and notch angles (such as 60 % notch depth and 60º notch angle) which is undesirable. The shear zone length of the specimen estimated after piercing (22.6 %) could only be exceeded by notch shear cutting with a 50º notch angle and 15% notch depth (24.4 %). The remaining shear zone values were inadequate for shearing 1.4301 sheets when compared to conventional piercing.
- If surface quality is of the highest significance and no rework of the produced workpieces is necessary during the production, notch shear cutting can produce better results than piercing, particularly in preventing burr forms. However, to attain the maximum shear zone length with no burrs, preliminary work should be conducted prior to application, since any uncorrected value may cause the shear zone to be shorter than piercing. Hence, obtaining the optimal settings is a complex and expensive operation to be accomplished through experimental trial and error, FEM simulations are required to conduct the work. Nonetheless, it is a time-consuming endeavour. Notch shear cutting seems feasible when utilized for mass manufacturing.
- All findings are explicitly limited to the shearing of 1.4301 stainless steel sheets and under the specified parameters. Any change in the material properties or unstudied aspects, such as notch position, various clearance values and cutting speed, might substantially vary the obtained results.

6 REFERENCES

[1] Gomah, M., Demiral, M. (2020). An experimental and numerical investigation of an improved shearing process with different punch characteristics. *Strojniški vestnik - Journal of Mechanical Engineering*, vol. 66, no. 6, p. 375-384, **DOI:10.5545/sv-jme.2020.6583**.

[2] Li, X. Chen, Z. Dong, C. (2021). Failure and forming quality study of metallic foil blanking with different punch die clearances. *International Journal Advanced Manufacturing Technologies*, vol. 115, p. 3163-3176, **DOI:10.1007/s00170-021-07400-z**.

[3] Lo, S.-P., Chang, D.-Y., Lin, Y.-Y. (2007). Quality prediction model of the sheet blanking process for thin phosphorous bronze. *Journal of Materials Processing Technology*, vol. 194, no. 1-3, p. 126-133, **DOI:10.1016/j.jmatprotec.2007.04.110**.

[4] Liewald, M., Bergs, T., Groche, P., Behrens, B.A., Briesenick, B., Müller M., Niemietz P., Kubik, C., Müller, F. (2022).

Perspectives on data-driven models and its potentials in metal forming and blanking technologies. *Production Engineering*, vol. 16, no. 5, p. 607-625, **DOI:10.1007/s11740-022-01115-0**.

[5] Lubis, D.Z., Indrasepta, L.R., Bintara, R.D., Ramadhan, R., Darmawan, A.B. (2021). The effect of thickness and type of material on the sheared edge characteristics of keychain cranioplasty plate blanking product using eccentric press machine. *Journal of Mechanical Science and Technology*, vol. 5, no. 1, p. 29-35, **DOI:10.17977/um016v5i12021p029**.

[6] Mori, K., Abe, Y., Kidoma, Y., Kadarno, P. (2013). Slight clearance punching of ultra-high strength steel sheets using punch having small round edge. *International Journal of Machine Tools and Manufacture*, vol. 65, p. 41-46, **DOI:10.1016/j.ijmachtools.2012.09.005**.

[7] Klocke, F., Sweeney, K., Raedt, H.-W. (2001). Improved tool design for fine blanking through the application of numerical modeling techniques. *Journal of Materials Processing Technology*, vol. 115, no. 1, p. 70-75, **DOI:10.1016/S0924-0136(01)00771-3**.

[8] Guo, W., Tam, H.-Y. (2012). Effects of extended punching on wear of the WC/Co micropunch and the punched microholes. *The International Journal of Advanced Manufacturing Technology*, vol. 59, p. 955-960, **DOI:10.1007/s00170-011-3567-0**.

[9] Ko, D.-C., Kim, D.-H., Kim, B.-M. (2002). Finite element analysis for the wear of Ti-N coated punch in the piercing process. *Wear*, vol. 252, p. 859-869, **DOI:10.1016/S0043-1648(02)00032-7**.

[10] Mucha, J. (2010). An experimental analysis of effects of various material tool's wear on burr during generator sheets blanking. *International Journal of Advanced Manufacturing Technology*, vol. 50, p. 495-507, **DOI:10.1007/s00170-010-2554-1**.

[11] Mucha, J., Jaworski, J. (2016). The tool surface wear during the silicon steel sheets blanking process. *Maintenance and Reliability*, vol. 18, no. 3, p. 332-342, **DOI:10.17531/ein.2016.3.3**.

[12] Mucha, J., Jaworski, J. (2017). The Quality Issue of the parts blanked from thin silicon sheets. *Journal of Materials Engineering and Performance*, vol. 26, p. 1865-1877, **DOI:10.1007/s11665-017-2589-7**.

[13] Sachnik, P., Hoque, S.E., Volk, W. (2017). Burr-free cutting edges by notch-shear cutting. *Journal of Materials Processing Technology*, vol. 249, p. 229-245, **DOI:10.1016/j.jmatprotec.2017.06.003**.

[14] Krinninger, M., Feistle, M., Golle, R., Volk, W. (2017). Notch shear cutting of aluminum alloys. *Procedia Engineering*, vol. 183, p. 53-58, **DOI:10.1016/j.proeng.2017.04.010**.

[15] Feistle, M., Krinninger, M., Golle, R., Volk, W. (2012). Notch shear cutting of press hardened steels. Merklein, M., Duflou, J. R., Leacock, A. G., Micari, F. Hagenah, H. (Eds.), *Key Engineering Materials*. Trans Tech Publications Ltd, Pfaffikon, p. 477-484, **DOI:10.4028/www.scientific.net/KEM.639.477**.

[16] Stahl, J., Pätzold, I., Golle, R., Sunderkötter, C., Sieurin, H., Volk, W. (2020). Effect of one-and two-stage shear cutting on the fatigue strength of truck frame parts. *Journal of Manufacturing and Materials Processing*, vol. 4, no.2, p. 52, **DOI:10.3390/jmmp 4020052**.

[17] Mucha, J., Tutak, J. (2019). Analysis of the influence of blanking clearance on the wear of the punch, the change of the burr size and the geometry of the hook blanked in the hardened steel sheet. *Materials*, vol. 12, no. 8, art. ID 1261, **DOI:10.3390/ma12081261**.

[18] Nishad, R., Totre, A., Bodke, S., Chauhan, A. (2013). An overview of the methodologies used in the optimization processes in sheet metal blanking. *International Journal of Mechanical Engineering and Robotics Research*, vol. 2, no. 2, p. 307-318.

[19] Kumar, A., Sharma, R., Kumar, S., Verma, P. (2022). Review on machining performance of AISI 304 steel. *Materials Today: Proceedings*, vol. 56, p. 2945-2951, **DOI:10.1016/j.matpr.2021.11.003**.

[20] Sahli, M., Roizard, X., Assoul, M., Colas, G., Giampiccolo, S., Barbe, J.P. (2021). Finite element simulation and experimental investigation of the effect of clearance on the forming quality in the fine blanking process. *Microsystem Technologies*, vol. 27, p. 871-881, **DOI:10.1007/s00542-020-04983-7**.

[21] Faura, F., Garcia, A., Estrems, M. (1998). Finite element analysis of optimum clearance in the blanking process. *Journal of Materials Processing Technology*, vol. 80-81, p. 121-125, **DOI:10.1016/S09240136(98)00181-2**.

[22] Natpukkana, P., Pakinsee, S., Boonmapat, S., Mitsomwang, P., Borrisutthekul, R., Panuwannakorn, R., Khoa-phong, L. (2018). Investigation of notch shear cutting for JIS SCM420 steel wire rod. *IOP Conference Series: Materials Science and Engineering*, art. ID 012013, **DOI:10.1088/1757-899X/436/1/012013**.

[23] Hambli, R., Richir, S., Crubleau, P., Taravel, B. (2003). Prediction of optimum clearance in sheet metal blanking processes. *The International Journal of Advanced Manufacturing Technology*, vol. 22, p. 20-25, **DOI:10.1007/s00170-002-1437**.

[24] Engin, K.E., Eyercioglu, O. (2017). The effect of the thickness-to-die diameter ratio on the sheet metal blanking process. *Strojniški vestnik - Journal of Mechanical Engineering*, vol. 63, no. 9, p. 501-509, **DOI:10.5545/sv-jme.2016.4272**.

[25] Engin, K.E., Eyercioglu, O. (2016). Investigation of the process parameters on the blanking of AISI 304 stainless steel by using finite element method. *Journal of Mechanics Engineering and Automation*, vol. 6, no. 7, p. 356-363, **DOI:10.17265/2159-5275/2016.07.00-6**.

Strojniški vestnik - Journal of Mechanical Engineering 69(2023)7-8, 339-351
DOI:10.5545/sv-jme.2022.456
Original Scientific Paper
Received for review: 2022-11-19
Received revised form: 2023-05-13
Accepted for publication: 2023-05-31

Recent Advancement via Experimental Investigation of the Mechanical Characteristics of Sisal and Juncus Fibre-Reinforced Bio-Composites

Benchaabane Chaouki[1,2,*] – Kirad Abdelkader[1,2] – Aissani Mouloud[3]

[1] FUNDAPL Laboratory, Faculty of Science, University of Blida 1, Algeria
[2] Department of Mechanical Engineering, Faculty of Technology, University of Blida 1, Algeria
[3] Research Centre in Industrial Technologies CRTI, Algeria

In this work, the mechanical characteristics of unidirectional bio-composite materials reinforced by two types of natural fibres (sisal and juncus) were studied in order to develop new materials. The effect of the fibres' extraction methods and their new assembly techniques on the mechanical properties of the elaborated composites was investigated. This is based on three methods of extracting natural fibres: the first uses water treatment alone over a long period, while the second uses alkaline chemical treatment with a sodium hydroxide solution. The last method uses the burial of plant leaves in moist soil. The obtained fibres are assembled according to techniques, such as monolinear fibres, twisting fibres into rope and braiding fibres into rope. The composite materials are produced manually using a pressure-contact moulding process. The outcomes demonstrated that the resulting compounds' mechanical properties are significantly impacted by the chemical treatment. The sisal/polyester composites exhibit better mechanical tensile test behaviour than those made with juncus fibres. Moreover, contrary to the results of some other studies, the recently developed techniques of assembling with a chemical treatment process enabled the reduction of the bio-composite's thickness as well as the cost of its preparation.

Keywords: natural fibre, sisal, juncus, mechanical properties, bio-composite

Highlights

- *Three procedures are used to extract natural fibres: the first involves prolonged water treatment alone; the second involves alkaline chemical treatment using sodium hydroxide solution; the final technique uses burying plant leaves in moist soil.*
- *The sisal/polyester composites exhibit better mechanical tensile test behaviour than those made with juncus fibres.*
- *Young's modulus of the composite reinforced with sisal fibres is twice as high as that reinforced with juncus fibres.*
- *The twisted rope assembly technique exhibits the highest values of Young's modulus compared to the other forms of assembly.*
- *The recently developed technique of assembling fibres into a rope with a chemical treatment process has contributed to the best reinforcement of the bio-composite materials.*

0 INTRODUCTION

The increasing interest in plant fibres is evident due to the proliferation of documents dealing with the use of these natural or modified fibres in composite materials. These plant fibres are already occupying an important place in the composites industry thanks to their best mechanical and physicochemical properties [1]. They are used in various fields of application, such as transport, construction, medical and leisure [2] and [3]. Among the main advantages of these natural fibres are their availability in several countries, regeneration, bio-degradability, and the possibility of extraction by various methods without damaging the fibres. They can also play a remarkable role in the development of new bio-degradable green materials with desirable characteristics. This can be used to solve some of the current ecological and environmental problems.

Natural fibres have become a viable, eco-friendly, and plentiful alternative to expensive, non-renewable synthetic fibres [1]. They present a promising reinforcement for composites for some applications due to their low cost, low density, and relatively good mechanical properties [4] and [5]. In addition, they are also characterized by the absence of health risks, easy handling, high flexibility, and sound insulation [6]. Natural fibres such as sisal, linen, kenaf, Alfa and jute have been used as reinforcement in bio-composites [7] to [9].

Our interest in this work is oriented towards the search for plant fibres that are generally the most abundant during the year. Furthermore, research is moving towards the development of bio-composites with the best possible mechanical properties at a lower cost.

Generally, the mechanical properties of bio-composites are often influenced by several factors, and they heavily depend on the fibre content and, therefore, on the nature and quality of the implementation [10]. These factors can be grouped into two types based on their origin: constitutional and structural. Among the elements of the constitutional

*Corr. Author's Address: FUNDAPL Laboratory, Faculty of Science, University of Blida 1, Algeria. chaoukiben27@yahoo.com

type is the nature of the plant (kind of fibre), the nature of the resin, the physicochemical characteristics of these components (fibre/resin), the geometry of the fibre cells and their porosities, etc. The main elements of the structural type are the fibre-resin structure, the fibres' orientation, the size of the fibres, the mass fraction of the fibres, the fibre/matrix interface quality, the extraction methods and the manufacturing process of the composite (contact moulding, vacuum pressure moulding, etc.) [10].

Improving the properties of a bio-composite or its performance comes down to improving the various elements mentioned above. Therefore, among the methods of extracting plant fibres, the method of chemical treatment with sodium hydroxide (NaOH), which, according to the literature [11] to [13], facilitates the separation of fibres from the leaf matrix of their plant, by reducing impurities such as pectin, wax, and lignin around the outer surface of the fibres. It also improves the bond between the fibres/matrix of the composite to give the best mechanical results [14].

Belaadi et al. [15] indicated that the mechanical properties of polymer composites reinforced with sisal fibres are largely influenced by the mechanical properties of these fibres. Through their studies, they analysed the mechanical behaviour of sisal fibres and compared them with other bio-composites made of jute and juncus fibres; they observed the existence of the same influence of the fibres on the overall behaviour of the composites.

Joseph et al. [14] analysed the effect of water absorption on the tensile strength of sisal/polypropylene (PP) composites at different volume fractions. They found that the maximum tensile stress decreased as a function of the immersion duration. In addition, they found that sisal/PP composites with treated fibres exhibit higher strength than those of composites without treated fibres. Also, the mechanical properties of the polymer laminates reinforced with sisal fibres were studied, and they showed that the fracture stress increased with the immersion time in water during the extraction phase of these fibres [16]. In addition, the mechanical properties of the composites (epoxy type) reinforced with sisal fibres were examined. The mechanical decortication method was used to extract these fibres, which were subjected to chemical treatment with alkalis and binding agents. These pre-treated fibres showed improved mechanical and hydrophilic tendencies compared to untreated fibres. Thus, they resulted in efficient bonding at the fibre/polymer matrix interfaces [17]. The researchers also showed that the mechanical properties of the developed composites depend on various parameters, such as fibre length, fibre orientation, and fibre volume fraction [17].

Uppal et al. [18] observed that composites containing short shredded sisal fibres have high mechanical properties compared to those formed from sisal fabric. The ageing of these fibres also changes the mechanical properties of the bio-composites compared to those having newly chopped sisal fibres.

Maurya et al. [19] studied the mechanical properties of the epoxy composite reinforced with sisal fibres by varying the length of the fibre and keeping a constant weight percentage of the fibres. It was concluded that the tensile strength of the composite was not improved by reinforcing the length of the sisal fibres.

In this work, the influence of three extraction methods (with various physical aspects) of sisal and juncus fibres, as well as the new techniques for assembling these fibres, on the mechanical tensile properties of composites will be studied in order to deduce the best-elaborated bio-composite and propose it to the industry. Although they can be found on other continents as well, the sisal and juncus fibres used in this study were taken from North African plants.

1 EXPERIMENTAL

1.1 Choice of Plants and Natural Fibre Extraction Methods

The natural fibres studied were extracted from sisal and juncus plants, as illustrated by Fig.1. The choice of plants is dictated by the availability in our region of North Africa and by the rapid renewability factor during the year. There are several methods for extracting plant fibres [20], mainly according to mechanical, chemical, and biological processes.

The first fibre extraction method is mechanical, under water alone (water treatment method T_{Wt}). It consists of cutting the juncus stalks longitudinally into two slices lengthwise and in the same way for the sisal leaves; then, these sisal leaves and the cut juncus stalks are immersed in a large container of water. They will be kept for 4 days to 5 days at room temperature until fully saturated with water. The recovered sheets are then washed and dried, then mechanically tapped and manually brushed to extract the fibres. The obtained fibres from plants are shown in Fig. 2 (bundles no. 1 and 4).

The second method is a chemical method (the alkaline treatment method, T_{Alk}). After immersing the stems or the sliced leaves of the plants in water for 24 hours, a solution of sodium hydroxide (NaOH) at a 7 % concentration is added for 48 hours at

ambient temperature. Next, they are well rinsed, and the traces of NaOH are neutralized in these fibres with a 2 % distilled water solution of sulphuric acid (H_2SO_4) immersed for 30 minutes [14]. Afterwards, they are immersed in distilled water for one hour to have a neutral potential of hydrogen (PH). The leaves obtained are placed on soft ground, and with a wooden stick, these leaves and stems are struck and shaken until the fibres are separated. Finally, they are dried in a room at room temperature for 24 hours, Fig. 2, (bundles no. 2 and 3).

The third method is biological under wet ground (T_{Gr}). It consists of burying the leaves and stems of sisal or juncus in the wet ground for 55 days to 57 days [21]. These sheets must be cut longitudinally beforehand into two or three parts; this promotes the biodegradation of these leaves, thus making the extraction of the fibres easier. Then, the obtained fibres are washed with water and then dried at room temperature, Fig. 2 (bundle no. 5).

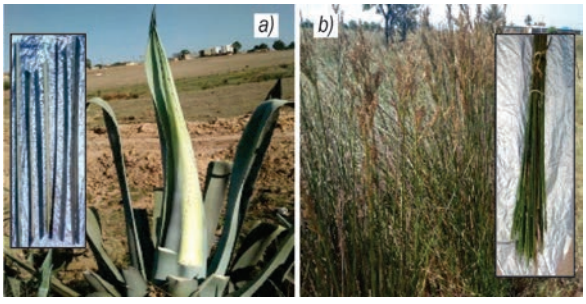

Fig. 1. *Studied plants in their natural habitat; a) sisal and b) juncus*

Fig. 2. *Some natural fibres obtained by different methods of extraction; no. 1, 2, 5 sisal's fibres, and no. 3 and 4 juncus' fibres*

1.2 Forming the New Assembly of Plant Fibres

The assembly of both studied fibres in the structure of composite materials is manually placed into two new rope shapes, with the addition of the usual form of linear assembly. The first one forms ropes by braiding or torsion, the second one forms ropes by twisting, and finally, it forms unidirectional straight fibres without overlapping, so we named this last assembly "mono-linear". The strings contain six fibres each.

1.2.1 Assembly in Ropes by Braiding

A braid is an assembly of bundles of fibres with a total of six threads. The different wicks of fibres pass alternately between them (Fig. 3a), such that the left strand is passed over the neighbouring strand and below the following one. It proceeds in this way until the last strand. The crossing of the wicks is done at a right angle and offers an oblique checkerboard pattern (Fig. 3a).

1.2.2 Assembly in Ropes by Torsion

In this mode of assembly, the six fibre threads are grouped in parallel and twisted in pairs (2×2×2 threads), then twisted together so as to form the rope by torsion (Fig. 3b). In this second case, the strands of twisted fibres are placed in a spiral whose centre is that of the rope.

1.2.3 Straight Unidirectional Assembly of the Fibres (Mono Linear)

In this last and usual mode of assembly, the fibres are grouped in parallel, quasi-straight and unidirectional lines without overlapping (Fig. 3c).

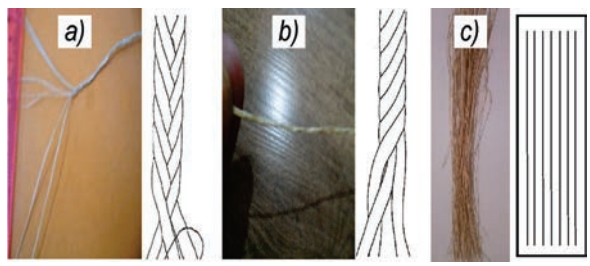

Fig. 3. *Assembly of fibres into a) ropes by braiding, b) ropes by twisting, and c) monolinear*

1.3 Fabrication of Laminated Composite Plates and Single Resin Plates

In order to fabricate our plates of bio-composite materials, we first prepared the plant fibres and then assembled them. Secondly, a polyester-type resin based on three components was also prepared. This type of polyester was chosen because it is the most used and the cheapest. The polyester matrix is therefore obtained by mixing a primary resin with a

hardener (7 %) and an accelerator (3 %) by volume. Polyester-only (resin) tensile specimens are obtained from manually prepared plates. These specimens are used as a reference for the bio-composite specimens.

Unidirectional sisal/polyester and juncus/polyester laminated plates (bio-composite) are made in mono-layers, such that the mass of fibres in a plate is approximately 30±0.5 g. The ends of the fibres are attached by double-sided adhesive tape to the edges of the mould during their deposits. This is done to ensure that the directions of the fibres are parallel and straight when casting the resin manually.

The composite plates were fabricated using the contact moulding method. The thicknesses of the plates are checked using metal wedges (2±0.1mm). The bio-composites are impregnated at room temperature (25±1 °C). The polyester resin obtained is catalysed and hardened in proportions of between 2 % and 3 % by mass of the primary resin.

Once the plates are reticulated, they all undergo a 24-hour polymerization cycle at room temperature before demoulding. In order to have a total polymerization of the polyester resin, the laminated plates are left in the open air for 3 days before being cold cut into test specimens. The bio-composite plates produced in dimensions of 180 mm×170 mm are cut into specimens according to the ASTM 3039 standards, as cited by Hassan and Abdullah [22]. In order to estimate the fibres' mass rate, each plate was weighed with a precision electronic balance (0.01 g). The tensile specimens (Fig. 4a) are in accordance with the ASTM 3039 standard [23] and have the following dimensions: Total length $L=175$ mm, thickness $h=2$ mm and width $b=25$ mm.

Fig. 4b shows some tensile specimens of bio-composites with wedges in their ends.

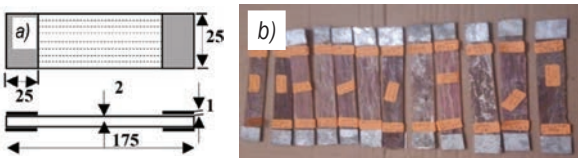

Fig. 4. *a) Schematic specimen with its dimensions; and b) some tensile specimens of bio-composite with wedges in their ends*

1.4 Mechanical and Structural Characterization of Bio-composites

To characterize the laminated plates produced, the mechanical properties and microstructure of all bio-composites elaborate are studied. The determination of the main mechanical properties is carried out via monotonic tensile tests under a universal machine of the Zwick-GmbH type (Fig. 5a). The tests are carried out with a pre-load of 1N until failure. To ensure good reproducibility of the results, at least three specimens for each category were tested at the same speed, which was quasi-static on the order of 1 mm/min. The direction of the tensile forces is the same as the orientation of the fibres. The length of the metal standards (wedge) placed at the end of the test specimens is equal to 25 mm. The latter serves to prevent crushing under the jaws of the universal testing machine (UTM). The longitudinal direction of the specimens is chosen to be the same direction as that of the fibres. Fig. 5b shows a bio-composite specimen under axial tensile loading with a zoom lens showing crack initiation.

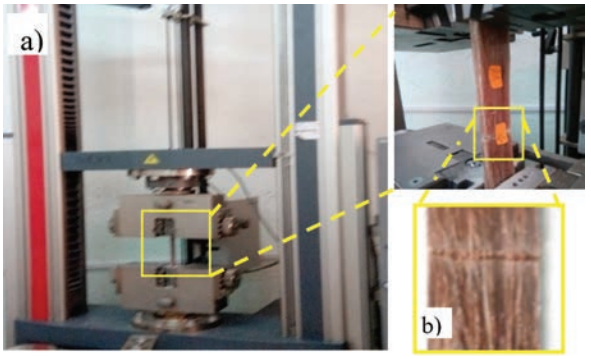

Fig. 5. *a) Tensile testing machine with zoom under the test, and b) zoom after tensile test*

Observation analyses of sisal and juncus fibres without resin and others into resin were carried out using optical microscopy (OM) and scanning electron microscopy (SEM).

2 RESULTS AND DISCUSSIONS

2.1 Mechanical Properties of Polyester Resin

Fig. 6 shows the curves of tensile testing of specimens in polyester-alone resin, and an example of a broken tensile specimen is illustrated. Each time, three specimens are tested. It is noted that the shapes of these curves are very close to each other except for a slight shift in elongation during the rupture phase. The overall mechanical behaviour of the resin specimens shows a bilinear stress-strain relationship, followed by sudden rupture. The elastic limit is approximately 5±0.5 MPa (Fig. 6). Young's modulus, the tensile strength, and the deformation of each specimen are grouped together in Table 1, associated with mean values.

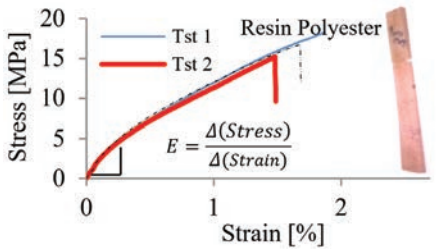

Fig. 6. *Curves of tensile tests of polyester specimens alone and an example of the specimen after the test*

Table 1. *Summary of the mechanical properties of the polyester resin specimens*

Specimens	Young's modulus E [GPa]	Plastic zone modulus $E2$ [GPa]	Maximum tensile strength Rm [MPa]	Rate of deformation [%]
Tst1	1.701	0.871	18.25	1.80
Tst2	1.533	0.805	15.12	1.52
Tst3	1.811	0.805	16.41	1.67
Average values	1.681 ±0.148	0.827 ±0.044	17.33 ±2.21	1.66 ±0.16

Table 1 shows the average maximum stress reaching a value of 17.33 MPa before the specimen breaks. This value is comparable to those given in references **[24]** and **[25]**. Young's modulus (elastic zone) has an average value of 1.681 GPa, and that of the plastic zone is around 0.827 GPa, with an error of ±0.15 GPa. However, the rate of deformation is of the order of 1.66±0.16 %. These results will serve as a reference for the composites to be developed.

2.2 Young's Modulus of Developed Bio-composites

The results of Young's modulus of the specimens of the different cases developed with the sisal fibres (Fig. 7a) and the juncus fibres (Fig. 7b) are presented in histograms. The different cases studied concern the three methods of extraction (chemical treatment T_{Alk}, water treatment T_{Wt}, and stripping in the wet ground T_{Gr}) and the three forms of fibre assembly (assembly in cords by twisting "#1", in cords by braiding "#2", and fibres in straight lines noted mono-linear "#3").

Overall, it can be seen that Young's modulus E of the composites is higher than that of the pure resin, and its value has been amplified several times (from 2 to 7 times that of the resin, depending on the nature of the fibres; Fig. 7) by the addition of fibres. From this Fig. 7, the effect of the extraction method on Young's modulus of the composites can therefore be classified according to their values as elasticity modulus E according to the extraction method, is classified by Eq. (1):

$$E_{Res\ Ref} < E_{Twt} < E_{TGr} < E_{TAlk}. \quad (1)$$

This result is valid for both cases of plants regardless of the type of assembly form. From Fig. 7a, Young's modulus of composites reinforced by sisal fibres and obtained by chemical treatment ($S-1\_T_{Alk}$) is compared to the modulus of the same composite obtained with water treatment ($S-1\_T_{Wt}$); it shows an increase of approximately 70.01 %. However, the comparison of Young's modulus of ($S-1\_T_{Gr}$) with that of ($S-1\_T_{Wt}$) gave an increase in value of about 13.60 %. The same observation of an increase in modulus is observed for the other cases of $S-2$ and $S-3$, but with low percentage values. It is concluded that the extraction method by treatment with NaOH has increased Young's modulus value of the composite compared to the other extraction methods. This observation is in accordance with some of the literature **[26]** and **[27]**.

Young's modulus of composites reinforced with juncus fibres (Fig. 7b) evolves in the same way as that of sisal, according to the different extraction methods, but with a difference in value. This reveals the importance and interest in using chemical treatment of fibres. However, there is no case for under wet ground (T_{Gr}) extraction for this juncus plant.

Note: this last method of extraction by the under wet ground technique on juncus fibres was not successful during the tests, so its effect was not studied. This is due to the very fast degradation and deterioration of these fibres during the execution of this method because of the low amount of pectin in this plant.

It can be summarized that for the same nature of fibre and for a given extraction method, Young's modulus E of the composite evolves according to the three forms of assembly as indicated in Eq. (2). It is noticed that the case of twisting assembly (#1) presents the highest values of the modulus compared to the other forms of assembly (#2, #3). They can therefore be classified by Eq.(2):

$$E^{\#3} < E^{\#2} < E^{\#1}. \quad (2)$$

It is observed that Young's modulus of the sisal-reinforced composite is twice as high as that of the juncus-reinforced composite for the same characteristics. Therefore, these results have helped to highlight these new fibre assembly techniques in the field of bio-composites. The main mechanical properties of the elaborated biocomposite

materials (sisal/polyester and juncus/polyester) are summarized in Table 2 (S = sisal; J = juncus). Thus, it can be deduced from the values of the ultimate tensile strength that the latter has almost the same evolutionary trend as that of Young's modulus in the different cases (Eq. (1)). Also, it was shown that the mechanical properties of the composites are improved compared to the resin-only case several times. In fact, the *Rm* of the composites increases by 4 to 5 times with the use of sisal fibres and by 2 times to 3 times with juncus fibres.

2.3 Influence of the Fibre Assembly Form on Mechanical Properties of Bio-composites

2.3.1 Case of Rope Assembly by Twisting #1

Fig. 8 shows the evolution of the tensile stress as a function of strain for different composites according to the three extraction methods (T_{Alk}, T_{Wt} and T_{Gr}), for which a pure resin curve is introduced as a reference (Res−Ref). The fibres of composites (sisal and juncus) are assembled in rope by twisting.

The figure illustrates a large shift between the curves of reinforced composites with sisal, juncus and

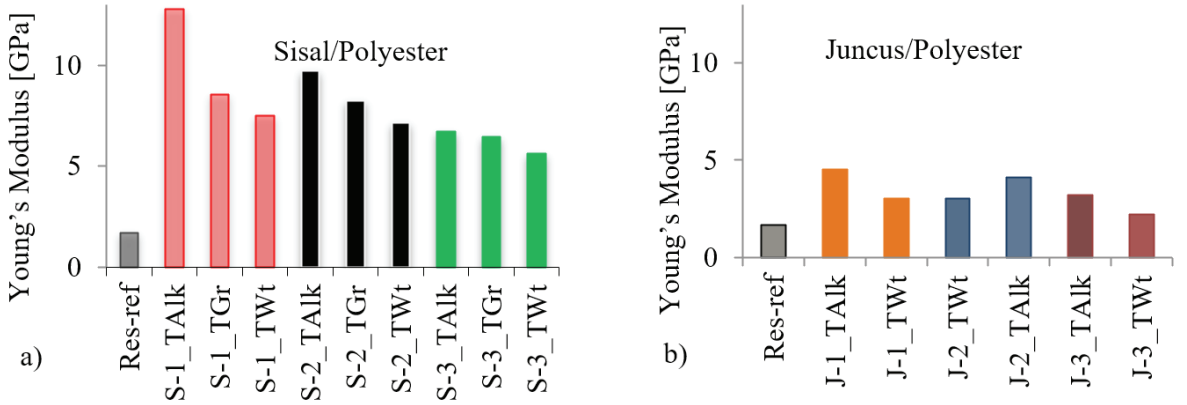

Fig. 7. *Young's modulus evolution of composites; a) sisal/polyester, and b) juncus/polyester*

Table 2. *Tensile mechanical proprieties of the composites produced (sisal and juncus/polyester)*

Fibres/ matrix	Composite types	Symbol	Young's Modulus E [GPa]	Modulus of plastic zone $E2$ [GPa]	Ultimate tensile strength Rm [MPa]	Strain ε [%]
Polyester	Resin-Ref N°1	Res-ref	1.701	0.871	18.25	1.80
Sisal (S)	S- in rope by twisting with NaOH treatment (Alkaline)	$S-1\_T_{Alk}$	12.77	4.693	95.24	2.13
	S- in rope by braiding with NaOH treatment (Alkaline)	$S-2\_T_{Alk}$	9.724	4.057	88.02	2.30
	S- monolinear with NaOH treatment	$S-3\_T_{Alk}$	6.704	3.176	74.80	2.88
	S- twisting rope with an underground processing T_{Gr}	$S-1\_T_{Gr}$	8.524	3.728	82.30	2.35
	S- braiding rope with T_{Gr}	$S-2\_T_{Gr}$	8.229	3.828	74.76	2.50
	S- monolinear with T_{Gr}	$S-3\_T_{Gr}$	6.436	2.843	74.80	3.04
	S- twisting rope with water treatment T_{Wt}	$S-1\_T_{Wt}$	7.501	3.930	73.89	2.59
	S- braiding rope withT_{Wt}	$S-2\_T_{Wt}$	7.146	3.396	72.51	2.91
	S- monolinear with T_{Wt}	$S-3\_T_{Wt}$	5.635	2.810	72.17	3.21
Juncus (J)	J- twisting rope with NaOH treatment	$J-1\_T_{Alk}$	4.529	2.346	55.40	2.78
	J- braiding rope with NaOH treatment	$J-2\_T_{Alk}$	4.103	2.074	53.49	3.14
	J- monolinear with NaOH treatment	$J-3\_T_{Alk}$	3.187	1.335	43.27	3.92
	J- twisting rope with T_{Wt}	$J-1\_T_{Wt}$	3.045	1.659	47.70	3.23
	J- braiding rope with T_{Wt}	$J-2\_T_{Wt}$	3.041	1.455	46.61	3.46
	J- monolinear with T_{Wt}	$J-3\_T_{Wt}$	2.230	1.193	45.29	4.60

pure resin. The spacing between curves (the slopes and the maximum values (peak)) is clearly different. This is due to the intrinsic nature of each substance, which is quite different. The shape of these curves represents two quasi-linear phases followed by an abrupt rupture (brittleness). It is a very short elastic zone followed by a wider one: the plastic zone (from approximately 0.2 % of the deformation). Thus, it is bilinear behaviour for the three materials (Fig. 8).

This behaviour is due to the natural response of the fibre reinforcements and due to the specificity of the fibre/resin interface of each composite.

It can be seen from the various curves that the maximum values (peaks) of the breaking stress are between 95.24 MPa of ($S-1\_T_{Alk}$) and 45.29 MPa of ($J-3\_T_{Wt}$) and are always followed after these maximums by a sudden break. This is obtained with an elongation between 2.13 % and 4.60 % (Table 2).

It is concluded that the highest *Rm* i.e. the maximum stress at failure corresponds to the composite reinforced with sisal fibres and elaborated by the NaOH treatment.

While the maximum stress at break corresponding to the juncus-reinforced composite (Fig. 8) is about 55.4 MPa ($J-1\_T_{Alk}$) with an elongation of 2.78 %, this plant gives a composite that is lower in maximum stress but has more elongation and is, therefore, more ductile than sisal. This is also due to its weak nature (low cell pectin density), resulting from the fact that the diameters of their fibres are narrower than those of sisal.

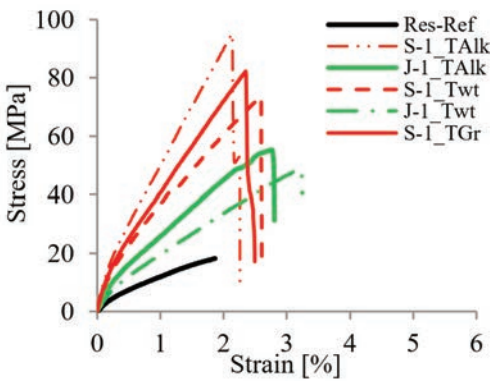

Fig. 8. *Tensile curves of resin and laminates assembled in rope by twisting (according to extraction methods)*

2.3.2 Case of Rope Assembly by Braiding #2

Fig. 9 shows the evolution of the tensile stress as a function of the deformation of the composites, where the fibres (sisal and juncus) are assembled in rope by braiding according to the three extraction methods.

It is found that the mechanical properties of bio-composite materials reinforced with sisal fibres are better than those reinforced with juncus fibres, with an increase in *Rm* of about 64 % and 55 % compared to juncus fibres (Fig. 9). This leads us to recommend the use of sisal fibres in bio-composites over juncus fibres.

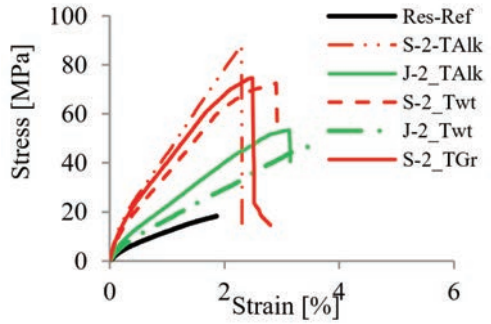

Fig. 9. *Tensile curves of resin and laminates assembled in rope by braiding (according to extraction methods)*

These results are similar to the previous case (fibres assembled in rope by twisting) and have a maximum increase of $Rm \approx 72$ % (Fig. 8). It can also be deduced that the twisting assembly is better than the braiding assembly.

2.3.3 The Case of Mono-Linear Assembly of the Fibres #3

Fig.10 shows the evolution of the stress to failure as a function of the deformation of the same laminates as above, but the fibres are assembled in a mono-linear fashion. As before, a large gap between the three curves (sisal, juncus, and pure resin) can be observed. This is due to the same reasons as before (rope assembly by twisting and braiding). It can be seen that there are also two quasi-linear phases in their overall behaviour. It can be seen that the maximum value of the stresses at failure (≈ 70 MPa) is lowered by about ≈ 25 % compared to the first case (by twisting), while their deformations were enlarged in the majority for this assembling case. This can be justified by the installation of the fibres in the resin in an evenly spaced manner without overlapping. It reduces the maximum stress by their dispersion but facilitates the elongation of the bio-composite. It can be seen that sisal has always kept the best mechanical behaviour compared to juncus. The latter keeps the large elongations.

Finally, it can deduce that the composites having an assembly in rope by twisting have better mechanical behaviour than those obtained by the fibres assembled in a monolinear fashion for the same type of plant.

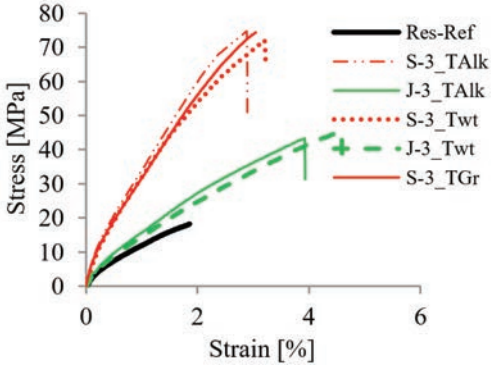

Fig. 10. *Tensile curves of resin and elaborated laminates by mono linear assembling (according to extraction methods)*

2.4 Influence of the Fibre Extraction Method on Mechanical Properties of Bio-composites

Fig. 11 shows the stress versus strain curves after the tensile test of the same composites for the three fibre extraction methods. The results in Fig.11a show the behaviour of the different composites obtained via the chemical treatment method (T_{Alk}). The shapes of the curves show a difference from one composite to another with a ranking discussed previously and prove that the behaviour of composites with sisal fibres is better than those with juncus fibres. Fig. 11b shows the effect of using the fibre extraction method with water treatment (T_{Wt}) on the tensile behaviour. For the same type of plant (same fibres), these curves are approaching each other, whatever the type of assembly (#1, #2 or #3).

Fig. 11c illustrates the effect of the under wet ground extraction method (T_{Gr}) on the behaviour of the composites according to the tensile curves. The first point that draws attention is the absence of composites with juncus fibres. It is also observed in Fig. 11c that the curves (of S1 and S2) belonging to th s T_{Gr} method are very close to each other (a very small deviation) with respect to (S3) for the behaviour of this sisal fibre composite. However, they are all far from the Resin-pure reference curve. Nevertheless, it can be observed that the peak of the maximum stresses of these curves lies between the two previous cases (the maximums) of Figs. 11a and b.

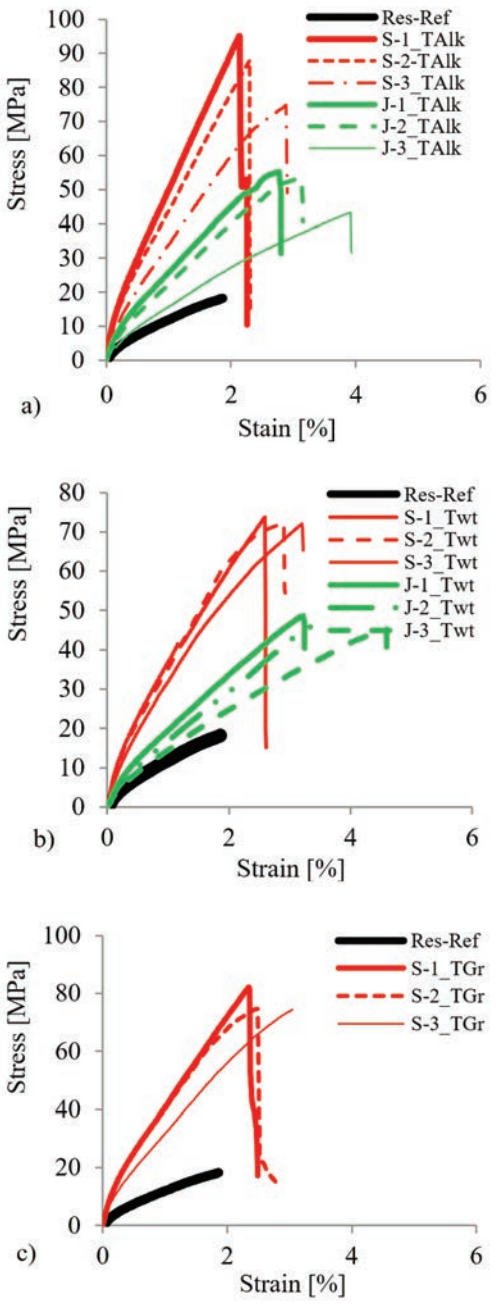

Fig. 11. *Tensile curves of the same composites showing the influence of extraction methods, a) T_{Alk}, b) T_{Wt} and c) T_{Gr}*

It is deduced that the T_{Alk} extraction method gives the best improvements on the mechanical properties of composites with both types of fibres (sisal and juncus). Since the NaOH treatment changes the topography of the fibre surface, it removes wax, pectin, and part of the lignin. Indeed, the removal of these components is necessary because their presence leads to lower tensile strength. It is concluded that the stress at break increases with the complexity of the

extraction method while the strain at break decreases overall. This is attributed to the reduced mobility of hydrogen bonds between the matrix and fibres to roughen the fibre surface [28] and so improve the quality of the fibre/matrix interface.

2.5 Structural Characterization of the Elaborated Bio-composites

2.5.1 Observation of Different Fibres Used

Fig. 12 shows typical optic micrographs of sisal fibres obtained by the T_{Alk} and T_{Gr} extraction methods, respectively. The other measurements of the fibre diameters are summarized in intervals and in average values in Table 3, according to the nature of the plants and the extraction methods. The average diameters were determined from five samples (fibres) on the median part of their length. These measurements show the effect of the extraction method on the average value of the fibre diameter.

Table 3. *Diameter measurement values for the fibres of sisal and juncus*

Fibre type	Extraction method	T_{Alk}	T_{Wt}	T_{Gr}
Sisal fibres	Diameters [μm]	210-330	270-360	340-560
	Average value [μm]	270	315	450

Fibre type	Extraction method	T_{Alk}	T_{Wt}
Juncus fibres	Diameters [μm]	110-220	170-260
	Average value [μm]	165	215

It is found that the first extraction method, T_{Alk} gives fibres with relatively small diameters compared to the other methods, such as 270 µm for sisal and 165 µm for juncus. This is probably due to the alkaline chemical treatment, which forces the fibres of the plant matrix to detach completely and results in fine fibres with smooth side surfaces. The second method T_{Wt} shows a remarkable increase in the measured fibre diameter values (Table 3).

The last method T_{Gr} reveals larger values of fibre diameters than before or sisal fibres. Thus, it is noted that with the last method, the increase ratio in average diameters compared to the first method is of the order of 66 %.

Other results can be summarised as follows.

On the surface of the fibres, traces of pectin and plant matrix cells were observed, despite a good rinsing. As a result, these traces of plant matrix participated in the increase of fibre diameters and thus reduced their number if used in the laminate for the same mass of fibres compared to other fibres obtained by other extraction methods and used in bio-composites. This resulted in weaker mechanical properties when testing the composites made by this method (T_{Gr}) and compared to the first treatment method (T_{Alk}).

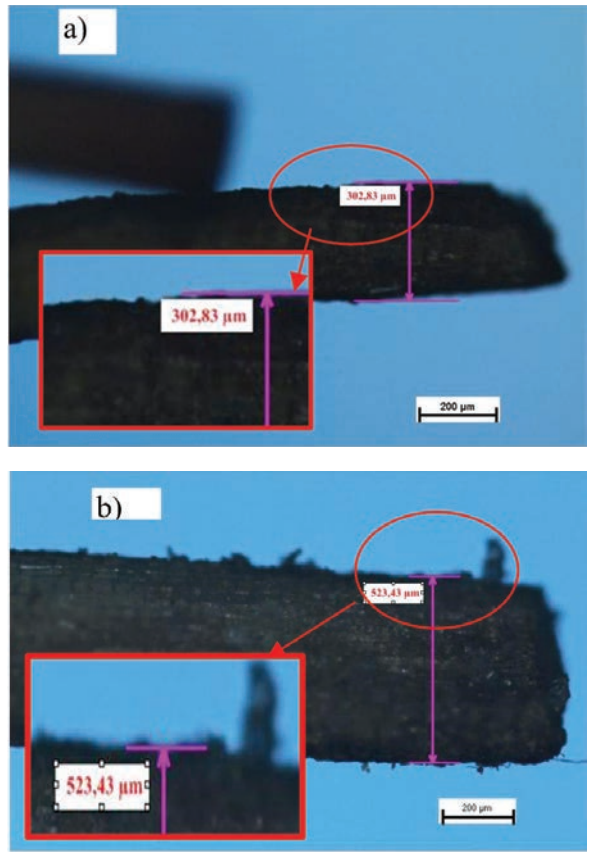

Fig. 12. *Typical optical micrographs of sisal fibres according to the above extraction methods, a) T_{Alk}, b) T_{Gr}*

Further measurements of the fibre diameter of any plant also show a small increase in the resin. Thus, the fibres in the resin were swollen (diameter increase of about 18 % to 20 %). For example, through some measurements of sisal fibres (T_{Gr}), the swelling ratio of this fibre is about 20.7 % (i.e., from 362 µm to 437 µm). This finding is also confirmed by Motaung et al. [9].

2.5.2 Structural Observation of the Developed and Tested Bio-composites

Longitudinal Observations of the Samples after Tensile Test

To characterize the interface between the fibres and the matrix after the tensile test and to see the fracture surfaces, the scanning electron microscope

(SEM) observation technique was used. Fig. 13 shows the fractured specimens of bio-composites reinforced with sisal fibres (front view), obtained by the T_{Alk} elaboration method and according to both fibre-assembling techniques (assembling in mono-linear technical and assembling in rope by twisting).

From the revealed images, it is globally observed that the failure that occurred in the samples was a combination of failure along the fibre-matrix interface and failure of some fibres, as well as matrix fracture. However, composite matrix failure after tensile failure generally exhibits brittle fracture. Fig. 13a shows a global view and its zoom of a rupture of the specimen obtained by the T_{Alk} extraction method and the fibres assembled with the mono-linear technique. It can be seen that there are some extended sisal fibres and some broken ones. The matrix has, in addition to its transverse fracture cracks, fragments attached to the fibres, showing the cohesion of the fibres with the matrix and the quality of the fibre-matrix interface.

Fig. 13b shows a wide view and zoom of a specimen fracture obtained by the same extraction technique, but the fibres are assembled in rope. The same observations as before can be made in this case, but the fibres are additionally bent in flexion, and the matrix fragments are more numerous than before. The mechanism of rupture of the matrix is also shown by even more numerous longitudinal cracks. This demonstrates a strong attachment at the fibre-matrix interface. This is also affirmed by its tensile results, showing a clear improvement and thus giving the best case of the tensile tests.

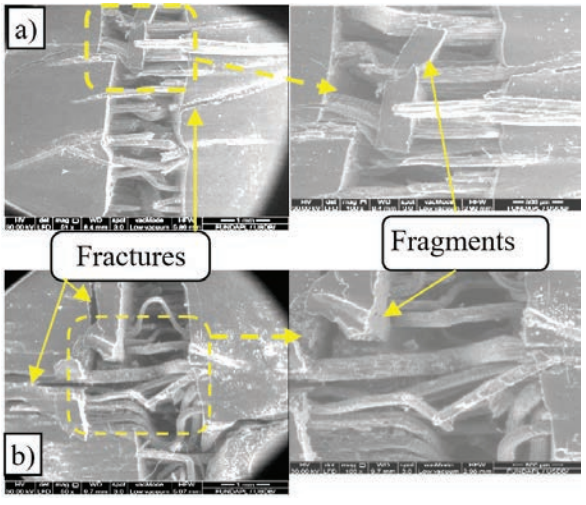

Fig. 13. *Global view and its zooms of a sisal specimen rupture obtained by the T_{Alk}; a) fibres assembled in mono linear technical and b) fibres assembled in ropes*

Fig. 14 shows laminated rupture specimens reinforced with the juncus fibres obtained via the T_{Wt} extraction method and assembled in mono-linear technical (T_{Wt} / Assemb-linear). It illustrates a global view and a magnified view of a part of the rupture. It is always observed after the tensile test that the polyester matrix fracture shows a brittle transverse break. It can be observed that the fibres underwent slippage, cracks and longitudinal with transverse breaks, showing a weak cohesion of the fibres with the matrix.

This resulted in a very low-quality fibre-matrix interface. Also, it is proved by the tensile tests, which give the lowest case for this juncus plant. It can be concluded that the T_{Wt} method does not give the best case of fibre-matrix junction in the composite. The same finding was obtained for the sisal plant with this method T_{Wt}.

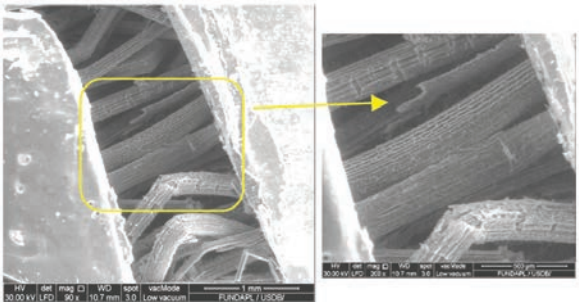

Fig. 14. *Global view and zoom of rupture specimen reinforced with the juncus fibres using the TWt /Assemb-linear production methods*

Cross-sectional Observations of the Specimens

Fig. 15 shows the transverse fracture surfaces of the bio-composite specimens reinforced with sisal. The portion of the specimen selected for observation corresponds to the best case of tensile test and complete rupture. This figure shows the shear surface morphology of the matrix and the sisal fibres state for two zones (Figs. 15a and b) in a selected specimen. It is observed that in Fig. 15a, the matrix surface is almost smooth, and there are fibre groups indicating a rope assembly. Fig. 15b shows some fibres having the burst tear with some micro-fibres and others in transverse rupture, as well as gaps on the matrix surface, which correspond to the location of other detached fibres. Therefore, the difference between Figs. 15a and b is that Fig. 15b illustrates more detail of the cross-sectional morphology of specimen rupture. Fig. 15c shows a magnified view of cut fibre that has a condensed capillary structure with a nearly flattened cross-section.

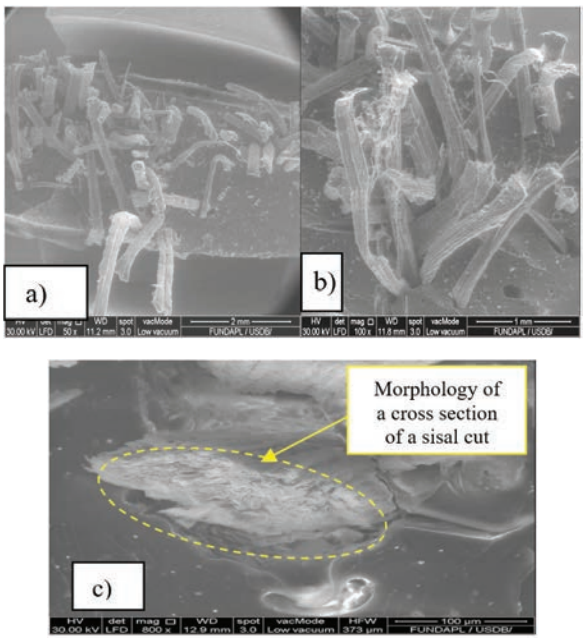

Fig. 15. *a) and b) global view of shear surface morphology of the matrix and the sisal fibres for two zones, and c) zoom of cut fibres*

3 CONCLUSIONS

This work aims to develop and elaborate the bio-composites with sisal and juncus fibres, analyse the effect of the elaboration of these materials on their mechanical properties and thus recommend the best case. The fibres are obtained via three extraction methods and assembled in three types of assembly, two of which are new techniques to form ropes in the matrix of these composites. The elaborate matrix is made of unsaturated polyester.

The first method of extraction is based on the effect of water alone for a long time (T_{Wt}), while the second method is based on an alkaline chemical treatment by a NaOH solution of 7 % concentration (T_{Alk}). The last method consists in exploiting the effect of the humidity under the ground (T_{Gr}). The selected fibres are assembled in three types, such as the first one in mono-linear fibres without overlaps, then groups of fibres in rope by twisting and in rope by braiding.

The tensile tests reflect a bilinear behaviour with a brittle fracture in the majority of the elaborated bio-composites. The classification according to the average mechanical characteristics of the different combinations in decreasing order is as follows: the case of assembly by twisted rope, then braided rope, and the last case in mono linear fibres. The classification by the extraction method is the Alkaline treatment with NaOH (T_{Alk}), treatment under wet ground (T_{Gr}), and treatment with water alone (T_{Wt}).

The mechanical properties of these bio-composites depend on the type of fibre, its diameter, the way of assembly, and the method of extraction of these fibres. The improvements resulting from the treatment with NaOH solution have changed the topography of the lateral surface of the fibres, eliminating the wax, pectin, hemicellulose and part of the lignin. The composites with sisal fibres show the best mechanical behaviour in tensile than those elaborated with juncus fibres. The difference is more than 200 %. The case of twisted rope assembly presents the highest values of Young's modulus compared to the other forms of assembly. The Young's modulus of the composite reinforced with sisal is twice as high as that reinforced with juncus for the same characteristics.

Optical microscopy analysis allowed the measurement of the diameter of the sisal and juncus fibres. The fibres in the resin underwent a swelling of about 18 % to 20 %. These measurements show the effect of the extraction method on the average value of the diameter of a fibre. The best fibres are those with more cleanliness without residual impurities and smaller diameters. Structural analysis of the bio-composites by SEM showed that those obtained by the NaOH solution extraction method (T_{Alk}) present the best cohesion of the fibres with the matrix. The post-tensile morphology of the specimen failures shows that the failure was a combination of failure along the fibre-matrix interface and fracture of some fibres as well as a brittle transverse failure of the polyester matrix.

Finally, the best bio-composite material developed and recommended is the one obtained by combining the extraction method based on NaOH treatment (7 %) with the sisal fibres assembled in rope by twisting. This combination contributed to reducing the thickness of bio-composites compared to the bibliography and improved their mechanical properties.

4 ACKNOWLEDGEMENTS

The authors would like to thank for the support of the Ministry of Higher Education and Scientific Research of Algeria.

5 NOMENCLATURE

T_{Alk} Treatment with NaOH (Alkaline),
T_{Wr} Treatment with water alone,

T_{Gr} Treatment in the wet ground,
#1, #2 Rope Assembly by twisting, by braiding,
#3 Mono Linear Assembly of the fibres,
E Young's modulus, [GPa].

6 REFERENCES

[1] Syduzzaman, M., Al Faruque, M.A., Bilisik, K,. Naebe, M. (2020). Plant-based natural fibre reinforced composites. A review on fabrication, properties and applications. *Coatings*, vol. 10, no. 10, p. 973-985, **DOI:10.3390/coatings10100973**.

[2] Mbeche, S.M., Wambua, P.M., Githinji, D.N. (2020). Mechanical properties of sisal/cattail hybrid-reinforced polyester composites. *Advance in Materials Science and Engineering*, vol. 2020, art. ID 6290480, **DOI:10.155/2020/6290480**.

[3] Oladele, I.O., Omotosho, T.F., Adediran, A.A. (2020). Polymer-based composites an indispensable material for present and future applications. *International Journal of Polymer Science*, vol. 2020, art. ID 8834518, **DOI:10.1155/202-0/8834518**.

[4] Pantano, A., Bongiorno, F., Marannano, G., Zuccarello, B. (2021). Enhancement of static and fatigue strength of short sisal fibre biocomposites by low fraction nanotubes. *Applied Composite Materials*, vol. 28, p. 91-112, **DOI:10.1007/s10443-020-09857-9**.

[5] Balsam, H.A., Ali, A.B., Abdul, H.K. (2021). Effect of immersion media for polyester composite reinforced with chicken feathers on creep behaviour. *Strojniški vestnik - Journal of Mechanical Engineering*, vol. 68, no. 6, p. 377-384, **DOI:10.5545/sv-jme.2021.7471**.

[6] Mohan, S.K., Ganesan, A.T., Ramarao, M., Mangrulkar, A.L., Rajesh, S., Al Obaid, S., Alfarraj, S., Sivakumar, S., Ganesan, M. (2021). Evaluation of mechanical properties of sisal and bamboo fibres reinforced with polymer matrix composites prepared by compression moulding process. *Advances in Materials Science and Engineering*, vol. 2021, art. ID 2832149, **DOI:10.1155/2021/2832149**.

[7] Sandino, T., Roberto, O., Pablo, A., Edisson, C. (2021). Hot incremental forming of biocomposites developed from linen fibres and a thermoplastic matrix. *Strojniški vestnik - Journal of Mechanical Engineering*, vol. 67, no. 3, p. 123-133, **DOI:10.5545/sv-jme.2020.6936**.

[8] Sathish, T., Mohanavel, V., Velmurugan, P. (2022). Investigating influences of synthesizing eco-friendly waste-coir-fibre nano filler-based ramie and abaca natural fibre composite parameters on mechanical properties. *Bioinorganic Chemistry and Applications*, vol. 2022, art. ID 6557817, **DOI:10.1155/2022/6557817.**

[9] Motaung, T.E., Linganiso, L.Z., Kumar, R., Anandjiwala, R.D. (2017). Agave and sisal fibre reinforced polyfurfuryl alcohol composites. *Journal of Thermoplastic Composite Materials*, vol. 30, no. 10, p. 1323-1343, **DOI:10.1177/0892705716632858**.

[10] Bajpai, P. (2015). *General Background, in Green Chemistry and Sustainability in Pulp and Paper Industry*, Springer, Cham, **DOI:10.1007/978-3-319-18744-0_1**.

[11] Archana, D.P., Jagannatha, R.H.N., Basavaraju, P. (2022). Mechanical characterization of biocomposites reinforced with untreated and 4% NaOH treated sisal and jute fibres. *Advances in Materials Science and Engineering*, vol. 2022, art. ID 7777904, **DOI:10.1155/2022/7777904**.

[12] Oladele, I.O., Omotoyinbo, J.A., Adewara, J.O.T. (2010). Investigating the effect of chemical treatment on the constituents and tensile properties of sisal fibre. *Journal of Minerals & Materials Characterization & Engineering*, vol. 9, no. 6, p. 569-582, **DOI:10.4236/jmmce.2010.96041**.

[13] Ayalew, A.A., Wodage, A.F. (2022). Characterization of chemically treated sisal fibre/polyester composites. *Journal of Engineering*, vol. 2022, art. ID 8583213, **DOI:10.1155/2022/8583213**.

[14] Joseph, P.V., Rabello, M.S., Mattoso, L.H.C., Joseph, K., Thomas, S. (2002). Environmental effects on the degradation behaviour of sisal fibre reinforced polypropylene composites. *Composite Science and Technology*, vol. 62, no. 10-11, p. 1357-1372, **DOI:10.1016/S02663538(02)00080-5**.

[15] Belaadi, A., Abderrezak, B., Mostefa, B., Fabrizio, S. (2013). Tensile static and fatigue behavior of sisal fibres. *Materials and Design*, vol.46, p. 76-83, **DOI:10.1016/j.matdes.2012.09.048**.

[16] Alvarez, V.A., Fraga, A.N., Vasquez, A. (2004). Effects of the moisture and fibre content on the mechanical properties of biodegradable polymer-sisal fibre biocomposites. *Journal of Applied Polymer Science*, vol. 91, no.6, p. 4007-4015, **DOI:10.1002/app.13561**.

[17] Senthil, K., Saba, N., Rajini, N., Chandrasekar, M., Jawaid, M., Siengchin, S., Alotman, O.Y. (2018). Mechanical properties evaluation of sisal fibre reinforced polymer composites: A review. *Construction and Building Materials*, vol. 174, p. 713-729, **DOI:10.1016/j.conbuildmat.2018.04.143**.

[18] Uppal, N., Pappu, A., Patidar, R., Gowri, V.S. (2019). Synthesis and characterization of short sisal fibre polyestercomposites. *Bulletin of Material Science*, vol. 42, art. ID132, **DOI:10.1007/s12034-019-1792-6**.

[19] Maurya, H.O., Gupta, M.K., Srivastava, R.K.., Singh, H. (2015). Study on the mechanical properties of epoxy composite using short sisal fibre. *Materials Today: Proceedings*, vol. 2, no. 4-5, p. 1347-1355, **DOI:10.1016/j.matpr.2015.07.053**.

[20] Venkata, R.D., Lakshumu, N., Abahubalendruni, M.V.A.R. (2018). A review on mechanical behaviour of polymers/ sisal fibre reinforced composites material. *International Journal of Scientific Development and Research*, vol. 3, no. 12, p. 190-199.

[21] Mouhoubi, S., Osmani, H., Bali, T., Abdeslam, S. (2012). Elaboration et étude des propriétés des composites polyester/ alfa traite et non traite. *Verres, Céramiques & Composites*, vol. 2, p. 34-40.

[22] Hassan, A.K.F., Abdullah, O.A. (2015). New methodology for prestressing fibre composites. *Universal Journal of Mechanical Engineering*, vol. 3, no. 6, p. 252-261, **DOI:10.13189/ujme.2015.030605**.

[23] ASTM D3039-21 (2021). *Standard Test Method for Tensile Properties of Polymer Matrix Composite Materials*. ASTM International, West Conshohocken.

[24] Mayandi, K., Rajini, N., Pitchipoo, P., Jappes, J.T.W., Siva, I. (2015). Mechanical performance of cissusquadrangularis/ polyester composite. *Materials Today Communications*, vol.4, p. 222-232, **DOI:10.1016/j.mtcomm.2015.08.001**.

[25] Shanmugam, D., Thiruchitrambalam, M., Thirumurugan, R. (2014). Continuous unidirectional palmyra palm leaf stalk fibre/glass-polyester composites static and dynamic mechanical properties. *Journal of Reinforced Plastics and Composites*, vol. 33, no. 9, p. 836-850, **DOI:10.1177/0731684413518828**.

[26] Krishnaiah, P., Ratnam, C.T., Manickam, S. (2017). Enhancements in crystallinity, thermal stability, tensile modulus and strength of sisal fibres and their PP composites induced by the synergistic effects of alkali and high intensity ultrasound (HIU) treatments. *Ultrasonics Sonochemistry*, vol. 34, p. 729-742, **DOI:10.1016/j ultsonch.2016.07.008**.

[27] Haque, R., Saxena, M., Shit, S.C., Asokan, P. (2015). Fibre-matrix adhesion and properties evaluation of sisal polymer composite. *Fibers and Polymers*, vol. 16, p. 146-152, **DOI:10.1007/s12221-015-0146-2**.

[28] Webo, W., Masu, L., Maringa, M. (2019). The compression and shear mechanical properties of treated and untreated sisal fibre epoxy resin. *International Journal of Mechanical & Mechatronics Engineering*, vol. 19, no. 6, p. 27-40.

Strojniški vestnik - Journal of Mechanical Engineering 69(2023)7-8, 352-363
DOI:10.5545/sv-jme.2022.510
Original Scientific Paper
Received for review: 2022-12-26
Received revised form: 2023-04-25
Accepted for publication: 2023-05-08

Effect of Vibrator Parameters and Physical Characteristics of Parts on Conveying Velocity

Vishwa Priya Vellingiri[1,*] – Udhayakumar Sadasivam[2]

[1] PSG College of Technology, Department of Robotics and Automation Engineering, India
[2] PSG College of Technology, Department of Mechanical Engineering, India

Automation is generally employed in the area of orienting, lifting, and moving parts for production in industries including automotive, electronic, food, and packaging. With the help of automation, it is possible to reduce the manufacturing time and labour required. The most adaptable tools for feeding small, designed pieces during part assembly are vibratory feeders. Industries have been effectively using vibratory feeders for more than 30 years, indicating that such technology is advanced. Although research in this area has not been lacking, a fundamental understanding of the interactions between a part's physical characteristics and the various vibratory feeder operating parameters in relation to optimal performance, defined as conveying a part with maximum stability and maximum velocity, remains lacking in linear feeders. While several papers discuss the effect of vibratory parameters (excitation frequency and amplitude of vibration) and the coefficient of friction, the effect of characteristics of part (l/w ratio and mass) is neglected. In this work, the effect of these factors on the conveying velocity of prismatic parts made of aluminium and brass on a horizontal track without inclination was determined, and an attempt was made to develop a predictive model based on the above factors. Using Taguchi's design of experiments (DOE), an L16 orthogonal array was designed. A response table for the signal-to-noise ratio has yielded optimal values for each parameter taken into consideration. ANOVA predicted frequency as the most influential parameter, followed by the coefficient of friction. The regression analysis yields an R^2 value of 99.3 % for aluminium and 98.7 % for brass. The results of the regression model and random experiments show a high correlation of 91.66 %. This model is required to set the desired conveying velocity of parts so that continuous flow can be maintained in automated assembly or packaging industries.
Keywords: linear vibratory feeders, conveying velocity, mass, l/w ratio, coefficient of friction

Highlights

- *Vibratory feeders are commonly used for conveying small components in automated assembly lines. Controlling its conveying velocity by controlling its parameters will enable the smooth execution of the assembly process.*
- *This paper is an attempt to study the effect of parameters such as excitation frequency (f), the amplitude of vibration (A), the mass of part (m), length-to-width ratio (l/w) and coefficient of friction (μ) between the part and vibrator, on the conveying velocity (v) of the vibratory feeder.*
- *Though several research studies have examined the behaviour of frequency, amplitude and coefficient of friction, the effect of the physical characteristics, such as the mass of part (m) and length-to-width ratio (l/w,) have not been studied earlier with reference to linear vibrators.*
- *ANOVA results show that the percentage of the contribution of the physical characteristics to the conveying velocity is also significant.*

0 INTRODUCTION

The world was forever altered by the introduction of assembly line technology. Previously, a single operator handled the entire assembly of a product. This required each operator to become proficient in numerous separate specialities, which led to extended apprenticeships and low total output levels. Numerous developers were inspired by Evans **[1]** notion of transporting goods from one location to another without the need for manual labour and adopted it as their own. With even basic automation came improvements in part quality, efficiency through quicker cycle times, yield (less rework and scrap), labour costs, and worker safety. Specialized assembly equipment is typically too expensive for small-scale and medium-scale manufacturing businesses. Flexible automatic assembly methods are employed as an alternative. These systems have the benefit of being reprogrammable, allowing the machine to be set up to execute the sequential processing of the product. Changing the system's programming typically entails reconfiguring the manipulator and the feeding system's parts feeders. Retooling for alternate manufacturing can take up much time and money; therefore, parts feeders, which were frequently retooled during product changes, required considerable knowledge on the part of the manufacturer.

A part feeder is a device that accepts a number of erratically oriented parts at its input and conveys parts in a specific orientation at its output and is divided into non-vibratory and vibratory feeders based on the motive force. Non-vibratory parts feeders are generally exclusive and employed in long production

*Corr. Author's Address: PSG College of Technology, Dept. of Robotics and Automation Engineering, Coimbatore, India, vvp.rae@psgtech.ac.in

run scenarios. A vibratory feeder is an instrument in which vibration is the mode of actuation to feed material to a process or machine. Vibration as a means of conveyance can be achieved by throwing the material to be transferred at a micro-level [2]. Gravity and vibration are both used by vibratory feeders to move material. Vibration is applied to move the material, while gravity is used to set the direction. They are mostly employed for the transportation of numerous small components. Vibratory feeders are of two types.

- vibratory bowl feeder (VBF) and
- linear vibratory feeder.

Literature based on the performance and functioning of vibratory bowl feeders, which deal with studying the jump-less and jump-type conveyance related to amplitude variation [3], calculation of natural frequencies [4], natural resting aspects of parts [5], analysing the feeding and orienting of small parts and flexible part feeding of small components in automation [6], force analysis [7], and simulation of part motion [8].

In a linear feeder, the feeder assembly is a dynamically balanced, two-mass vibrating system whose actuation is by electromagnetic means. This system consists of a trough, which is connected to an electromagnetic drive through leaf springs. Fig. 1 shows a linear vibratory feeder model considered for the study. Like bowl feeders, linear vibratory feeders and their functioning, performance [9] and [10], motion analysis [11] and [12], dynamic modelling [13], analysis on feeding, orienting, conveying small parts without sensor feedback [14] and [15], mathematical modelling of resonant vibratory feeder [16] and [17], and control of the vibrator [18] are also dealt with in literature.

Feeders are the most significant components in an automation system; if the conveying velocity of these feeders could be controlled by directing the factors, then many automated systems could be programmed easily. Several studies focus on the velocity of parts moving on a vibrator and the factors that influence the conveying velocity. A detailed description of the effect of frequency, amplitude and coefficient of friction was given by Boothroyd [19]. Ramalingam and Samuel [20] discussed the behaviour of linear vibratory feeders and the measured values of velocity, which were in good agreement with experimental studies. Frequency, track angle and amplitude of vibration were considered. Sloot and Kruyt [21] have presented theoretical and experimental studies on transporting granular material in both slide and flight conveyors with varying inclinations of the track. The influence of the inclination of the track, throw number, coefficient of friction and vibration angle on the velocity efficiency was studied. The theoretical and experimental results agreed satisfactorily for slide conveyors and varied for flight conveyors. Okabe et al. [22] discussed how friction characteristics behave in a newly developed vibratory feeder.

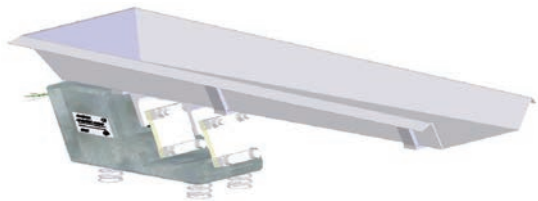

Fig. 1. *Linear vibratory feeder model*

Lim [23] made a dynamic analysis of a vibratory feeder and concluded that the factors that could affect the rigid body's conveying velocity are the vibration angle, the amplitude of vibration, the coefficient of friction, the inclination of the plate and the operating frequency. Wolfsteiner and Pfeiffer [24] used an oscillating track with frequencies up to 100 Hz. In this paper, a complete mechanical model of part feeding dynamics based on unilateral constraints with Coulomb friction was discussed. Kawachi et al. [25] proposed an algorithm for simulating simultaneous collision impulses with friction between rigid bodies.

Based on the literature survey, it was found that significant work has not been carried out in determining the conveying velocity considering the physical characteristics of the part, such as the l/w ratio and mass. This paper fills that gap by considering parts made of brass and aluminium. Brass is mainly used in the field of door hinges, utensils, electrical appliances, pipeline fittings, etc., while aluminium is mainly used in the fields of aerospace, automotive, marine, rail, building construction, energy distribution etc. Models with appropriate l/w ratios and mass have been manufactured for experimental studies. The objective of this research work is to determine the effect of the following factors on the conveying velocity of the part:

- vibrator parameters - excitation frequency (f) and amplitude of vibration (A),
- physical characteristics of mass of part (m), length-to-thickness ratio (l/w) and
- coefficient of friction (μ) between the part and vibrator.

The track angle/inclination is not considered since it is a horizontal vibratory feeder. To reduce the number of experiments and find the most significant

parameter among the vibrator parameters and physical characteristics of parts, a Taguchi design of experiments and ANOVA methods are used [26].

1 SELECTION OF LEVELS OF FACTORS

To satisfy the objective, the following methodology is proposed:

- Fix the levels of mass of the part and length-to-width ratio (l/w) and manufacture them.
- Conduct a pilot study to determine the levels for the factors excitation frequency (f), the amplitude of vibration (A), the mass of part (m), the length-to width-ratio (l/w), and the coefficient of friction (μ) between the part and feeder, for conducting the actual experiments.
- Experimentally determine the effect of the factors on the conveying velocity.
- Determine the most significant factor using ANOVA.
- The method of selection of levels is discussed below. A pilot study to determine the values of the frequency and amplitude of vibration of the feeder was conducted.

1.1 Determining the Excitation Frequency and Amplitude of Vibration

By trial and error, the frequency between 10 Hz to 50 Hz was chosen because, no appreciable movement of parts was observed in the vibratory feeder below 10 Hz and above 50 Hz. The frequency was chosen at equal intervals between 10 Hz to 50 Hz at four levels: 15 Hz, 25 Hz, 35 Hz, and 45 Hz. The Vibrodyne controller has a phase angle control system, which helps vary the voltage and, consequently, the vibration amplitude of an electromagnetic feeder. Vibration amplitude is varied by varying the input voltage (% of the input voltage) of the electromagnetic feeder as per the specifications given in Table 7. Amplitude was chosen between 65 % and 90 % of input voltage, because below 65 % there was no appreciable movement of part in the feeder, and very high decibel noise was observed above 90 % of input voltage. Similar to the frequency, the amplitude was also chosen at equal intervals between 65 % to 90 % of input voltage at four levels (75 %, 80 %, 85 % and 90 % of input voltage), as better velocities were obtained at this range during trials.

The factors and levels chosen for the experimental studies for aluminium and brass are shown in Tables 1 and 2, respectively.

1.2 Determining the l/w ratio and mass of the part

Parts chosen are to be commonly used parts in industries and therefore, prismatic parts made of aluminium and brass were considered for the experimental studies. Four parts with masses of 50 g, 100 g, 150 g and 200 g with a thickness of 6 mm were chosen for experimental studies. The l/w ratio was fixed at four levels (1, 1.5, 2, and 2.5). Hence, 16 workpieces were manufactured in aluminium, as shown in Fig. 2 and brass as in Fig. 3, satisfying the above conditions; the values are given in Tables 3 and 4, respectively.

Table 1. *Factors and levels chosen for aluminium*

Factors	Levels			
	I	II	III	IV
Excitation frequency [Hz]	15	25	35	45
Amplitude of vibration [% of input voltage]	75	80	85	90
Coefficient of friction (μ)	0.290	0.320	0.317	0.572
l/w ratio	1.0	1.5	2.0	2.5
Mass [g]	50	100	150	200

Table 2. *Factors and levels chosen for brass*

Factors	Levels			
	I	II	III	IV
Excitation frequency [Hz]	15	25	35	45
Amplitude of vibration [% of input voltage]	75	80	85	90
Coefficient of friction (μ)	0.331	0.419	0.445	0.629
l/w ratio	1.0	1.5	2.0	2.5
Mass [g]	50	100	150	200

Table 3. *Dimensions of aluminium work piece*

S. No	l/w ratio	Mass [g]	Length [mm]	Width [mm]
1	1	50	56	56
2	1	100	79	79
3	1	150	96	96
4	1	200	111	111
5	1.5	50	68	45
6	1.5	100	96	64
7	1.5	150	119	79
8	1.5	200	136.5	91
9	2	50	80	40
10	2	100	112	56
11	2	150	136	68
12	2	200	158	79
13	2.5	50	87.5	35
14	2.5	100	125	50
15	2.5	150	152.5	61
16	2.5	200	175	70

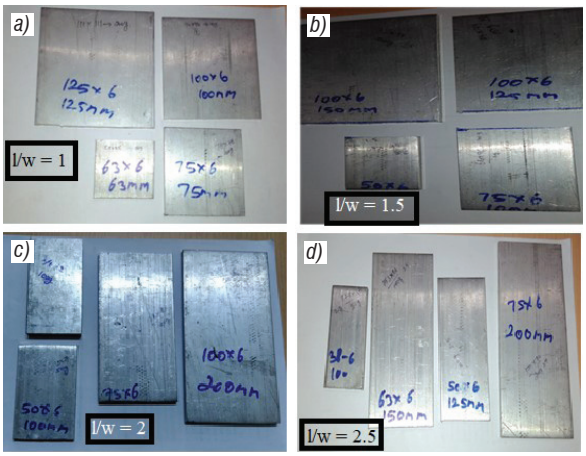

Fig. 2. *Aluminium parts with varying l/w ratio; a) l/w = 1, b) l/w = 1,5, c) l/w = 2, and d) l/w = 2,5*

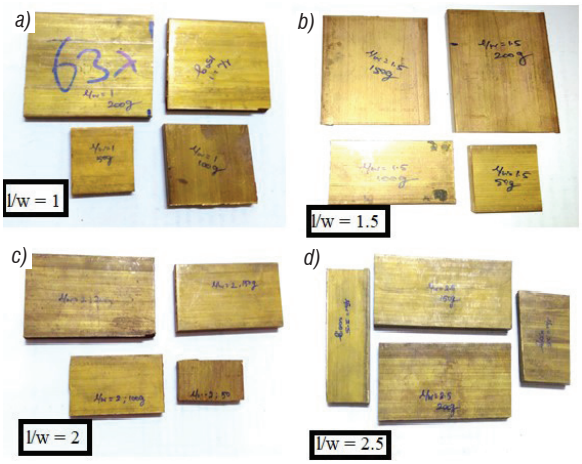

Fig. 3. *Brass parts with varying l/w ratio; a) l/w = 1, b) l/w = 1,5, c) l/w = 2, and d) l/w = 2,5*

Table 4. *Dimensions of brass work piece*

S. No	l/w ratio	Mass [g]	Length [mm]	Width [mm]
1	1	50	30	30
2	1	100	42	42
3	1	150	51	51
4	1	200	59	59
5	1.5	50	36	24
6	1.5	100	51	34
7	1.5	150	63	49
8	1.5	200	72	48
9	2	50	42	21
10	2	100	60	30
11	2	150	72	36
12	2	200	84	42
13	2.5	50	47	19
14	2.5	100	66	26
15	2.5	150	81	32
16	2.5	200	93	37

1.3 Determining the coefficient of friction

To vary the coefficient of friction μ, different track materials are used. The materials other than stainless steel are:

- rubber sheet,
- polythene sheets, and
- black chart.

The stainless-steel tray of the feeder was wrapped with materials (i.e., polythene sheet, black chart and rubber sheet) to vary the coefficient of friction. The coefficient of friction was obtained through the reciprocating friction monitor (RFM) equipment. RFM is an apparatus used to measure the dynamic coefficient of friction of materials under a reciprocating sliding motion.

The base plate of dimension 30 mm × 30 mm × 6 mm is fixed at the bottom and the pin of diameter 4 mm and length of 10 mm is allowed to pass over the base plate. The coefficient of friction values obtained using RFM equipment are listed in Table 5.

Table 5. *Coefficient of friction values*

Part material	Track material			
	Polythene	Stainless steel	Black chart	Rubber sheet
Brass	0.290	0.320	0.317	0.572
Aluminium	0.331	0.419	0.445	0.629

2 EXPERIMENTAL SETUP

The linear vibratory feeder and controller used for experimentation is described below.

2.1 Electromagnetic Part Feeder

The part feeder considered for the experimental studies to determine the effect of vibrator parameters (excitation frequency, amplitude of vibration, track angle), physical characteristics of the part (weight, length to thickness ratio) and coefficient of friction between the part and feeder on conveying velocity of part is LF02 shown in Fig. 4 and the specification is shown in Table 6. The LF02 feeder assembly is a dynamically balanced, two-mass vibrating system whose actuation is by electromagnetic means. This system consists of a trough, which is connected to an electromagnetic drive through leaf springs. Fig. 4 shows the vibratory part feeder with stainless steel track. The electromagnetic drive consisting of a coil and core assembly is located inside the base housing. This assembly is connected to the backside of the

drive unit housing. An armature is also a part of the drive unit and is placed opposite to the core and coil and is connected to the trough mounting bracket. Leaf springs are located at the front of the drive unit housing and are clamped to the drive unit housing and to the trough mounting bracket at the bottom and the top. Fig. 5 shows a block diagram of a linear vibratory feeder, which represents the amplitude and frequency: the vibrator's parameters, varied using the controller without feedback, and the part's physical characteristics considered for the study.

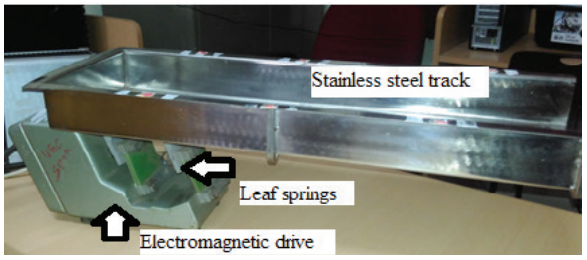

Fig. 4. *Vibratory part feeder with stainless steel track*

Table 6. *Specification of vibratory feeder*

Description	Details
Model	LF 02
Made	HVPL
Frequency range	200 Hz
Track	Stainless steel
Dimension of track (l×w)	600 mm × 180 mm

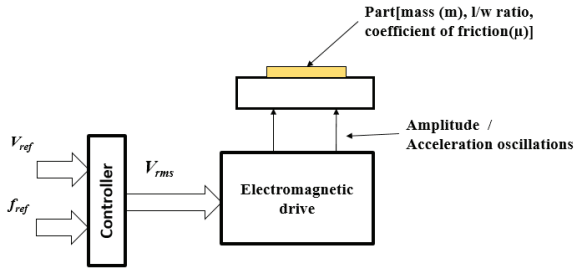

Fig. 5. *Block diagram of an electromagnetic vibratory feeder*

2.2 Feeder Controller

Vibrodyne is a controller for controlling any electromagnetic feeder in the processing and packing industry. Fig. 6 shows the variable frequency variable voltage electromagnetic feeder controller. It has been designed with a 32-bit controller which has:

- a feed rate from 0 % to 100 %,
- non-volatile memory,
- programmable ramp up and ramp down option,
- interacts with PLCs and other automation components in the system.

Table 7 provides the specification of the vibratory feeder controller that was used to control the excitation frequency and amplitude of vibration. The amplitude of vibration is controlled by means of variable voltage.

Table 7. *Specification of feeder controller*

Description	Details
Controller make	Vibrodyne
Frequency range	10 Hz to 200 Hz
Amplitude	10 % to 100 % of output voltage

3 DESIGN OF EXPERIMENTS

The method of design of experiments (DoE) was considered to conduct the experiments on the vibratory part feeder. Taguchi's design **[26]** to **[29]** is used to avoid the extensive experimentation. Five factors and four levels were determined for the experimental studies for which Taguchi suggests an L16 orthogonal array.

4 EXPERIMENTAL STUDIES

The experiment was conducted based on the L16 Taguchi Orthogonal array. The steps followed are described as follows. The vibratory feeder was switched ON. The frequency and amplitude of vibration were set to determined values in the controller. The START button was pressed in the controller, and the parts moved in the part feeder. Experiments were conducted based on the L16 orthogonal array to determine the conveying velocity as the response. The initial and final distances were marked in the vibratory part feeder. As soon as the parts touch the initial line, the timer was switched ON; when the parts touched the final line, the timer was switched OFF. The distance between the initial and the final line is 400 mm. For each part, the trial was conducted five times, based on which the mean time was calculated. Finally, the conveying velocity was obtained by calculating the ratio between the distance travelled by the part and the measured time taken for the part to travel between the initial and final lines. To vary the coefficient of friction, three different sheets (e.g., polythene, black chart, and rubber sheet) are placed on the vibratory part feeder, and the same procedure was repeated. The observations were recorded and presented as follows.

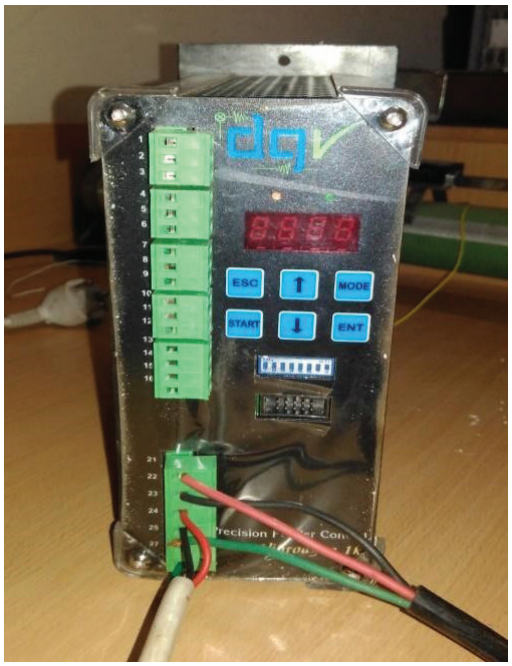

Fig. 6. *Vibrodyne controller*

4.1 Effect of Frequency on Conveying Velocity

Based on the experimental results, a graph is plotted between Frequency and Velocity for both brass and aluminium of mass 50 g, and 200 g and an *l*/*w* ratio of 1 as shown in Figs. 7 and 8.

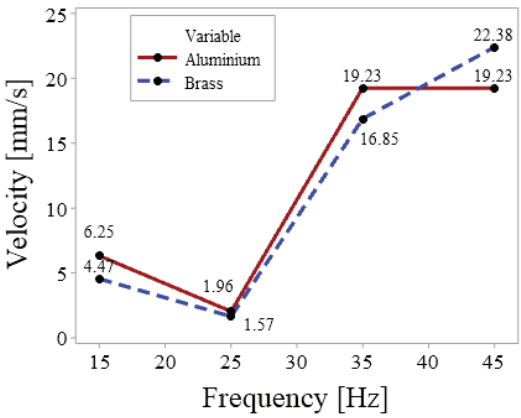

Fig. 7. *Effect of frequency on conveying velocity (m = 50 g, l/w = 1)*

At the frequency of 15 Hz, the velocity is 6 mm/s, as the cycles per second is low, and the parts have enough time to grip onto the track to move forward. It reduces intermittently when it reaches the frequency of 25 Hz. The velocity again increases at 35 Hz and is maximum at the frequency of 45 Hz for both aluminium and brass parts because they tend to jump rapidly to move forward. The effect of the frequency on the conveying velocity is highly non-linear.

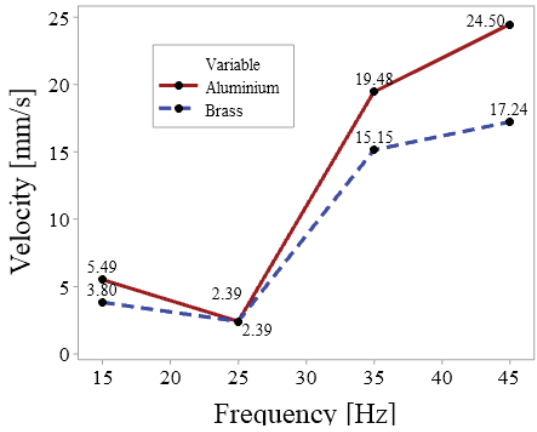

Fig. 8. *Effect of frequency on conveying velocity (m = 200 g, l/w = 1)*

4.2 Effect of Mass on Conveying Velocity

The variation of conveying velocity with respect to mass at constant frequency, amplitude and *l*/*w* ratio is shown in Fig. 9 (f = 15 Hz, A = 75 % of voltage and l/w = 1.5). It shows the behaviour of parts of different masses (50 g, 100 g, 150 g, and 200 g) with an *l*/*w* ratio of 1.5; the frequency is set at 45 Hz, and the amplitude is set at 90 % of the input voltage in the controller. The vibrator is started, and the time taken for each component to travel the distance from the start to finish lines is measured using a timer. The velocity is then calculated by finding the ratio of distance travelled by time taken.

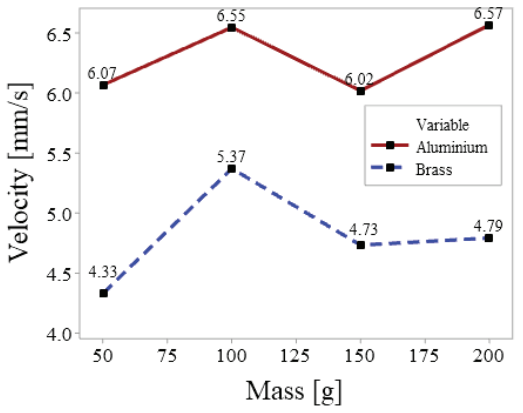

Fig. 9. *Effect of mass on conveying velocity (f = 15 Hz, A = 75 % of voltage and l/w = 1.5)*

From the graph (Fig. 9), it is clear that both aluminium and brass follow the same pattern for velocity. Velocity is low for 50 g mass, while it increases for 100 g again sweeps down at 150 g and increases for 200 g. Velocity is higher when the mass is 100 g and 200 g, compared to when the mass is 50 g and 150 g. Similarly, Fig. 10 shows the effect of mass at a different frequency and amplitude but for the same *l*/*w* ratio (f = 45 Hz, A = 90 % of voltage and *l*/*w* = 1.5). The results are different from the previous graphs due to the change in frequency as well as amplitude. It is clear that the velocity decreases when the mass is increased for a lower frequency and amplitude. Velocity increases in another instance where the frequency and amplitude are higher. Therefore, based on these studies, it can be concluded that the effect is highly non-linear.

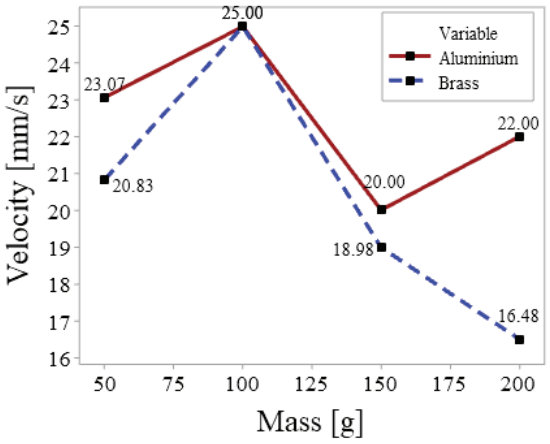

Fig. 10. *Effect of mass on conveying velocity (f = 45 Hz, A = 90 % of voltage and l/w = 1.5)*

4.3 Effect of *l*/*w* ratio on Conveying Velocity

The variation of conveying velocity with respect to *l*/*w* ratio at constant frequency, amplitude, and mass (f = 15 Hz, A = 75 % of voltage and m = 50 g) is, as shown in Fig. 11. In order to study the behaviour, the amplitude and frequency have been varied for the same mass and is as shown in Fig. 12 (f = 25 Hz, A = 80 % of voltage and m = 50 g). From the graphs (Fig. 12), it is clear that aluminium and brass parts follow the same pattern of velocity; velocity is maximum when the length is twice its width. The highest velocity for both aluminium and brass is attained at an *l*/*w* ratio of 2.0 irrespective of the change in amplitude and frequency. The effect of the *l*/*w* ratio on conveying velocity is again non-linear.

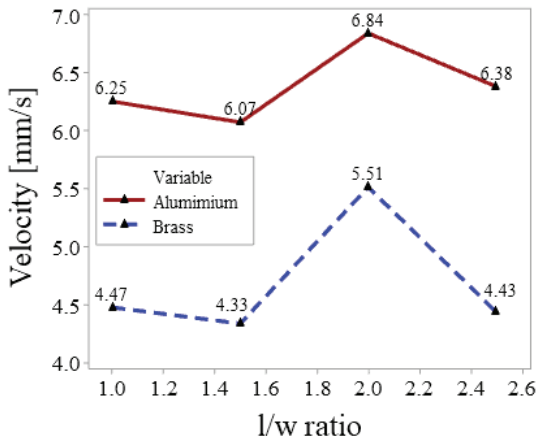

Fig. 11. *Effect of l/w ratio on conveying velocity (f = 15 Hz, A = 75 % of voltage and m = 50 g)*

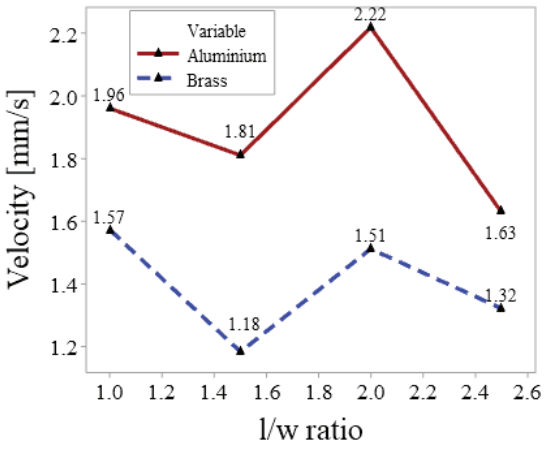

Fig. 12. *Effect of l/w ratio on conveying velocity (f = 25 Hz, A = 80 % of voltage and m = 50 g)*

4.4 Effect of Coefficient of Friction on Conveying Velocity

The frequency, amplitude, mass, and l/w ratio are maintained constant, and the graph is plotted between varying coefficient of friction and conveying velocity for both aluminium and brass; the experimental results are as shown in Fig. 13 (f = 45 Hz, A = 90 % of voltage, m = 50 g and *l*/*w* = 1.5) and Fig. 14 (f = 35 Hz, A = 85 % of voltage, m = 50 g and *l*/*w* = 1).

Irrespective of the change in frequency, amplitude, *l*/*w* ratio and constant mass, the pattern of behaviour of the conveying velocity is the same. Both tracks with lower and higher coefficients provide higher conveying velocity when compared with intermediary values of coefficients of friction. The effect of the coefficient of friction on the conveying velocity is also non-linear.

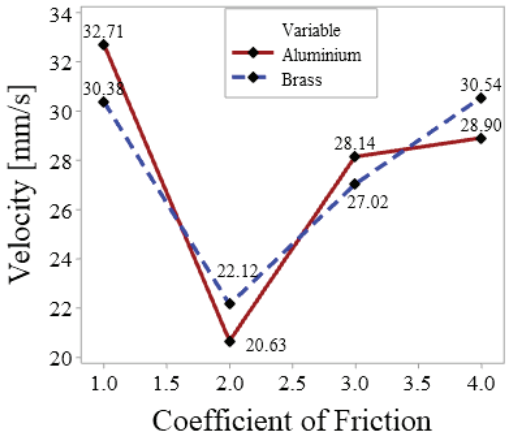

Fig. 13. *Effect of coefficient of friction on conveying velocity (f = 45 Hz, A = 90 % of voltage, m = 50 g and l/w = 1.5)*

From Fig. 14, it is clear that the rubber sheet, which has a higher co-efficient friction, has higher velocity and is closely followed by black chart. Polythene sheet, which has lower co-efficient of friction, provides higher velocity than stainless steel. Developing an analytical model is difficult as the observations are nonlinear. Hence, a predictive model called "regression analysis" was conducted to determine the conveying velocity.

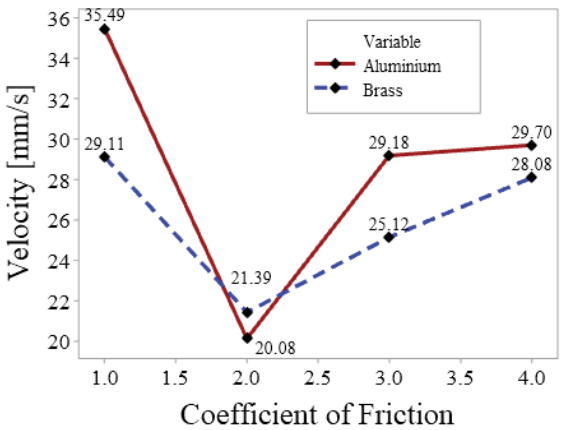

Fig. 14. *Effect of coefficient of friction on conveying velocity (f = 35 Hz, A = 85 % of voltage, m = 50 g and l/w = 1)*

5 REGRESSION ANALYSIS FOR DETERMINING CONVEYING VELOCITY

Regression analysis is a statistical tool that helps to find a quantitative association between independent and dependent variables. Simple linear regression helps fit a straight line for X and Y data points, with the goal of finding the line that best predicts the value of Y from X. Multiple Linear Regression model is tried in this paper to calculate the output (conveying velocity) with the set of input parameters (excitation frequency (f), amplitude of vibration (A), mass of part (m), length-to-thickness ratio (l/w), and coefficient of friction (μ) between the part and feeder). In fact, it creates the equation in which the values are entered to find out the desired output **[27]** to **[30]**. The regression equation was obtained by using Minitab 17 software. The regression equation for aluminium and brass are given in Eqs. (1) and (2), respectively.

For aluminium,

$$\begin{aligned} v = &-172.4 + 13.86\,f + 0.3344\,A + 272.3\,\mu \\ &+ 38.93\,l/w - 0.1329\,m - 0.08167\,f{\times}A \\ &- 3.830\,f{\times}\mu - 1.616\,f{\times}l/w - 0.02339\,f{\times}m \\ &- 1.625\,A{\times}\mu + 0.08481\,A{\times}l/w + 0.007848\,A{\times}m \\ &- 53.94\,\mu{\times}l/w - 0.09394\,\mu{\times}m \\ &+ 0.02844\,l/w{\times}m\,, \end{aligned} \tag{1}$$

$$R^2 = 99.3\ \%\,,$$

For brass,

$$\begin{aligned} v = &\ 135.8 + 1.527\,f - 2.377\,A - 4.031\,\mu \\ &- 17.02\,l/w - 0.2810\,m + 0.000907\,f{\times}A \\ &+ 0.2308\,f{\times}\mu - 0.8903\,f{\times}l/w - 0.004218\,f{\times}m \\ &+ 0.9629\,A{\times}\mu + 0.7603\,A{\times}l/w + 0.005144\,A{\times}m \\ &- 59.15\,\mu{\times}l/w - 0.06450\,\mu{\times}m \\ &- 0.01271\,l/w{\times}m\,, \end{aligned} \tag{2}$$

$$R^2 = 98.7\ \%\,,$$

where, R^2 is the percentage of total variation that could be explained by the regression equation, v conveying velocity [mm/s], f excitation frequency [Hz], A amplitude of vibration [% of input voltage], μ coefficient of friction between the tray and the material, l/w length to width ratio, and m mass [g].

5.1 SN Ratio

In Taguchi designs, a measure of strength is used to identify control factors that reduce inconsistency in a product or process by reducing the effects of uncontrollable factors (noise factors). Process parameters that can be controlled are called the "control factors". Parameters that cannot be controlled during production or product use are called "noise factors", but these can be controlled during experimentation. In a Taguchi-designed experiment, optimal control factor settings are identified that make the process or product strong, or resistant to variation. Higher values of the signal-to-noise ratio (SN) help identify control factor settings that reduce the effects of the noise factors.

Taguchi experiments use an optimization process with two steps. Step 1 identifies those control factors that reduce inconsistency. For this, the signal-to-noise ratio is used. Step 2 identifies control factors that move the mean to the target. This has a small or no effect on the signal-to-noise ratio.

The signal-to-noise ratio quantitates the responses relative to the nominal or target values for various noise conditions. Minitab offers four signal-to-noise ratios. In this analysis, the larger-is-better condition is chosen as the objective is to maximize the output response (i.e., conveying velocity). The mean effects plot for the SN ratio of aluminium is shown in Fig. 15.

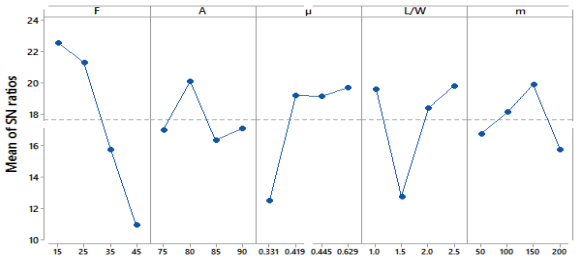

Fig. 15. *SN ratio for aluminium*

Table 8. *Response table for aluminium parts*

Level	f	A	μ	l/w	m
1	22.57	17.04	12.50	19.63	16.80
2	21.32	20.13	19.22	12.79	18.71
3	15.79	16.37	19.19	18.42	19.94
4	10.97	17.12	19.74	19.82	15.75
Delta	11.59	3.76	7.24	7.03	4.19
Rank	1	5	2	3	4

From the response table shown in Table 9 for aluminium, the optimal values of each factor that tend to maximize the conveying velocity could be determined by comparing the values in Tables 8 and 1 for aluminium parts. Maximum conveying velocity (v) for aluminium is obtained at a frequency (f) of 15 Hz, amplitude (A) of 80 % of input voltage, coefficient of friction (μ) of 0.629, l/w ratio of 2.5 and mass (m) of 150 g. The ranking also clearly indicates that the frequency is the most important factor that is influencing the conveying velocity followed by co-efficient of friction, l/w ratio, mass, and amplitude. The mean effects plot for SN ratio of brass is shown in Fig. 16. As per the response Table 9 and factors Table 2, maximum conveying velocity (v) for brass is obtained at a frequency (f) of 15 Hz, amplitude (A) of 90 % of input voltage, coefficient of friction (μ) of 0.290, l/w ratio of 1.0 and mass (m) of 200 g.

Table 9. *Response table for brass parts*

Level	f	A	μ	l/w	m
1	23.85	14.57	19.09	20.84	11.53
2	20.82	17.88	18.71	16.36	17.11
3	12.75	17.44	15.95	15.78	19.07
4	10.73	18.26	14.40	15.17	20.44
Delta	13.12	3.70	4.70	5.68	8.91
Rank	1	5	2	3	4

5.2 Analysis of Variance

Analysis of variance (ANOVA) is a group of statistical models used to explore the differences between group means and the procedures related to them (such as "variation" among and between groups), developed by Fisher [31] and [32] to [35]. ANOVA is used to study the effect of the factors which affect the conveying velocity.

The five input parameters are excitation frequency (f), amplitude of vibration (A), co-efficient of friction (μ), length-to-width ratio (l/w), and mass (m) of the part.

Results of ANOVA shown in Table 10 for aluminium indicate that the excitation frequency is the most influential factor with a contribution of 56.22 %; the second most influential factor is the coefficient of friction with 14.78 % followed by l/w ratio 13.34 % and mass 11.04 %. The least influential is the amplitude with a 4.59 % contribution, which is in line with the literature [14], [36] and [37]. Increasing the amplitude of vibration might increase the conveying velocity. As seen, 80 % of the input voltage for aluminium and 90 % of the input voltage for brass are the optimal values of amplitude. However, the delta value in Fig. 16 is small for amplitude, which indicates that amplitude has a relatively small impact on the conveying velocity. Damping could be one of the reasons for the relatively small impact of amplitude. Table 11 provides the percentage contribution of each factor for brass in a similar manner.

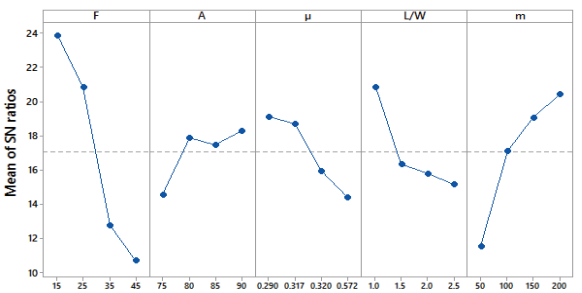

Fig. 16. *SN ratio for brass*

Table 10. *Percentage of individual factors affecting conveying velocity for aluminium*

Source	SS	% of contribution
Frequency	259.32	56.22
Amplitude	21.18	4.59
Coefficient of friction	68.31	14.78
l/w ratio	61.54	13.34
Mass	50.94	11.04
Error	395.23	
Total	461.28	

Table 11. *Percentage of individual factors affecting conveying velocity for brass*

Source	SS	% of contribution
Frequency	344.5	66.02
Amplitude	18.33	3.51
Coefficient of friction	93.47	17.91
l/w ratio	43.79	8.39
Mass	18.33	4.41
Error	426.87	
Total	521.74	

6 VALIDATION

To verify the regression model generated, a random set of experiments (combinations not included in an L16 orthogonal array) have been conducted and the parameter values of which are shown in Table 12. The comparisons of the experimental and regression results are plotted as a bar graph as in Fig. 17. The values of the regression and experimental results have been tabulated in Table 13.

Table 12. *Random experimental values for validation*

Experiment no.	f [Hz]	A [% V]	μ	l/w ratio	m [g]
1	16	76	0.331	1.5	50
2	26	81	0.331	1	100
3	36	86	0.29	2	150
4	46	91	0.29	2.5	200
5	16	74	0.419	1	50
6	26	79	0.419	1.5	200
7	36	84	0.317	2	100
8	46	89	0.317	2.5	50
9	17	87	0.629	1	200
10	27	82	0.629	2	50
11	37	87	0.572	1.5	100
12	47	92	0.572	2.5	150
13	17	73	0.445	1	150
14	27	78	0.445	1.5	150
15	37	83	0.32	2	50
16	47	88	0.32	2.5	200

From Fig. 17 and Table 13, it can be understood that the regression model results follow the same pattern as that of experimental results. The average deviation between the results of the model and experimental values was found to be 8.34 %. Hence, it could be concluded that the regression model predicted has a high correlation with the experimental results. These types of models could be used in industries to control the conveying velocity by varying the factors based on the physical characteristics of the part to be conveyed.

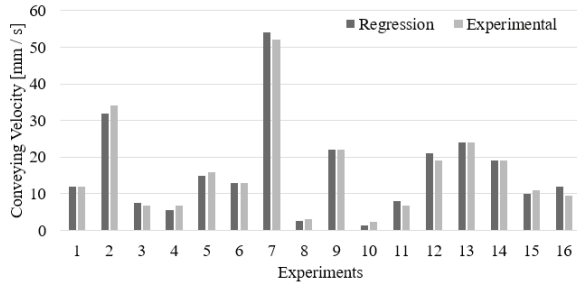

Fig 17. *Comparison of experimental and regression values*

Table 13. *Validated regression and experimental values of conveying velocity*

Experiment no.	Regression values	Experimental values
1	12	12
2	32	34
3	7.5	6.9
4	5.5	6.7
5	15	16
6	13	13
7	54	52
8	2.6	3
9	22	22
10	1.3	2.3
11	7.9	6.8
12	21	19
13	24	24
14	19	19
15	10	11
16	12	9.5

7 CONCLUSION

In this paper, an effort was made to find and understand the effect of factors such as excitation frequency (f), amplitude of vibration (A), coefficient of friction (μ), l/w ratio and mass (m) of the part on conveying velocity through experimental studies for Aluminium and brass parts.

The factors and levels were identified using the trial-and-error method. Taguchi's DOE was used to design experiments based on the five factors, each at four levels, to obtain an L16 array.

Based on the experimental results, the effects of the factors were studied and found to be highly non-linear.

Due to the complexity of developing an analytical model, a regression model was developed using Minitab software and the obtained expression for both aluminium and brass are discussed in Eqs. (1) and (2). R^2 of 99.3 % and 98.7 % for aluminium and brass, respectively, shows that the differences between the observations and the predicted values are very small. The larger R^2 value means that the regression model best fits the observations.

By using Taguchi's Design Analysis, SN ratio also has been plotted and the optimum values of each factor to maximize the conveying velocity has been determined.

ANOVA results show that frequency was the most influential parameter that affects the conveying velocity followed by the coefficient of friction and l/w ratio.

The regression model results were compared with random experimental results and the average deviation was found to be 8.34 %, which shows a high correlation between the two.

Based on the predicted model, industries can set the desired conveying velocity to maintain continuous flow of components for automated or robotic assembly.

8 FUTURE WORK

The same work can be extended to asymmetrical parts with different aspect ratios and the relationship between vibrator parameters and physical characteristics of the part can be determined.

9 NOMENCLATURES

f	excitation frequency, [Hz]
A	amplitude of vibration, % of input voltage, [% V]
μ	coefficient of friction
l/w	length-to-width ratio
m	mass, [g]
v	conveying velocity, [mm/s]

10 REFERENCES

[1] Evans, O. (1805) *The Abortion of the Young Steam Engineer's Guide*, Fry and Kammerer.

[2] Goncharevich, I.F., Frolov, K.V., Rivin, E.I. (1990). *Theory of Vibratory Technology*. Hemisphere Publishing Corporation.

[3] Yasuyuki, S., Yasuo O. (1963). Studies on vibratory feeder. *Bulletin of JSME*, vol. 6, no. 21, p. 37-43, **DOI:10.1299/jsme1958.6.37**.

[4] Okabe, S., Yokayama, Y. (1981). Study of vibratory feeders: Calculation of natural frequency of bowl-type vibratory feeders. *Transactions of the ASME*, vol. 103, no. 1, p. 249-256, **DOI:10.1115/1.3254873**.

[5] Ngoi, B.K.A., Lim, L.E.N., Ee, J.T. (1997). Analysis of natural resting aspects of parts in a vibratory bowl feeder - Validation of "drop test", *The International Journal of Advanced Manufacturing Technology*, vol. 13, p. 300-310, **DOI:10.1007/BF01179612**.

[6] Tay, M.L., Chua, P.S.K., Sim, S.K., Gao, Y. (2005). Development of a flexible and programmable parts feeding system, *International Journal of Production Economics*, vol. 98, no. 2, p. 227-237, **DOI:10.1016/j.ijpe.2004.05.019**.

[7] Silversides, R., Dai, J.S., Seneviratne, L. (2005). Force analysis of a vibratory bowl feeder for automatic assembly. *Journal of Mechanical Design*, vol. 127, no. 4, p. 637-645, **DOI:10.1115/1.1897407**.

[8] Ashrafizadeh, H., Ziaei-Rad, S. (2013). A numerical 2D simulation of part motion in vibratory bowl feeders by discrete element method. *Journal of Sound and Vibration*, vol. 332, no. 13, p. 3303-3314, **DOI:10.1016/j.jsv.2013.01.020**.

[9] Leckie, G.G., Barr, A.D.S. (1970). A study of the performance of a non-linear resonant vibratory conveyor. *Proceedings of the Institution of Mechanical Engineers*, vol. 185, no. 1, p. 1115-1126, **DOI:10.1243/PIME_PROC_1970_185_121**.

[10] Winkler, G. (1978). Analysing the vibrating conveyor. *International Journal of Mechanical Sciences*, vol. 20, no. 9, p. 561-570, **DOI:10.1016/0020-7403(78)90014-0**.

[11] Parameswaran, M.A., Ganapathy, S. (1979). Vibratory conveying-analysis and design: A review. *Mechanism and Machine Theory*, vol. 14, no. 2, p. 89-97, **DOI:10.1016/0094-114X(79)90024-7**.

[12] Buzzoni, M., Battarra, M., Mucchi, E., Dalpiaz, G. (2017). Motion analysis of a linear vibratory feeder, Dynamic modeling and experimental verification. *Mechanism and Machine Theory*, vol. 114, p. 98-110, **DOI:10.1016/j.mechmachtheory.2017.04.00**.

[13] Redford, A.H., Dhailami, F. (1997). A new approach to small parts vibratory conveying. *Flexible Automation and Intelligent manufacturing: Proceedings of the Seventh international FAIM Conference*.

[14] Udhayakumar, S., MohanRam, P.V., Ranganathan, G. (2010). Manufacturing automation for handling assymetric components. *Acta Technica Corviniensis Bulletin of Engineering*, vol. 3, p. 57-66.

[15] Suresh, M., Mathew, N.K., Rohith, S.P., Aishwarya, R., Ramanathan, K., (2021). Assembly automation - an efficient appraoch to find optimal parameters for part feeders, *International Journal of Robotics and Automation*, vol. 36, no. 4, p. 246-255, **DOI:10.2316/J.2021.206-0564**.

[16] Despotović, Ž.V., Urukalo, D., Lečić, M.R., Ćosić, A. (2017). Mathematical modeling of resonant linear vibratory conveyor with electromagnetic excitation: simulations and experimental

results. *Applied Mathematical Modelling*, vol. 41, p. 1-24, **DOI:10.1016/j.apm.2016.09.010**.

[17] Goldberg, K.Y. (1993). Orienting polygonal parts without sensors. *Algorithmica*, vol. 10, p. 201-225, **DOI:10.1007/BF01891840**.

[18] Ribic, A.I., Despotovic, Ž.V. (2010). High-performance feedback control of electromagnetic vibratory feeder. *IEEE Transactions on Industrial Electronics*, vol. 57, no. 9, p. 3087-3094, **DOI:10.1109/TIE.2009.2037677**.

[19] Boothroyd, G. (1992). *Assembly Automation and Product Design*. Marcel Dekker Inc., New York, p. 31-94.

[20] Ramalingam, M., Samuel, G.L. (2009). Investigation on the conveying velocity of a linear vibratory feeder while handling bulk-sized small parts. *The International Journal of Advanced Manufacturing Technology*, vol. 44, p. 372-382, **DOI:10.1007/s00170-008-1838-1**.

[21] Sloot, E.M, Kruyt, N.P. (1996). Theoretical and experimental study of the transport of granular materials by inclined vibratory conveyors. *Powder Tehnology*, vol. 87, no. 3, p. 203-210, **DOI:10.1016/0032-5910(96)03091-4**.

[22] Okabe, S., Yokoyama, Y., Boothroyd, G. (1988). Analysis of vibratory feeding where the track has directional friction characteristics. *The International Journal of Advanced Manufacturing Technology*, vol. 3, no. 4, p. 73-85, **DOI:10.1007/BF02601835**.

[23] Lim, G.H. (1997). On the conveying velocity of a vibratory feeder. *Computers & Structures*, vol. 62, no. 1, p. 197-203, **DOI:10.1016/S0045-7949(96)00223-4**.

[24] Wolfsteiner, P., Pfeiffer, F. (1999). The parts transportation in a vibratory feeder, *IUTAM Symposium on Unilateral Multibody Contacts*, vol. 72, p. 309-318, **DOI:10.1007/978-94-011-4275-5_30**.

[25] Kawachi, K., Suzuki, H. Kimura, F. (1997). Simulation of rigid body motion with impulsive friction force. *Proceedings of IEEE International Symposium on Assembly and Task Planning*, vol. 6, no. 6, p. 182-187, **DOI:10.1109/ISATP.1997.615405**.

[26] Cicek, A., Kivak, T., Samtas, G. (2012). Application of Taguchi method for surface roughness and roundness error in drilling of AISI 316 Stainless Steel. *Strojniski vestnik - Journal of Mechanical Engineering*, vol. 58, no. 3, p.165-174, **DOI:10.5545/sv-jme.2011.167.**

[27] Michigan Engineering (2016). from *https://controls.engin.umich.edu/wiki/index.php/* accessed on 2016-09-07.

[28] Dung, H., Nguyen, N., Quy, T., Thien, N. (2019). Cutting forces and surface roughness in face-milling of SKD61 hard steel. *Strojniški vestnik - Journal of Mechanical Engineering*, vol. 65, no. 6, p. 375-385, **DOI:10.5545/sv-jme.2019.6057**.

[29] Çolak, O. (2012). Investigation on machining performance of Inconel 718 in high pressure cooling conditions. *Strojniški vestnik - Journal of Mechanical Engineering*, vol. 58, no. 11, p. 683-690, **DOI:10.5545/sv-jme.2012.730**.

[30] Baek, S.H., Hong, S.H., Cho, S.S., Jang, D.Y., Joo, W.S. (2019). Erratum to "Optimization of process parameters for recycling of mill scale using Taguchi experimental design", *Journal of Mechanical Science and Technology*, vol. 33, art. ID 4573, **DOI:10.1007/s12206-019-0854-4**.

[31] Fisher, R.A. (1936). The use of multiple measurements in taxonomic problems. *Annals of Eugenics*, vol. 7, p. 179-188, **DOI:10.1111/j.1469-1809.1936.tb02137.x**.

[32] Eniko, P., Soković, M., Kramar, D. (2016). Influence of non-productive operations on product quality. *Strojniški vestnik - Journal of Mechanical Engineering*, vol. 62, no. 3, p. 197-204, **DOI:10.5545/sv-jme.2015.3109**.

[33] Omprakasam, S., Marimuthu, K., Raghu, R., Velmurugan, T. (2022). Statistical modelling and optimization of TIG welding process parameters using Taguchi's method. *Strojniški vestnik - Journal of Mechanical Engineering*, vol. 68, no. 3, p. 200-209, **DOI:10.5545/sv-jme.2021.7414**.

[34] Saravana, K., Thanigaivelan, R. (2021). Optimization of laser parameters and dimple geometry using PCA-coupled GRG. *Strojniški vestnik - Journal of Mechanical Engineering*, vol. 67, no 10, p. 525-533, **DOI:10.5545/sv-jme.2021.7246**.

[35] Anmol, B., Reeta, W. (2021). Process parameter optimization for maximising tensile strength in friction stir-welded carbon steel. *Strojniški vestnik - Journal of Mechanical Engineering*, vol. 67, no. 6, p. 311-321, **DOI:10.5545/sv-jme.2021.7203**.

[36] Udhayakumar, S., Mohanram, P.V., Yeshwanth, S., Manas Ranjan Biswal, Sabareeswaran, A. (2014). Development of an adaptive part feeder for handling sector-shaped parts. *Assembly Automation*, vol. 34, no. 3, p. 227-236, **DOI:10.1108/AA-04-2013-043**.

[37] Mathew, N.K., Mayilswamy, S., Sharma, S., Mehta, N.A., Kumar, J. (2021). Investigation of track based on part measurement. *MAPAN*, vol. 36, p. 875-889, **DOI:10.1007/s12647-021-00480-y**.

Vsebina

Strojniški vestnik - Journal of Mechanical Engineering
letnik 69, (2023), številka 7 8
Ljubljana, julij-avgust 2023
ISSN 0039-2480

Izhaja dvomesečno

Razširjeni povzetki (extended abstracts)

Strojniški vestnik - Journal of Mechanical Engineering 69(2023)7-8, SI 31

Prejeto v recenzijo: 023-03-30
Prejeto popravljeno: 2023-05-03
Odobreno za objavo: 2023-05-31

Dinamska karakterizacija stožčastih ležajev – validacija od spodaj-navzgor

MatejR azp nik[1], Thm as Bisch[2], Miha Boltežar[1]
[1] Univerza v Ljubljani, Fakulteta za strojništvo, Slovenija
[2] ZF Friedrichshafen AG, Nemčija

Članek obravnava tematiko prenosa vibracij preko kotalnih ležajev. Analizirana sta krogličnи in stožčasti tip ležaja. Najprej je podan način modeliranja ležajev, kjer analitično izračunano togostno matriko ležaja vstavimo v širši sistem, popisan z metodo končnih elementov (MKE). Zatem je predstavljena namensko zasnovana testirna naprava za validacijo numeričnega modela. Sledi popis poteka dela na način od spodaj navzgor, prikaz rezultatov ter diskusija in zaključki.

Rezultati v obliki frekvenčno prenosnih funkcij (FPF) so predstavljeni na nivoju celotne naprave, pri čemer je sistem impulzno vzbujen z modalnim kladivom na določenem mestu na gredi, odziv pa pomerjen s pomočjo pospeškomera na ohišju. Sprva so v sistem vstavljeni togi obroči namesto ležajev. Prikazano je dobro ujemanje FPF med eksperimentom in numeriko. Različne aksialne obremenitve vnesene v sistem pokažejo, da sprememba obremenitve zanemarljivo vpliva na spremembo lastnih frekvenc sistema. S tem je potrjena predpostavka, da se togost zasnovanega sistema ne spreminja z aplicirano aksialno obremenitvijo. Sistem lahko torej znotraj znanih robnih pogojev in obremenitev obravnavamo kot linearen. Nadaljnje testiranje je izvedeno z vstavljenimi ležaji, vsaka morebitna sprememba dinamike sistema pa je posledično pripisana nelinearni spremembi togosti ležajev.

Nato so podani rezultati za sistem z ne-rotirajočo se gredjo in z vstavljenimi krogličnimi ležaji. Prikazano je dobro ujemanje med numerično izračunanimi FPF in pomerjenimi. V izbranem frekvenčnem območju vidimo štiri različne vrhove, ki se z večanjem aksialne obremenitve pomikajo proti višjim frekvencam. Prikazane so tudi pripadajoče modalne oblike. V nadaljevanju je sistemu dodan motor povezan preko sklopke na gred. Rezultati pokažejo, da vnos rotacije ne povzroči spremembe lokacij lastnih frekvenc v obravnavanem območju do 6000 RPM. V tem območju vrtenja so torej rotodinamični vplivi (giroskpski efekt in centrifugalne sile) v obravnavanem sistemu zanemarljivi.

Enak postopek testiranja je nato prikazan za sistem z vstavljenimi stožčastimi ležaji. Sprva je izvedena analiza na sistemu z ne-rotirajočo se gredjo. Opaženo je, da pride do velikega odstopanja med numerično izračunanimi in eksperimentalno dobljenimi FPF. Ob dodatni primerjavi lastnih oblik je razvidno, da je dejanska togost stožčastega ležaja znatno večja od izračunane.

Za namen ugotovitve izvora omenjenega odstopanja je izdelan celoten model krogličnega in stožčastega ležaja s pomočjo MKE ter izvedena kvazi-statična analiza. Pridobljene so krivulje pomika v odvisnosti od obremenitve ter iz njih pridobljene togosti. Dobljene karakteristike so primerjane z rezultati pridobljenimi na analitični način in sicer po metodi avtojev Lim in Singh ter po industrijskem standardu ISO/TS 16281. Prikazano je dobro ujemanje za kroglični tip ležaja. Pri stožčastem tipu ležaja pa je opaziti dobro ujemanje med obema analitičnimi modeloma, vendar faktorsko odstopanje napram rezultatom iz numeričnega modela.

V diskusiji sta navedena dva možna razloga, ki bi lahko vplivala na opaženo neskladnost za stožčasti tip ležaja in sicer: 1) Analitični model ležaja upošteva zgolj povprečni naklonski kot stožčastih ležajev, v realnosti pa ima stožčasti ležaj dva različna kota in sicer med kotalnim elementom in notranjim obročem ter kotalnim elementom in zunanjim obročem. Posledično analitični model zanemari aksialno silo, ki kotalni element rine iz kontakta. Prav tako je zanemarjen dodaten kontakt med kotalnim elementom in robom za nased lociranem na notranjem obroču, ki onemogoča da bi kotalni element aksialno zdrsel višje po tečini notranjega obroča; 2) Pojav trenja je izključen iz obeh uporabljenih analitičnih modelov kakor tudi pri numeričnem modeliranju z MKE. V realnosti pa je sistem obratoval v mejnem območju mazanja, kjer ima trenje lahko znaten vpliv.

V zaključku je podano, da analitični model togosti ležaja ustrezno popisuje realno dinamsko stanje za kroglični tip ležaja, medtem ko model togosti za stožčasti tip ni ustrezen. Obravnavana študija predstavlja izhodišče za morebitno prihodnjo izpeljavo nadgrajenega analitičnega modela togosti ležaja za stožčasti tip.

Ključne besede: Dinamski model ležaja, stožčasti ležaj, kroglični ležaj, togostna matrika ležajev, prenos vibracij, študija od spodaj-navzgor

*Naslov avtorja za dopisovanje: Univerza v Ljubljani, Fakulteta za strojništvo, Aškerčeva 6, 1000 Ljubljana, Slovenija, miha.boltezar@fs.uni-lj.si

Strojniški vestnik - Journal of Mechanical Engineering 69(2023)7-8, SI 32

Prejeto v recenzijo: 2023-01-29
Prejeto popravljeno: 2023-05-15
Odobreno za objavo: 2023-06-06

Izboljšanje zmogljivosti dvoetažnih škarjastih dvigal s parametrično analizo

Anh-Tuan Dang – Dang-Viet Nguyen – Dinh-Ngoc Nguyen*
Tehniška univerza Thai Nguyen, Thai Nguyen, Vietnam

Škarjasta dvigala so specialne naprave, namenjene dvigovanju ljudi, opreme ali materiala. Z zložljivim mehanizmom, ki spominja na škarje, omogočajo varen dostop do težje dosegljivih mest brez lestev ali delovnih odrov in so tako primerna za različne panoge, kot so gradbeništvo, servisne storitve in proizvodnja. Odvisno od specifičnih delovnih zahtev in vrste tovora je pomembna izbira primerne konfiguracije dvigala. Zaradi različnih dejavnikov pri obratovanju dvigala pa lahko predstavljata izziv izbor velikosti in postavitve valjev na okvirju ter določitev delovnih parametrov valjev za izpolnitev zahtev. Postopki računanja in preizkušanja v programski opremi za simulacije, vključno z gradnjo modelov, določitvijo parametrov materiala in upoštevanjem dimenzij, zahtevajo veliko naporov in časa. Ti dejavniki vplivajo na konstrukcijski proces, zlasti ob upoštevanju dinamičnih sprememb obremenitev sistema med obratovanjem. Zato obstaja potreba po metodi, ki bi poenostavila proces preračuna sistemov škarjastih dvigal v pomoč pri konstruiranju in proizvodnji.

S parametrično določitvijo orientacije, dimenzij in lastnosti valjev ter z uporabo matematičnih transformacij je mogoče preprosto določiti vse značilnosti sistema, vključno z dvižno višino, nosilnostjo in celo porazdelitvijo obremenitev po posameznih elementih. Rezultati vključno z dvižno višino platforme, potisno silo valjev in reakcijami v zgibih so bili validirani na podlagi primerjave z 2D-modelom, konstruiranim in simuliranim v programski opremi Working Model. Proces je potrdil tudi točnost enačb, izpeljanih v študiji.

Točnost predlagane metode je bila ovrednotena s pomočjo simulacij na podlagi modelov v programski opremi Working Model. Potrjena je bila uporabnost metode pri konstruiranju in proizvodnji, saj skrajšuje računski čas in izboljšuje učinkovitost konstrukcijskega procesa. Konstruktorji lahko dimenzionirajo valje v specifičnih postavitvah ali pa izberejo orientacije valjev, ki izpolnjujejo zahteve glede obratovanja škarjastega dvigala.

Pričujoča študija se razlikuje od ostalih raziskav, ki analizirajo konstrukcije s fiksnimi dimenzijami ter prinaša več prednosti in inovativnih prispevkov, med drugim:

- Tehnika parametričnega dimenzioniranja omogoča analizo geometrije in obremenitev dvoetažnih škarjastih dvigal kot funkcij.
- Z opredelitvijo dimenzijskih parametrov postavitve valjev je mogoče točno izračunati značilnosti sistema kot so višina platforme, stabilnost platforme in reakcije v zgibih. S tem se poenostavi izbor komponent ter niso potrebni kompleksni pregledi ali eksperimenti s 3D-modeli.
- Na podlagi določenih reakcij in značilnosti sistema je mogoče dodatno optimizirati detajle konstrukcije sistema (izbor primernih ležajev za vrtilne zgibe, določitev najbolj obremenjenih delov okvirja za izboljšanje konstrukcije) in tako znižati proizvodne stroške.

Ključne besede: dvoetažno škarjasto dvigalo, orientacija valjev, kinematična analiza, parametrično konstruiranje

*Naslov avtorja za dopisovanje: Tehniška univerza Thai Nguyen, Thai Nguyen, Vietnam, ngocnd@tnut.edu.vn

Strojniški vestnik - Journal of Mechanical Engineering 69(2023)7-8, SI 33

Prejeto v recenzijo: 2023-03-17
Prejeto popravljeno: 2023-04-27
Odobreno za objavo: 2023-05-15

Do okolja prijazen pristop k obdelavi težje odrezovalnega dupleksnega nerjavnega jekla AISI 4462 z vrtinčno cevjo

Fikret Sönmez*
Univerza Manisa Celal Bayar, Tehniška univerza Hasan Ferdi Turgutlu, Turčija

Obdelava z odrezavanjem je kompleksen proces, na katerega vplivajo mnogi dejavniki. Obrabi orodja se ni mogoče izogniti, odvisna pa je od raznih pogojev pri obdelavi. Pomemben rezultat obdelave z odrezavanjem je poleg obrabljanja orodja tudi površinska hrapavost. Cilj študije je analiza obrabljanja orodja in površinske hrapavosti pri obdelavi dupleksnega nerjavnega jekla AISI 4462 z metodo vrtinčnega hlajenja v kombinaciji z mokrim odrezavanjem.

Za analizo obrabe orodja in površinske hrapavosti v pogojih mokrega odrezavanja in hlajenja z vrtinčno cevjo so bile opravljene meritve po vsakem prehodu orodja. Spremembe obrabe in hrapavosti so bile spremljane do izteka življenjske dobe orodja.

Obdelovanci so bile palice iz dupleksnega nerjavnega jekla AISI 4462 s premerom 75 mm in dolžino 110 mm. Eksperimenti so bili opravljeni s ploščicami TNMG 160404-M3 in z orodnim držalom PTGNR2020K16 ob uporabi priporočenih rezalnih parametrov po standardu ISO 3685: globina reza 1 mm, podajanje 0,1 mm/obrat in polmer rezalnega roba 0,4 mm. Izbrana je bila rezalna hitrost 120 m/min. Eksperimenti z mokrim struženjem so bili opravljeni s 5-odstotno koncentracijo hladilno-mazalne tekočine. Uporabljena je bila tudi do okolja prijazna vrtinčna cev (tipa Ranque-Hilsch), s katero je bil na izhodu iz šobe vrtinčne cevi pri tlaku 5 bar dosežen zračni tok s temperaturo –23 °C. Pri eksperimentih s struženjem je bila za vsak prehod uporabljena rezalna dolžina 90 mm. Po vsakem prehodu sta bili izmerjeni površinska hrapavost obdelovancev in obraba orodja, in sicer obraba na prosti ploskvi in zarezna obraba. Ko se je serija eksperimentov zaključila, je bila opravljena tudi preiskava rezalnih orodij po metodah SEM in SEM-EDX.

Glede na meritve obrabe na prosti ploskvi in zarezne obrabe je obstojnost orodja pri mokrem struženju 19,8 minute (14 prehodov). Pri eksperimentih z vrtinčno cevjo se je obstojnost orodja iztekla po 11,1 minute (v 7. prehodu). Tako obraba na prosti ploskvi kot zarezna obraba sta se v pogojih mokre obdelave in vrtinčnega hlajenja pojavili hitro, po 1,4 minute odrezavanja (v prvem prehodu). V pogojih mokre obdelave sta se obe vrsti obrabe povečevali s konstantno stopnjo. Pri vrtinčnem hlajenju se je orodje obrabilo hitro, po 6,6 minutah odrezavanja. Opažen je bil pojav abrazivne obrabe in nastanka nalepka. Zanimivo je, da je bilo nalepka manj pri eksperimentih z vrtinčno cevjo, kar je verjetno znak za težave z odvajanjem odrezkov. Boljši nadzor nad odrezki je bil v vseh eksperimentih dosežen v pogojih vrtinčnega hlajenja. Geometrija lomilca odrezkov na ploščici morda ni pravilno delovala zaradi nizke vrednosti podajanja (0,1 mm/obrat). Boljša površinska hrapavost je bila sicer pričakovana v pogojih mokre obdelave, toda vrednosti površinske hrapavosti *Ra* in *Rz* sta bili nižji pri eksperimentih z vrtinčno cevjo. Vrtinčno hlajenje v splošnem zagotavlja dvojno kakovost površine, najnižja površinska hrapavost pa je znašala približno 0,65 µm za *Ra* in 3 µm za *Rz*. Ugotovitev je mogoče pojasniti z oblikovanjem manj nalepka med eksperimenti z vrtinčno cevjo.

Pri manjših vrednostih podajanja se izgubi nadzor nad odvajanjem odrezkov in zato bo v prihodnjih eksperimentih mogoče preučiti še vplive mokrega in vrtinčnega hlajenja z večjimi vrednostmi podajanja. Možne smernice za prihodnje delo: zanimiva bi bila podrobnejša študija uporabe vrtinčne cevi v različnih pogojih odrezavanja, kakor tudi uporaba minimalnega mazanja (MQL) z nanodelci v vrtinčni cevi.

V pričujoči študiji je bil prvič podrobneje preučen vpliv do okolja prijaznega sistema hlajenja z vrtinčno cevjo v kombinaciji z dovodom hladilno-mazalne tekočine pri struženju dupleksnega nerjavnega jekla AISI 4462. Sledi ugotovitev, da je lahko uporaba vrtinčne cevi primerna rešitev za obdelavo dupleksnih nerjavnih jekel z odrezavanjem.

Ključne besede: vrtinčna cev, obdelava z odrezavanjem, dupleksno nerjavno jeklo, obstojnost orodja, površinska hrapavost

*Naslov avtorja za dopisovanje: Univerza Manisa Celal Bayar, Tehniška univerza Hasan Ferdi Turgutlu, Manisa 45140, Turčija, sonmezfikret@gmail.com

Strojniški vestnik - Journal of Mechanical Engineering 69(2023)7-8, SI 34

Prejeto v recenzijo: 2023-03-17
Prejeto popravljeno: 2023-05-16
Odobreno za objavo: 2023-05-30

Tehnike odločanja o tveganju zalog z uporabo analize vedenja strank

Ivan Marc – Tomaž Berlec*
Univerza v Ljubljani, Fakulteta za strojništvo, Slovenija

Učinkovito upravljanje zalog je pomembna funkcija vsakega globalnega podjetja. Obstoječa literatura in opažanja industrije trdijo, da nosilci odločanja pogosto odstopajo od optimalnega vedenja pri naročanju, ki ga predpisujejo kvantitativni modeli. Takšna odstopanja pa pogosto spremljajo visoki stroški zalog in/ali nerealizirana prodaja. Zato obstaja potreba po implementaciji kakovostnega modela upravljanja zalog v podjetja. Predstavljen model stroškovne analize toka vrednosti CASM (cost analyzis stream mapp) je uporaben in koristen v primeru optimizacije proizvodnega procesa na primeru zalog.

Opravljena raziskava je potrdila dejstvo, da je izdelava matematičnega modela, ki za izhodišče uporablja informacije o nakupnem vedenju kupcev, lahko dobra osnova za določitev povprečnega stroška izdelka ACP (average cost of product). V raziskavi smo se omejili le na vpliv prevelikih količin zalog na velikost povprečnega stroška. Z uporabo modela smo dokazali, da velike količine medfaznih zalog negativno vplivajo na lastno ceno končnega izdelka, saj prekomerna proizvodnja lahko povzroči dvig lastne cene izdelka do mere, da podjetje ni več konkurenčno ter lahko celo posluje z izgubo.

Model je bil testiran na podatkih podjetja, ki proizvaja pohištveno okovje in ima kupce po celem svetu. Kljub uspešnosti podjetja, smo ugotovili, da bi podjetje lahko s pravilnim upravljanjem zalog in z uvedbo vitke proizvodnje s pomočjo modela CASM, še bolj utrdilo svojo pozicijo na trgu. Pri raziskavi smo se omejili na proizvodni proces izdelka Spone Basic. Popisali smo potek proizvodnih operacij in izdelali tok vrednosti materiala in informacij VSM (value stream mapping). V analizi toka vrednost obstoječega stanja je bilo ugotovljeno, da gre v konkretnem primeru za presežno proizvodnjo, saj je bila dnevna potreba 50.000 kosov izdelka, med operacijami na dan opazovanja pa smo zabeležili 466.666 kosov. Na osnovi nakupnega vedenja kupca smo izdelali matematični model in izbrali funkcijo gostote verjetnosti povpraševanja $f_X(x) = a^2 x \cdot e^{-ax}$, ki se, dobro prilega dejanskemu obnašanju nakupnega vedenja potrošnika po izdelku v praksi.

Na osnovi matematičnega modela smo izračunali vpliv sprememb gibanja količin zalog (z) med delovnimi operacijami $E[C]$ v proizvodnem procesu na povprečni strošek skladiščenja zalog $E[C]$ in na povprečni strošek izdelka ACP ter na tveganje β, ki se pojavi pri zniževanju medfaznih zalog s ciljem, da bi se približali željeni vitkosti proizvodnega procesa.

Izračunali smo optimalno količino zaloge in optimalni povprečni strošek izdelka ACP, ter rezultate primerjali z realnimi rezultati podjetja, kar je potrdilo, da strošek skladiščenja zaloge med delovnimi operacijami pomembno vpliva na povprečni strošek izdelka ACP in posledično na lastno ceno izdelka. Izvedli smo simulacijo treh možnih scenarijev vitkosti proizvodnega procesa, kjer smo ugotovili, da je optimalna količina zaloge 30,000 kosov, pri kateri so stroški zalog minimalni pri zmernem tveganju, ki znaša 17 %.

Predlagani model CASM, se je izkazal kot primerno in enostavno orodje, ki omogoča linijskemu managerju učinkovito podporo pri odločanju glede količin v odvisnosti od obnašanja kupcev. To pomeni, da bodo odločitve managementa določale stopnjo vitkosti in učinkovitost proizvodnega procesa in posledično vplivale na končni izid povprečnega stroška izdelka na koncu proizvodnega procesa. S simulacijo si lahko pomaga tudi vodja prodaje tako, da med pogajanji s kupci sproti analizira, kaj željene količine pomenijo za stroške proizvodnje in v odvisnosti od tega lahko ustrezno vodi pogajanja pri določitvi prodajne cene.

Keywords: vitka proizvodnja, povpraševanje kupca, simulacija tveganja, optimizacija zalog

*Naslov avtorja za dopisovanje: Univerza v Ljubljani, Fakulteta za strojništvo, Aškerčeva 6, 1000 Ljubljana, Slovenija, tomaz.berlec@fs.uni-lj.si

Strojniški vestnik - Journal of Mechanical Engineering 69(2023)7-8, SI 35

Prejeto v recenzijo: 2023-01-31
Prejeto popravljeno: 2023-03-28
Odobreno za objavo: 2023-05-15

Analiza globine in kota zareze po metodi končnih elementov pri izsekovanju nerjavne jeklene pločevine s predzarezovanjem

Kaan Emre Engin*
Tehniška fakulteta pri univerzi Adiyaman, Oddelek za strojništvo, Turčija

Luknjanje je pomemben postopek v industriji predelave pločevine. Gre za postopek rezanja pločevine z orodjem, ki ga sestavljata oblikovan pestič in spodnja matrica. Med najpomembnejšimi zahtevami pri postopku luknjanja sta tudi zmanjšanje potrebe po dodelavah na minimum in ohranitev kakovosti površin. Težavo pri izpolnjevanju te zahteve predstavljajo srh in izstopajoče površine. Nepravilnosti se s površin običajno odstranijo z brušenjem in z drugimi postopki čiščenja, kar pa je povezano s podaljšanjem dela, višjimi stroški in dodatno obremenitvijo delavcev.

Za izboljšanje kakovosti površin odrezanih pločevinastih komponent je bila nedavno razvita metoda izsekovanja s predzarezovanjem. Pri tem naprednem postopku se v obdelovanec najprej vtisne zareza z določenimi lastnostmi, temu pa sledi klasično luknjanje. Prisotnost zareze na obdelovancu zahteva analizo dodatnih parametrov, kot so globina zareze, izražena z odstotno vrednostjo višine zareze glede na debelino obdelovanca, in kot vtisnjene zareze na površini obdelovanca. Le malo raziskovalcev se je ukvarjalo z izsekovanjem pločevine s predzarezovanjem in s pripadajočimi parametri. Vrednost kota zareze je običajno fiksna in znaša 60°. Nobena od raziskav, ki so bile vključene v pregled, pa ni analizirala vpliva teh lastnosti na nerjavna jekla, ki so eden od najbolj razširjenih materialov v industriji. Novost študije je v raziskavi izsekovanja z vnaprejšnjo izdelavo zareze do treh različnih globin (15 %, 30 % in 60 % debeline obdelovanca) in s šestimi različnimi koti zareze (10°, 20°, 30°, 40°, 50° in 60°) v nerjavnem jeklu 1.4301, in sicer eksperimentalni ter z analizo po metodi končnih elementov. Z analizo vpliva različnih kotov in globin zarez v nerjavnem jeklu tako zapira obstoječo vrzel v literaturi. Za eksperimentalni del raziskave je bilo izdelano orodje po meri, za analizo po metodi končnih elementov pa je bila uporabljena programska oprema Deform-2D. Najprej so bile z nateznim preizkusom nerjavnega jekla 1.4301 določene krivulje odvisnosti napetosti od deformacij, ki jih zahteva programska oprema.

Nato so bili opravljeni eksperimenti z luknjanjem in izsekovanjem s predzarezovanjem. Premer spodnje matrice je bil 10 mm, premer pestiča za navadno luknjanje pa je znašal 9,80 mm z rezilno zračnostjo 5 %. Zaradi progresivne narave postopka izsekovanja je bil izdelan poseben votli pestič s kotom zareze 60° in globino zareze v vrednosti 60 % debeline obdelovanca. Eksperimenti so bili opravljeni na hidravlični stiskalnici s silo 300 kN in hitrostjo pestiča 1 mm/s. Po potrditvi ujemanja eksperimentalnih in numeričnih rezultatov so bile analizirane preostale vrednosti globine in kota zareze z analizo po metodi končnih elementov. Analizirane so bile dolžine strižnih con in potrebne rezalne sile.

Rezultati kažejo na zmanjšanje potrebnih rezalnih sil pri preizkušancih z globljimi zarezami in širšimi koti zarez. Sile pri preizkušancih z zarezo so bile manjše kot pri preizkušancih, luknjanih po klasičnem postopku, kar je v neposredni povezavi z zmanjšanjem debeline materiala zaradi oblikovanja zareze na obdelovancu. Ugotovljeno je bilo tudi, da obstajata vrednosti globine in kota zareze, pri katerih je dosežena optimalna kakovost odrezane površine: pri kotu zareze 50° za globino zareze 15 %, pri kotu zareze 40° za globino 30 % in pri kotu zareze 20° za globino zareze v višini 60 %. Pojav srha se je občutno zmanjšal. Ocenjeno dolžino strižne cone na preizkušancu po luknjanju (22,6 %) je bilo mogoče preseči samo pri kotu zareze 50° in globini 15 % (24,4 %). Preostale vrednosti strižnih con niso bile primerne za rezanje pločevine iz materiala 1.4301 v primerjavi s konvencionalnim luknjanjem.

Izkazalo se je torej, da lahko daje izsekovanje s predzarezovanjem boljše rezultate kot luknjanje, zlasti z vidika preprečitve nastanka srha, če je glavna zahteva po kakovosti površin in odsotnosti dodelave na obdelovancih. Največjo dolžino strižne cone brez srha je mogoče doseči z nujnimi pripravljalnimi deli, kot je analiza po metodi končnih elementov, saj je strižna cona pri nekorigiranih vrednostih prekratka.

Ključne besede: luknjanje, izsekovanje s predzarezovanjem, rezalne sile, kot zareze, globina zareze, oblikovanje srha, strižna cona, kakovost površine

*Naslov avtorja za dopisovanje: Tehniška fakulteta pri univerzi Adiyaman, Oddelek za strojništvo, Altinsehir Mah. 3005. Sok. No:13, Adiyaman, Turčija, kengin@adiyaman.edu.tr

Strojniški vestnik - Journal of Mechanical Engineering 69(2023)7-8, SI 36

Prejeto v recenzijo: 2022-11-19
Prejeto popravljeno: 2023-05-13
Odobreno za objavo: 2023-05-31

Eksperimentalna raziskava mehanskih lastnosti biokompozitov, ojačenih z vlakni sisala in ločja

Benchaabane Chaouki[1,2,*] – Kirad Abdelkader[1,2] – Aissani Mouloud[3]

[1] Univerza v Blidi 1, Znanstvena fakulteta, Laboratorij FUNDAPL, Alžirija
[2] Univerza v Blidi 1, Tehniška fakulteta, Oddelek za strojništvo, Alžirija
[3] Raziskovalno središče za industrijske tehnologije CRTI, Alžirija

Kompoziti na osnovi sintetičnih steklenih ali ogljikovih vlaken so sicer razširjeni v industriji, vendar so tudi dragi in škodljivi za okolje. Cilj je poiskati druge vrste vlaken, ki so cenejša, ne škodujejo okolju ter niso izdelana s predelavo surove nafte oz. ki izvirajo iz obnovljivih virov. Pričujoče delo obravnava biokompozite, ojačene z rastlinskimi vlakni sisala in ločja, ki so razširjena po vsem svetu. Opravljena je bila študija za določitev najboljših mehanskih lastnosti biokompozitov z vlakni omenjenih rastlin, pridobljenih po najnovejših postopkih oz. tehnikah. Preučen je bil tudi vpliv postopkov pridobivanja vlaken in novih tehnik povezovanja vlaken na mehanske lastnosti kompozitov.

Naravna vlakna so bila pridobljena na tri različne načine: z dolgotrajnim namakanjem v vodi, s kemijsko obdelavo v alkalni raztopini natrijevega hidroksida (7 % NaOH) in z zakopavanjem listov rastline v vlažno zemljo. Za povezovanje vlaken so bile uporabljene tri tehnike. Prva je klasična (vlakna so monolinearna), drugi dve pa sta bili razviti šele v zadnjem času. Gre za povezovanje vlaken v vrvi s sukanjem in s pletenjem. Za matrico je bila uporabljena nenasičena poliestrska smola. Kompozitni materiali so bili izdelani po postopku ročnega lameliranja.

Izkazalo se je, da na mehanske lastnosti biokompozitov signifikantno vplivajo kemijska obdelava, kakovost vlaken ter stik med vlakni in osnovo. Obdelava v raztopini NaOH je izboljšala topografijo bočne površine vlaken z odstranitvijo voskov, pektina, hemiceluloze in dela lignina. V nateznih preizkusih so se kompoziti poliestra s sisalom odrezali bolje od kompozitov z vlakni ločja. Razlika presega 200 % ne glede na način pridobivanja vlaken. Najvišje vrednosti modula elastičnosti so bile izmerjene pri tehniki sukanja vrvi. Modul elastičnosti kompozita, ojačenega s sisalovimi vlakni, je dvakrat večji od modula elastičnosti kompozita, ojačenega z vlakni ločja.

Premer vlaken sisala in ločja je bil izmerjen pod optičnim mikroskopom. Vlakna so nabreknila v smoli za 18 % do 20 %. Iz teh meritev je mogoče sklepati o vplivu načina pridobivanja na povprečno vrednost premera vlakna. Najboljša vlakna so čistejša, torej brez ostankov nečistoč, in manjšega premera. Strukturna analiza biokompozitov z vrstično elektronsko mikroskopijo je razkrila, da je oprijem vlaken z osnovo (dober stik med vlakni in osnovo) najboljši pri vlaknih, obdelanih z raztopino NaOH. Ta vlakna so tanka.

Nedavno razvita tehnika povezovanja kemijsko obdelanih vlaken v vrvi je prispevala k najboljši ojačitvi biokompozitov. V nasprotju z nekaterimi objavami so prav omenjene tehnike povezovanja kemijsko obdelanih vlaken omogočile zmanjšanje debeline biokompozitov in znižanje stroškov priprave.

Razviti biokompoziti so uporabni za različne aplikacije, zlasti tam, kjer niso izpostavljeni večjim mehanskim obremenitvam in kjer obstaja potreba po lahkih in nestrupenih konstrukcijah, npr. za armaturne plošče v vozilih, hrbtni del voznikovega sedeža, notranji del streh v avtobusih in plovilih ipd.

Ključne besede: naravna vlakna, sisal, ločje, mehanske lastnosti, biokompozit, poliester, natezni preizkus

*Naslov avtorja za dopisovanje: Univerza v Blidi 1, Znanstvena fakulteta, Laboratorij FUNDAPL, Alžirija. chaoukiben27@yahoo.com

Strojniški vestnik - Journal of Mechanical Engineering 69(2023)7-8, SI 37

Prejeto v recenzijo: 2022-12-26
Prejeto popravljeno: 2023-04-25
Odobreno za objavo: 2023-05-08

Vpliv parametrov vibracijskega dodajalnika in fizikalnih lastnosti delov na transportno hitrost

Vishwa Priya Vellingiri[1,*] – Udhayakumar Sadasivam[2]

[1]Tehniški kolidž PSG, Oddelek za robotiko in avtomatizacijo, Indija
[2]Tehniški kolidž PSG, Oddelek za strojništvo, Indija

Avtomatizacija se uporablja za usmerjanje, dvigovanje in premikanje delov v panogah proizvodne industrije, kot so avtomobilska, elektronska, živilska in industrija embalaže. S pomočjo avtomatizacije se skrajša čas izdelave in znižajo stroški dela. Najbolj prilagodljivo orodje za dovajanje manjših sestavnih delov pri montaži so vibracijski dodajalniki. Le-ti uspešno obratujejo v industriji že več kot 30 let, kar priča o njihovi napredni tehnologiji.

Raziskav na tem področju sicer ni malo, manjka pa osnovno razumevanje odvisnosti med fizikalnimi lastnostmi delov in različnimi obratovalnimi parametri linearnih vibracijskih dodajalnikov za optimalno zmogljivost, ki je opredeljena z največjo stabilnostjo in hitrostjo transporta. Več člankov obravnava vpliv parametrov vibracijskega mehanizma (vzbujalna frekvenca in amplituda vibracij) ter količnika trenja, medtem ko je bil vpliv lastnosti delov (razmerje $d/š$ in masa) zanemarjen.

V pričujočem članku je obravnavan vpliv parametrov kot so vzbujalna frekvenca (f), amplituda vibracij (A), masa dela (m), razmerje med dolžino in širino ($d/š$) ter količnik trenja (μ) med delom in vibratorjem na transportno hitrost (v) vibracijskega dodajalnika. Analiziran je vpliv teh dejavnikov na hitrost transporta prizmatičnih aluminijastih in medeninastih delov po horizontalni progi brez naklona. Predstavljen je tudi poskus oblikovanja prediktivnega modela na podlagi zgornjih dejavnikov. Oblikovano je bilo ortogonalno polje L16 po Taguchijevi metodi zasnove eksperimentov. Preglednica odgovorov za razmerje med signalom in šumom daje optimalne vrednosti za vse obravnavane parametre. Analiza ANOVA je pokazala, da ima največji vpliv frekvenca, sledi pa ji količnik trenja. Signifikanten je tudi odstotni prispevek fizikalnih lastnosti dela k hitrosti transporta. Z regresijsko analizo je bila izračunana vrednost R^2 v višini 99,3 % za aluminij in 98,7 % za medenino.

Rezultati regresijskega modela in naključnih eksperimentov so pokazali visoko stopnjo korelacije 91,66 %. Model je pomemben zato, ker lahko pripomore k doseganju želene hitrosti transporta za neprekinjen tok delov pri avtomatizirani montaži oz. pakiranju.

Študijo bi bilo mogoče razširiti tudi na asimetrične dele z različnimi razmerji med dolžino in širino ter določiti odvisnosti med parametri vibracijskega dodajalnika in fizikalnimi lastnostmi delov.

Ključne besede: linearni vibracijski dodajalniki, transportna hitrost, masa, razmerje d/š, količnik trenja, zasnova eksperimentov po Taguchiju, ANOVA

*Naslov avtorja za dopisovanje: Tehniški kolidž PSG, Oddelek za robotiko in avtomatizacijo, Coimbatore, Indija, vvp.rae@psgtech.ac.in

Guide for Authors

All manuscripts must be in English. Pages should be numbered sequentially. The manuscript should be composed in accordance with the Article Template given above. The suggested length of contributions is 10 to 20 pages. Longer contributions will only be accepted if authors provide justification in a cover letter. For full instructions see the Information for Authors section on the journal's website: http://en.sv-jme.eu .

SUBMISSION:

Submission to SV-JME is made with the implicit understanding that neither the manuscript nor the essence of its content has been published previously either in whole or in part and that it is not being considered for publication elsewhere. All the listed authors should have agreed on the content and the corresponding (submitting) author is responsible for having ensured that this agreement has been reached. The acceptance of an article is based entirely on its scientific merit, as judged by peer review. Scientific articles comprising simulations only will not be accepted for publication; simulations must be accompanied by experimental results carried out to confirm or deny the accuracy of the simulation. Every manuscript submitted to the SV-JME undergoes a peer-review process.

The authors are kindly invited to submit the paper through our web site: http://ojs.sv-jme.eu. The Author is able to track the submission through the editorial process - as well as participate in the copyediting and proofreading of submissions accepted for publication - by logging in, and using the username and password provided.

SUBMISSION CONTENT:

The typical submission material consists of:

- A **manuscript** (A PDF file, with title, all authors with affiliations, abstract, keywords, highlights, inserted figures and tables and references),
- Supplementary files:
  - a **manuscript** in a WORD file format
  - a **cover letter** (please see instructions for composing the cover letter)
  - a ZIP file containing **figures** in high resolution in one of the graphical formats (please see instructions for preparing the figure files)
  - possible **appendicies** (optional), cover materials, video materials, etc.

Incomplete or improperly prepared submissions will be rejected with explanatory comments provided. In this case we will kindly ask the authors to carefully read the Information for Authors and to resubmit their manuscripts taking into consideration our comments.

COVER LETTER INSTRUCTIONS:

Please add a **cover letter** stating the following information about the submitted paper:

1. Paper **title**, list of **authors** and their **affiliations**. **One** corresponding author should be provided.
2. **Type of paper**: original scientific paper (1.01), review scientific paper (1.02) or short scientific paper (1.03).
3. A **declaration** that neither the manuscript nor the essence of its content has been published in whole or in part previously and that it is not being considered for publication elsewhere.
4. State the **value of the paper** or its practical, theoretical and scientific implications. What is new in the paper with respect to the state-of-the-art in the published papers? Do not repeat the content of your abstract for this purpose.
5. We kindly ask you to suggest at least two **reviewers** for your paper and give us their names, their full affiliation and contact information, and their scientific research interest. The suggested reviewers should have at least two relevant references (with an impact factor) to the scientific field concerned; they should not be from the same country as the authors and should have no close connection with the authors.

FORMAT OF THE MANUSCRIPT:

The manuscript should be composed in accordance with the Article Template. The manuscript should be written in the following format:

- A **Title** that adequately describes the content of the manuscript.
- A list of **Authors** and their **affiliations**.
- An **Abstract** that should not exceed 250 words. The Abstract should state the principal objectives and the scope of the investigation, as well as the methodology employed. It should summarize the results and state the principal conclusions.
- 4 to 6 significant **key words** should follow the abstract to aid indexing.
- 4 to 6 **highlights;** a short collection of bullet points that convey the core findings and provide readers with a quick textual overview of the article. These four to six bullet points should describe the essence of the research (e.g. results or conclusions) and highlight what is distinctive about it.
- An **Introduction** that should provide a review of recent literature and sufficient background information to allow the results of the article to be understood and evaluated.
- A **Methods** section detailing the theoretical or experimental methods used.
- An **Experimental section** that should provide details of the experimental set-up and the methods used to obtain the results.
- A **Results** section that should clearly and concisely present the data, using figures and tables where appropriate.
- A **Discussion** section that should describe the relationships and generalizations shown by the results and discuss the significance of the results, making comparisons with previously published work. (It may be appropriate to combine the Results and Discussion sections into a single section to improve clarity.)
- A **Conclusions** section that should present one or more conclusions drawn from the results and subsequent discussion and should not duplicate the Abstract.
- **Acknowledgement** (optional) of collaboration or preparation assistance may be included. Please note the source of funding for the research.
- **Nomenclature** (optional). Papers with many symbols should have a nomenclature that defines all symbols with units, inserted above the references. If one is used, it must contain all the symbols used in the manuscript and the definitions should not be repeated in the text. In all cases, identify the symbols used if they are not widely recognized in the profession. Define acronyms in the text, not in the nomenclature.
- **References** must be cited consecutively in the text using square brackets [1] and collected together in a reference list at the end of the manuscript.
- **Appendix(-icies)** if any.

SPECIAL NOTES

Units: The SI system of units for nomenclature, symbols and abbreviations should be followed closely. Symbols for physical quantities in the text should be written in italics (e.g. *v*, *T*, *n*, etc.). Symbols for units that consist of letters should be in plain text (e.g. ms^{-1}, K, min, mm, etc.). Please also see: http://physics.nist.gov/cuu/pdf/sp811.pdf .

Abbreviations should be spelt out in full on first appearance followed by the abbreviation in parentheses, e.g. variable time geometry (VTG). The meaning of symbols and units belonging to symbols should be explained in each case or cited in a **nomenclature** section at the end of the manuscript before the References.

Figures (figures, graphs, illustrations digital images, photographs) must be cited in consecutive numerical order in the text and referred to in both the text and the captions as Fig. 1, Fig. 2, etc. Figures should be prepared without borders and on white grounding and should be sent separately in their original formats. If a figure is composed of several parts, please mark each part with a), b), c), etc. and provide an explanation for each part in Figure caption. The caption should be self-explanatory. Letters and numbers should be readable (Arial or Times New Roman, min 6 pt with equal sizes and fonts in all figures). Graphics (submitted as supplementary files) may be exported in resolution good enough for printing (min. 300 dpi) in any common format, e.g. TIFF, BMP or JPG, PDF and should be named Fig1.jpg, Fig2.tif, etc. However, graphs and line drawings should be prepared as vector images, e.g. CDR, AI. Multi-curve graphs should have individual curves marked with a symbol or otherwise provide distinguishing differences using, for example, different thicknesses or dashing.

Tables should carry separate titles and must be numbered in consecutive numerical order in the text and referred to in both the text and the captions as Table 1, Table 2, etc. In addition to the physical quantities, such as *t* (in italics), the units [s] (normal text) should be added in square brackets. Tables should not duplicate data found elsewhere in the manuscript. Tables should be prepared using a table editor and not inserted as a graphic.

REFERENCES:

A reference list must be included using the following information as a guide. Only cited text references are to be included. Each reference is to be referred to in the text by a number enclosed in a square bracket (i.e. [3] or [2] to [4] for more references; do not combine more than 3 references, explain each). No reference to the author is necessary.

References must be numbered and ordered according to where they are first mentioned in the paper, not alphabetically. All references must be complete and accurate. Please add DOI code when available. Examples follow.

Journal Papers:

Surname 1, Initials, Surname 2, Initials (year). Title. *Journal*, volume, number, pages, DOI code.

[1] Hackenschmidt, R., Alber-Laukant, B., Rieg, F. (2010). Simulating nonlinear materials under centrifugal forces by using intelligent cross-linked simulations. *Strojniški vestnik - Journal of Mechanical Engineering,* vol. 57, no. 7-8, p. 531-538, DOI:10.5545/sv-jme.2011.013.

Journal titles should not be abbreviated. Note that journal title is set in italics.

Books:

Surname 1, Initials, Surname 2, Initials (year). Title. Publisher, place of publication.

[2] Groover, M.P. (2007). *Fundamentals of Modern Manufacturing*. John Wiley & Sons, Hoboken.

Note that the title of the book is italicized.

Chapters in Books:

Surname 1, Initials, Surname 2, Initials (year). Chapter title. Editor(s) of book, book title. Publisher, place of publication, pages.

[3] Carbone, G., Ceccarelli, M. (2005). Legged robotic systems. Kordić, V., Lazinica, A., Merdan, M. (Eds.), Cutting Edge Robotics. Pro literatur Verlag, Mammendorf, p. 553-576.

Proceedings Papers:

Surname 1, Initials, Surname 2, Initials (year). Paper title. Proceedings title, pages.

[4] Štefanić, N., Martinčević-Mikić, S., Tošanović, N. (2009). Applied lean system in process industry. *MOTSP Conference Proceedings*, p. 422-427.

Standards:

Standard-Code (year). Title. Organisation. Place.

[5] ISO/DIS 16000-6.2:2002. *Indoor Air – Part 6: Determination of Volatile Organic Compounds in Indoor and Chamber Air by Active Sampling on TENAX TA Sorbent, Thermal Desorption and Gas Chromatography using MSD/FID.* International Organization for Standardization. Geneva.

WWW pages:

Surname, Initials or Company name. Title, from http://address, date of access.

[6] Rockwell Automation. Arena, from *http://www.arenasimulation.com,* accessed on 2009-09-07.

EXTENDED ABSTRACT:

When the paper is accepted for publishing, the authors will be requested to send an **extended abstract** (approx. one A4 page or 3500 to 4000 characters or approx. 600 words). The instruction for composing the extended abstract are published on-line: http://www.sv-jme.eu/information-for-authors/ .

COPYRIGHT:

Authors submitting a manuscript do so on the understanding that the work has not been published before, is not being considered for publication elsewhere and has been read and approved by all authors. The submission of the manuscript by the authors means that the authors automatically agree to publish the paper uder CC-BY 4.0 Int. or CC-BY-NC 4.0 Int. when the manuscript is accepted for publication. All accepted manuscripts must be accompanied by a Copyright Agreement, which should be sent to the editor. The work should be original work by the authors and not be published elsewhere in any language without the written consent of the publisher. The proof will be sent to the author showing the final layout of the article. Proof correction must be minimal and executed quickly. Thus it is essential that manuscripts are accurate when submitted. Authors can track the status of their accepted articles on https://en.sv-jme.eu/.

PUBLICATION FEE:

Authors will be asked to pay a publication fee for each article prior to the article appearing in the journal. However, this fee only needs to be paid after the article has been accepted for publishing. The fee is 380 EUR (for articles with maximum of 6 pages), 470 EUR (for articles with maximum of 10 pages), plus 50 EUR for each additional page. The additional cost for a color page is 90.00 EUR (only for a journal hard copy; optional upon author's request). These fees do not include tax.

Strojniški vestnik -Journal of Mechanical Engineering
Aškerčeva 6, 1000 Ljubljana, Slovenia, e-mail: info@sv-jme.eu

9 770039 248001
ISSN 0039-2480

http://www.sv-jme.eu

Contents

Papers